Dynamics and Control of a Tilting Three Wheeled Vehicle

Berote, Johan

Award date:
2010

Awarding institution:
University of Bath

DYNAMICS AND CONTROL OF A TILTING THREE WHEELED VEHICLE

Submitted by Johan J. H. Berote
for the degree of
Doctor of Philosophy
of the University of Bath
2010

Summary

Narrow commuter vehicles have attracted considerable interest in recent years as a means of reducing congestion and emissions in the urban environment. In order for these vehicles to provide similar levels of safety as bigger passenger vehicles, they must be relatively tall and fully enclosed. Due to the tall and narrow nature of the vehicle, they are prone to rolling over during cornering. To prevent this from happening, it is necessary to tilt the vehicle into the turn in order to compensate for the moment due to the lateral force generated by the tyres. The success of this type of vehicle depends primarily on the control strategy used to tilt the vehicle. Although a number of theoretical models have been developed outlining possible tilt control strategies, experimental data is scarce.

CLEVER is a direct tilt controlled three-wheel prototype vehicle that was developed at the University of Bath as part of an EU funded project. The current control strategy utilises measurements of speed and steer to predict the lateral acceleration and hence the tilting angle required to balance the vehicle during cornering. The cabin of the vehicle is then tilted to the desired angle using two hydraulic actuators. Although the vehicle performs well in steady state, transient dynamics have been shown to lead to instability and ultimately roll-over of the vehicle.

The aim of the work presented here is to create an understanding of the dynamics that lead to the transient state instability and design a control method which will improve the handling characteristics of the vehicle and prevent dangerous transients. In order to study the vehicle's dynamics and test the new control system, a full multi-body model is developed using the SimMechanics software package. The model is validated using data from numerous experimental tests performed with the prototype vehicle. Using the full vehicle model, it is possible to analyse the scenarios that could lead to the transient-state roll-over of the vehicle, creating a good understanding of the dynamics that lead to these potentially dangerous situations. Taking these dynamics into account, a lateral

dynamics optimisation study is performed which proves the necessity for independent control of the tilting mechanism and the lateral acceleration, confirming the need for combined steer and direct tilt control. The new control system is then developed using a linearised model in order to optimise the controller in the frequency domain and is tested using the non-linear multi-body model. A simple combined control approach is presented and shown to significantly reduce transient roll moments, resulting in a much safer and more predictable handling characteristic.

Although a number of control strategies have been proven successful in simulation by other researchers, these relied on complex switching strategies and weighting functions to switch between steer tilt control and direct tilt control and often required numerous sensor inputs. The system proposed by the author combines both steer and tilt control concurrently, using the driver steering input and vehicle speed as the only input parameters. The simplified principle of the control strategy is anticipated to faciliate implementation in a prototype vehicle.

Acknowledgements

I would like to show my gratitude to my supervisors Dr Jos Darling and Professor Andrew Plummer, without whom this thesis would not have been possible. Thank you for the guidance and support which you have shown throughout the project. The CLEVER project captured my imagination when I first read about it as an undergraduate student and I am very grateful for having had the opportunity to make my own contribution.

I also offer my regards to all of those who supported me in any respect during the completion of this thesis.

Contents

Nomenclature

Listed below are the main parameters and variables used throughout this thesis. Additional subscripted versions of these variables may also be found in the document to describe more specific parts of the system, which are not listed here. Where this occurs, the meaning of these parameters will be clearly stated in the appropriate section.

A_p	actuator piston area	[m^2]
a	londitudinal distance of front axle to front cabin CoG	[m]
a_y	lateral acceleration	[ms^{-2}]
$a_{y,max}$	maximum lateral acceleration	[ms^{-2}]
B	'Magic Formula' stiffness factor	[-]
b	longitudinal distance of rear axle to front cabin CoG	[m]
b_θ	actuator lever arm	[m]
C	'Magic Formula' shape factor	[-]
C_α	slip stiffness coefficient	[-]
C_γ	camber coefficient	[-]
D	'Magic Formula' peak value	[-]
E	'Magic Formula' curvature factor	[-]
F_y	lateral force on tyre	[m]
F_z	vertical force on tyre	[m]
g	gravitational acceleration	[ms^{-2}]
h	distance of vehicle CoG from ground	[m]
h_c	distance of cabin CoG from ground	[m]
h_r	distance of rear module CoG from ground	[m]
h_θ	distance of tilt bearing from ground	[m]
I_c	cabin roll inertia about CoG	[kgm^2]
I_r	rear module roll inertia about CoG	[kgm^2]
I_x	vehicle roll inertia about CoG	[kgm^2]

I_y	vehicle pitch inertia about CoG	[kgm^2]
I_z	vehicle yaw inertia about CoG	[kgm^2]
K	valve flow coefficient	[-]
K_θ	tyre camber coefficient	[-]
$K_{\theta r}$	rear steer coefficient	[-]
K_c	pressure gain	[-]
K_p	pitch steer coefficient	[-]
K_q	flow gain	[-]
K_r	roll bar stiffness	[-]
K_s	spring stiffness	[-]
K_ϕ	vehicle roll stiffness	[-]
$K_{\delta\theta}$	controller steering gain	[-]
K_θ	tilt angle demand gain	[-]
L	wheel base	[m]
l	distance between front tyre contact patch and tilt bearing	[m]
m_1	mass supported by front axle	[kg]
m_2	mass supported by rear axle	[kg]
m_c	cabin mass	[kg]
m_r	rear module mass	[kg]
M_{cab}	cabin moment about roll axis	[Nm]
M_{rear}	rear module moment about roll axis	[Nm]
P_s	hydraulic supply pressure	[Nm^{-2}]
P_p	hydraulic piston pressure	[Nm^{-2}]
P_r	reservoir pressure	[Nm^{-2}]
q	flow into actuator	[m]
q_c	flow into actuator due to oil compressibility	[m]
R	corner radius	[m]
R_y	lateral reaction force at tilt bearing	[m]
R_z	vertical reaction force at tilt bearing	[m]
r	yaw rate	[rads^{-1}]
S_h	'Magic Formula' horizontal shift	[-]
S_v	'Magic Formula' vertical shift	[-]
T	rear wheel track	[m]
T_{act}	actuator torque	[Nm]
t	time	[s]
u	forward velocity component	[ms^{-1}]
v	lateral velocity component	[ms^{-1}]
V	vehicle velocity	[ms^{-1}]

V	fluid volume in single actuator	[m^3]
V_{hyd}	hydraulic volume of actuator in central position	[m^3]
W_f	front axle weight	[N]
W_r	rear axle weight	[N]
α_f	front tyre slip angle	[rad]
α_r	rear tyre slip angle	[rad]
β	bulk modulus of hydraulic fluid	[bar]
δ	resultant steer angle	[rad]
δ_f	front steer angle	[rad]
δ_r	rear steer angle	[rad]
δ_{pitch}	steering due to pitching of vehicle	[rad]
γ	camber angle	[rad]
ϕ	roll angle of rear module	[rad]
ψ	yaw angle	[rad]
θ	relative tilt angle between cabin and rear module	[rad]
θ_e	effective tilt angle of cabin	[rad]
θ_{ss}	steady state tilt angle of cabin	[rad]
w	rotational speed	[$rads^{-1}$]
ξ	tilt axis inclination	[rad]

Chapter 1

Introduction

Narrow vehicles are a promising alternative to address increasing traffic congestion and pollution in urban environments. The low weight and reduced aerodynamic drag due to the small frontal area means that the fuel consumption and carbon dioxide (CO_2) emissions of this class of vehicle are much lower than that of a regular car. As EU car manufacturers are committed to reduce their overall fleet emissions to 130g/km by 2015 with a long term target of 95g/km for the year 2020 [1], a small vehicle with emissions equivalent to that of a motorcycle would greatly aid the companies to reach these targets. The increase in congestion has already led to numerous commuters turning to motorcycles. In Britain, the availability of bus lanes for motorcyclists has also contributed to this trend. However, manoeuvring a motorbike requires special skill from the driver, making it necessary to obtain a motorcycle specific driving licence. The majority of commuters also feel that these vehicles do not offer enough protection from the elements and from collisions [2]. In order for narrow vehicles to be an acceptable alternative, these vehicles should retain the comfort and safety of today's average passenger car.

To provide these levels of comfort and safety, it is crucial that the driver and passenger are fully enclosed in a weather tight structure which also protects them against potential impact situations. The implementation of this comes with considerable challenges. Due to the small track of narrow vehicles, they are very prone to rollover. In order for the driver to steer the vehicle like a conventional car, active tilt control systems must be implemented. These play an essential part in assisting the driver in balancing the vehicle while cornering as well as keeping the vehicle upright when stationary.

A proof-of-concept vehicle aiming to achieve the previously mentioned targets was developed at the University of Bath from 2003 to 2006. The vehicle was designed and constructed as part of an EU funded project comprising nine industrial companies and academic institutions from across Europe. The vehicle uses an electronically controlled hydraulic direct tilt control system. However, it was shown that the transient state stability was a considerable issue affecting the safe operation of the vehicle. It has been shown that steer tilt control systems can perform well at higher speeds in steady and transient states. However, low speed stability cannot be achieved with such systems. Recent work has therefore been focused on combining the two systems to achieve stability across the speed range, although a successfull system remains to be implemented.

1.1 Literature Review

The concept of tilting three-wheeled vehicles has been around for several decades. Work on three-wheel tilting cars can be traced back to as early as 1968. Li et al. [3] recognised the advantages of narrow track vehicles and tilting as a means of preventing these vehicles from rolling over. General Motors developed what is thought to be the first tilting three-wheeled prototype vehicle, named the Lean Machine [4]. The tilting was operated by by the driver through the use of foot pedals. Garrison and Pitstick did some of the earliest work on the potential for transition of regular cars to this type of vehicle [5]. Since then a number of concepts have been developed which has led to the need to classify these into different categories according to their layout and control method. Passively controlled three wheeled vehicles are controlled by the driver in a similar fashion to a motorbike, where counter-steer inputs are used to cause the vehicle to lean into the corner. However, a fully enclosed vehicle that is operated as a car would require active control.

There are two basic types of active control systems that can be employed: Direct Tilt Control (DTC), in which an actuator is used to tilt the vehicle and Steer Tilt Control (STC), where a steer-by-wire system is used to control the steering of the vehicle. The disadvantage of steer tilt control is that it necessitates the vehicle to be in motion to maintain stability. When the vehicle is stationary there is nothing to support the cabin from falling over. This is why DTC is most commonly found on actively controlled tilting vehicles. Recent work, however, has shown that DTC can lead to instability at higher driving speeds ([6],[7],[8]). This has led to the demand for a combined strategy which provides safe handling at all driving speeds. Some early attempts at combining

both tilting strategies by So et al. [9] led to conflicts in the controllers and a later attempt [10] resulted in a system using logical switches to switch between control methods. This however led to poor response around the switching points. The most successful dual control strategy to date is presented by Kidane et al. [6] where weighting functions are used to smoothly switch from one control mode to the other. It was shown to be successful in simulation but remains to be proven in practice. The system proposed by the author combines both steer and tilt control synchronously across all vehicle speeds, removing the need for switching strategies or transition phases.

1.1.1 Classification of Tilting Three-Wheeled Vehicles

The first way to classify the vehicle is by its layout, i.e. whether it has its two wheels at the rear or at the front and how many of its wheels tilt. For example the vehicles in figure 1.1 (b) and figure 1.2 (a) & (c) all have 1 tilting front wheel and a static rear module and are therefore all classified as 1F1T (1 front, 1 tilting wheel) and those in figure 1.1 (c) and figure 1.2 (b) as 2F3T. More importantly, however, is the control method of these vehicles. The various control methods are discussed below.

Passive Control

The simplest layout for a tilting three wheeler is to have passive tilt control. Vehicles with this type of layout tend to be derivatives of motorcycles and scooters where the driver controls the tilting motion of the vehicle. Although these bring added safety and stability to its two-wheeled counterparts, they generally don't offer the protection of a closed compartment. Furthermore, they require a certain amount of driver skill similar to that required to control a two wheeled vehicle, where the driver uses counter steering to tilt the vehicle in the corner. This is a (mostly subconscious) technique where, in order to initiate a turn, the rider momentarily steers out of the corner. This creates a moment large enough to tip the vehicle into the corner. Once the vehicle is leaning into the corner, the driver adjusts the steer angle until the vehicle reaches a steady state.

The Calleja by Prodrive (figure 1.1 (a)) and the Honda Gyro Canopy (figure 1.1 (b)) are examples of these. Most recently Piaggio brought out its quite successful Hybrid X8 and MP3 three wheeled scooters and Gilera released its near identical FUOCO 500ie (figure 1.1 (c)).

(a) (b) (c)

Figure 1.1: Three-wheelers with passive control: (a) Calleja (b) Gyro Canopy (c) FUOCO 500ie

As this type of three-wheeler doesn't offer the desired comfort or protection the average commuter desires, and requires additional driver skill (and possibly an extra licence) it is not likely to create a significant impact on the choice of transport of today's driver.

Active Control

By having active control systems no special skills are required of the driver other than those to drive a car. There are two basic types of control systems that can be employed, DTC and STC.

With STC systems, the vehicle is inherently unstable at low speeds as it has nothing supporting its tilting element. It therefore requires an additional system to either lock the vehicle or provide a balancing torque. DTC vehicles on the other hand, can reach equilibrium during all driving conditions and do not need additional mechanisms to provide stability at low speeds. The most commonly found control method is therefore direct tilt control. DTC systems typically use electrical or hydraulic systems to provide the actuation energy. Hydraulics are preferred due to their high power density and because the pump can be driven directly off the engine. DTC systems typically consume up to 1.5kW in peak conditions and around 400W in average driving conditions [11]. If an electric motor were to be used in either a direct drive configuration or to drive a hydraulic pump, a 12V electrical system would require current peaks of up to 125 A. It would therefore not be a viable option for a 12V electrical system.

In a DTC system it is crucial that the system responds before excessive lateral acceleration builds up. Using the steering input of the driver to initiate tilting before the

(a) (b) (c)

Figure 1.2: Three-wheelers with active control: (a) CLEVER (b) F300 Life-Jet (c) CARVER

tyres start producing any cornering force is therefore common. However, it is shown in this thesis that this is only achieved with limited success and that lateral acceleration transients contribute significantly to the instability of DTC vehicles. Figure 1.2 shows some of the vehicles that have successfully implemented a DTC system.

Recent work has focused on the possibility of combining the two control methods, using STC at high vehicle speeds for lower power consumption and reduced transients while DTC provides the required stability at low speed. This is referred to as dual-tilt control or SDTC.

1.1.2 Previous and Contemporary Work on Tilting Vehicles

Several of the three-wheeled concepts previously mentioned have been developed in industry, resulting in a very limited amount of literature and documentation regarding these vehicles. The F300 Life-Jet concept by Mercedes Benz shown in figure 1.2(b) was unveiled at the 1997 Frankfurt Motor Show. The tilting was controlled by a hydraulic direct tilt control system which utilised information from various sensors measuring the driver's steering input, speed, yaw rate and actuator position to calculate the required tilt angle. The vehicle never made it into production and research done on the vehicle is restricted to Daimler AG. From a control point of view, this vehicle resembles the CLEVER vehicle developed at the University of Bath and could have provided valuable information on control methods.

The vehicle shown in figure 1.2(c) is the CARVER developed by Dutch engineers Chris van den Brink and Harry Kroonen. The vehicle is similar to CLEVER in that both

Institution	Layout	Control	Status
University of Bath	1F1T	DTC	working prototype
University of Minnesota	2F3T	SDTC	working prototype
University of California, Davis	-	-	-
University of California, Berkeley	-	-	-
University of Padua	1F1T	Passive	working prototype
University of Delft	1F1T	DTC	in production

Table 1.1: Institutions with published work on tilting three-wheelers

are 1F1T DTC three wheelers. The main difference is that the CARVER utilises its Dynamic Vehicle Control (DVC^{TM}) technology to control the tilting and it is also wider (1.3m as opposed to 1m). The tilt control solution is based on a mechanically operated hydraulic system. A hydraulic valve opens according to the amount of steering torque at the front wheel and remains open until the steer torque is zero. The entire system was developed experimentally and is quite mechanically complex. The engineers of Brink Dynamics have published a few papers on their technology [12] [13] [14]. These, however, do not contain any data on the dynamic performance of the vehicle.

Although actively controlled tilting three-wheeled vehicles have been developed and built in the past, very little experimental work has been published on the subject. The institutions that are currently involved in research on tilting three-wheeled vehicles are summarised in table 1.1. The large majority of the work carried out at these institutions has been centred around the modelling of tilting three-wheeled vehicles in order to investigate the strategies employed to control them (STC, DTC and Dual Mode). Notable is the research based at the University of Minnesota, which has been involved with tilting three-wheel vehicles since 2002. Gohl et al. Rajamani et al. and Kidane at al. have published numerous papers on the subject of the control of these vehicles. A full size prototype was also built in 2008 [15]. Another narrow tilting vehicle prototype with four wheels arranged in a diamond shape was constructed at the National Chiao Tung University in Taiwan. The vehicle utilises a dual-tilt control stategy. However, papers published by Chiou et al. ([16], [17]) reveal little on the details of the control strategy.

In 1992 Karnopp and Fang [18] created an elementary bicycle model of a steering controlled banking vehicle, which illustrated the counter steering effect. It was suggested that this model could be used to explore unconventional vehicle concepts and bring insight into possible control strategies. Karnopp and Hibbard [19] then highlighted the differences between trains and other fixed guide way vehicles and driver steered vehicles, with respect to the desirable tilting mechanisms and the optimum tilt angle time

histories under certain criteria. Further work was then done by Hibbard and Karnopp [20] [21] on methods of controlling the lean angle of tilting vehicles where instead of using the lateral cornering acceleration as the control signal for the desired lean angle, alternative methods were investigated such as using the perceived lateral acceleration or the torque in the active tilt mechanism. In this work they demonstrated that there are two possible methods to lean a vehicle into the corner: the method of counter steering or through the use of an actuator. They showed that when the vehicle was tilted by an actuator, it is always stable in steady state, but the driver would experience elevated levels of lateral acceleration at higher speeds. When counter steering was used to lean the vehicle into a corner, the lateral acceleration experienced by the driver was close to zero. However, at lower speeds, the system would require frequent large inputs.

These findings led to further research on dual mode control switching strategies by Hibbard and Karnopp [4], So and Karnopp [10] [9] and Karnopp [22] [23]. Initially a speed dependent strategy was suggested and it was found that this system performed poorly at the switching points. Another paper was published where they introduced a system which could switch between the two tilt systems depending on the error between the demand and the output lateral acceleration. They recognised that the switching could be improved to obtain a smoother output.

Rather than using tilt-angle control based on the small slip angles assumption, Snell [24] suggested using a control method combining STC and DTC based on the feedback from accelerometers. His simulation results showed that the vehicle would turn smoothly and swiftly into the turn with very little perceived lateral acceleration and with modest actuator torque requirements. His control method aimed to minimise the perceived lateral acceleration and allowed the roll dynamics to be tuned simply by changing the location of the accelerometer. The resulting control law responded with counter steering in transient situations and an actuator moment in steady state conditions. However, the control method was never implemented and it was acknowledged that further work was required on the robustness of the strategy.

It should be noted that up to this point all the published work carried out on control strategies had been purely theoretical and were only tested in simulation. Gohl et al. [25] [26] [27], Rajamani et al. [28] and Piyabongkarn et al. [29] of the University of Minnesota recognised this lack of experimental data and produced a number of papers presenting the development of their tilting three wheel vehicle and the various control methods implemented. Their initial prototype was presented in 2002 [25] and used a direct tilt control (DTC) method to lean the vehicle into corners. The practical tests

showed that the DTC method was better than STC due to its ease of implementation and its stability at low speeds. The disadvantage was high actuator torques in transient states. This was improved by using a steer-by-wire configuration, to make sure that the tilt controller started acting before any yaw rate could be generated by the tyres. They found that the easiest method of control was to consider the driver's output as the desired lean angle. Gohl [26] went on to implement STC on the prototype. The controller was a modified version of the one suggested by Karnopp [18]. They found that active STC would be a viable method to balance a narrow vehicle and that when combined with DTC, it could be used to make a fully enclosed vehicle that would lean into corners using steering inputs similar to those for a car.

Further experimental work was carried out by Pauwelussen [30] [31] using the Carver as a basis. Pauwelussen found that parameters like the tilting axis orientation and the roll-steer characteristics of the rear part of the vehicle have a significant effect on the vehicle yaw stability. The reasons for this are discussed in detail in chapter 2.

Cossalter et al. [32] [33] developed and built a passively controlled 1F1T vehicle. This vehicle uses a four bar linkage system between the tilting front and the static rear of the vehicle. The geometry of the system could be altered in order to investigate the effects of the location and inclination of the tilt axis and the instantaneous centre of rotation. Simulations and experimental testing were used to evaluate the required steering torque and the load transfer between the rear wheels. The steering angle, steering torque, roll angle, roll rate, yaw angle and yaw rate were measured in slalom tests and used to calculate a number of comparative parameters. These were then plotted as a function of slalom frequencies for different vehicle configurations. As a result of this a new handling index was suggested based on the maximum frequency at which a driver could perform a particular manoeuvre.

The most recent attempts to combine STC and DTC were presented by Kidane et al. The first attempt [34] in 2007 used a combination of STC, DTC and a 'Tilt Brake' for low speed operation. This was followed by a second control approach [6] which removed the tilt brake and used DTC for low speed operation and STC for high speed operation. Weighting functions were used to create a smooth transition from one control mode to the other. It was shown to be successful in simulation but remains to be proven in practice.

Figure 1.3: CLEVER test vehicle at the University of Bath

1.2 The CLEVER Concept Vehicle

CLEVER is an acronym for 'Compact Low Emissions VEhicle for uRban transport'. The European Union funded project ran from 2003 to 2006 and comprised of nine industrial companies and academic institutions from across Europe. The aim of the project was to design and develop a low emission alternative vehicle for city travel by combining the comfort and safety of a small car with the road footprint of a motorcycle. In total, five prototypes were built. Three were used for crash testing, one is a show vehicle belonging to BMW and the final one is located at the University of Bath and is used for further research (figure 1.3).

In order for CLEVER to appeal to a significant proportion of motorists, it is important for it to have the same controls as a conventional car and not require further training or development of skills, as required for motorcycles. To keep consumption and road space to a minimum, the vehicle's external dimensions were fixed to 1 metre wide, 3 metres long and 1,4 metres high. These design restrictions come with considerable challenges in terms of vehicle dynamics and control.

1.2.1 Wheeltrack and Rollover

In order to prevent a vehicle from rolling over, it is important to keep its centre of gravity as close as possible to the ground. This is especially important for vehicles with a narrow wheel track.

Figure 1.4 (a) shows the rear of a narrow vehicle with the forces acting upon the

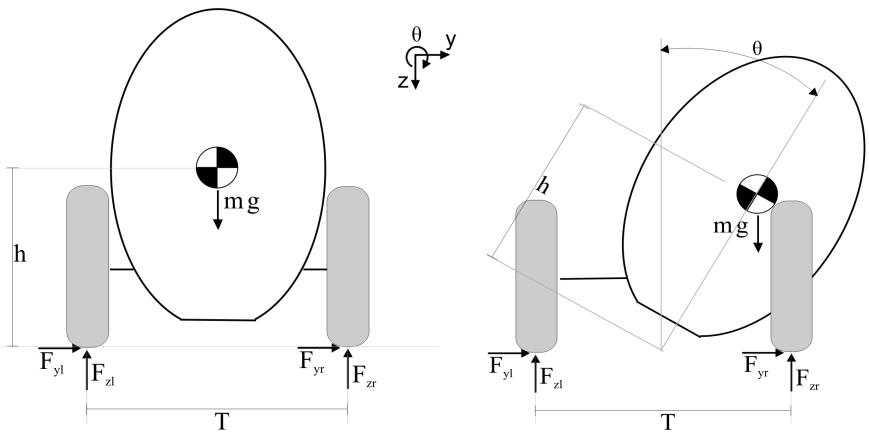

Figure 1.4: Forces acting on a narrow vehicle

vehicle during a steady state turn to the right. Assuming that the tyres will not slide, the maximum lateral acceleration application before roll over can be calculated when the vehicle is on the limit of rollover, when $F_{zr} = F_{yr} = 0$. Taking moments around the centre of gravity:

$$\sum M_{cg} = \frac{F_{zl}T}{2} - F_{yl}h = 0 \tag{1.1}$$

In this limiting condition, the weight of the vehicle is supported completely by the left hand tyres:

$$F_{zl} = mg \tag{1.2}$$

and the cornering force on the left hand tyres is equal to the force due to the lateral acceleration:

$$F_{yl} = mw^2R = \frac{mV^2}{R} = ma_y \tag{1.3}$$

Combining equations 1.1, 1.2 and 1.3, the maximum lateral acceleration, $a_{y,max}$ is governed by equation 1.4

$$a_{y,max} = \frac{gT}{2h} \tag{1.4}$$

This shows that for a four-wheeled vehicle with equal front and rear track, the maximum achievable lateral acceleration is determined by the ratio of half the wheel track and the height of the centre of mass. A modern tyre has an adhesion limit that will generate maximum forces equating to a lateral acceleration of approximately 10 m/s^2 and any vehicle should therefore be designed to have a rollover limit higher than this. For a narrow vehicle such as CLEVER, with a wheel track of 0.8m, this would equate to having a centre of gravity height of 0.4m. To achieve this it would be necessary to position all the vehicle components and the driver very low to the ground. This would have a detrimental effect on accessibility, ground clearance and leave the driver feeling very vulnerable towards other vehicles.

By tilting the centre of mass towards the centre of the curve, the vehicle's tendency to overturn is reduced. Figure 1.4 (b) show the same vehicle but with its body tilting into the corner. In this example, the tilt axis is located at ground level. Taking moments about the CoG again:

$$\sum M_{cg} = F_{zl}\left(h\sin\theta + \frac{T}{2}\right) - F_{yl}h\cos\theta = 0 \tag{1.5}$$

This results in the expression describing the maximum lateral acceleration:

$$a_{y,max} = \frac{g(h\sin\theta + \frac{T}{2})}{h\cos\theta} \tag{1.6}$$

It can be seen that $a_{y,max}$ is now a function of the tilt angle. This gives a lot more scope for the location of the centre of gravity without affecting the cornering capabilities of the vehicle.

It should be noted that with three-wheeled vehicles, the axis about which the vehicle will roll isn't in the centre of the vehicle, but about the line joining the front wheel to the rear tyre which is on the outside of the curve (the dotted line in figure 1.5). As the centre of mass will be located somewhere between the front and the rear wheels, the track of the rear wheels must be multiplied by the ratio of the longitudinal position of the centre of mass a and the wheelbase of the vehicle L to obtain its distance from the

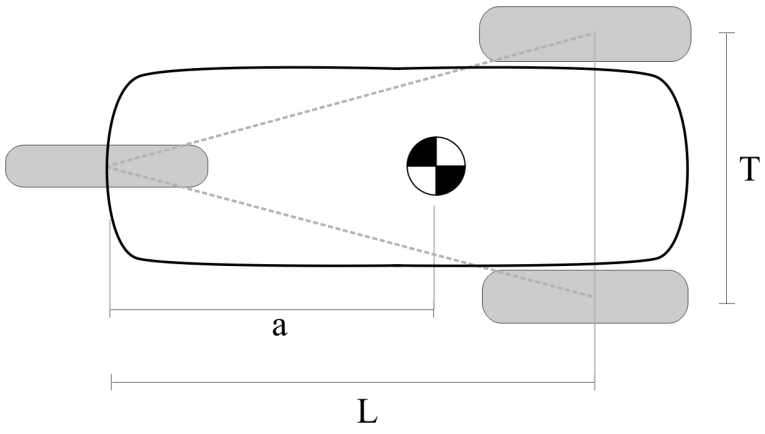

Figure 1.5: Plan view of a three-wheeled vehicle

roll axis of the vehicle. It is assumed that that the vehicle is symmetrical. Including this term, equation 1.6 becomes:

$$a_{y,max} = \frac{g(h\sin\theta + \frac{T}{2}\frac{a}{L})}{h\cos\theta} \tag{1.7}$$

As $\frac{a}{L} < 1$ the resistance to roll-over of a three-wheeled vehicle is less than that of four-wheeled vehicle. In the event of a 1F1T vehicle braking in a corner, the likelihood of the vehicle rolling over is increased even more as the weight of the vehicle is shifted towards the front reducing the ratio of $\frac{a}{L}$ even further. Shifting the centre of mass is therefore a necessity to ensure the stability of a narrow track three-wheeled vehicle.

The implementation of the control system required to achieve the tilting action and the unique dynamics associated with the three-wheeled vehicle are discussed in detail in chapter 2.

1.3 Thesis Structure

After having discussed the driving forces behind the research on narrow tilting vehicles and the underlying principles associated with them, the CLEVER concept vehicle will be covered in detail. Chapter 2: *Kinematics and Control of the CLEVER Concept Car* is primarily a review of the work of Barker [11] and Drew [35] on the development of the CLEVER car. The fundamental operating principles, which will be referred to through-

out the thesis, are presented and observations on areas for potential improvement are made.

Barker and Drew had observed in experimental tests that the transient behaviour could lead to instability of the vehicle and ultimately to roll-over, although the dynamics which lead to this were not fully understood. In order to create a better understanding of the transient roll dynamics, a five degree-of-freedom (DoF) model was initially developed in a Simulink environment, where roll motion of the vehicle was determined by the angular motion of the cabin and rear module and the vertical motion of the wheels. Furthermore, the individual nature of the CLEVER vehicle meant that much remained to be learned about the ride characteristics of this type of vehicle. The principal modes could be decoupled due to the vehicle symmetry and the resonant frequencies of the principal modes could be determines using a number of single mass models.

The vertical and roll dynamics of the vehicle were subsequently tested using a three-post rig where each wheel was individually actuated by a vertical hydraulic actuator. As the resultant dynamics were significantly more complex than anticipated, the vehicle model was extended to a multi-body model using the SimMechanics package. In the next stage, a model was created for the lateral dynamics of the vehicle and validated using experimental data obtained at a local test track. The development and validation of the full vehicle model is detailed in chapters 3 to 5.

The limiting stability conditions in steady and transient state are then discussed in chapter 6. The steady state dynamics can be represented using a two DoF model, whereas the full vehicle model is used to look at the transient state dynamics. This leads to a lateral dynamics optimisation study based on an arbitrary function to describe the tilting profile. The results of the optimisation study prove that independent control of the front steering wheel is required for optimal handling and stability.

In the chapter 7, a linear vehicle model is presented along with the proposed control method. Based on the results from chapter 6, a dual-control (SDTC) system is proposed. The linear model permits a frequency domain analysis of the control systems. The frequency domain analysis gives further insight in the transient stability issues presented in chapter 6 and the current and proposed control systems are compared. Parameters of the new control method are optimised in the frequency domain. The two systems are then compared in the time domain and the new control approach is tested for robustness using the full non-linear vehicle model.

The overall objectives of this thesis and how they were achieved are listed below:

1. **Investigate how the roll dynamics are affected by the current direct tilt control set-up**

   - A five degree of freedom model is developed in Simulink in chapter 3, where the roll motion of the vehicle is determined by the angular motion of the cabin and rear module and the vertical motion of the wheels.
   - The principal elements of the model are then incorporated in a more sophisticated multi-body model in order to include pitch and bounce effects.

2. **Investigate the ride characteristics of the vehicle**

   - A series of one and two degree of freedom models are developed in chapter 3 to investigate the ride characteristics in pitch, roll and bounce and the principal natural frequencies are determined. It was possible to decouple the different modes due to the vehicle symmetry.
   - The vehicle is tested on a three-post rig, where each wheel is vertically displaced by a hydraulic actuator. The results and comparison with the multi-body model are presented in chapter 4.

3. **Create a full non-linear vehicle model to investigate the combined handling and tilting dynamics and test the proposed control method**

   - Chapter 5 details the development of the lateral dynamics model. The model is based around a bicycle model and is developed to include non-linear tyre characteristics and load transfer across the rear axle. The model is validated using test data obtained at a local test track.
   - The lateral dynamics model is incorporated in the multi-body model. In Chapter 6 the complete model is used to present the dynamic effects that can lead to the transient state roll-over of the vehicle.
   - Finally, the complete model is used to compare the performance of the proposed controller with the original controller.

4. **Develop an improved control method**

   - In chapter 6 an optimisation study is performed based on a two degree of freedom system using an arbitrary function to describe the tilting profile. The tilting function is optimised for a range of initial conditions and it is

shown that an optimum solution can only be achieved with independent control of the front wheel.

- A new type of combined steer and tilt control is proposed in chapter 7 and a linear vehicle model is developed in order to analyse the controller in the frequency domain and compare it to the performance of the original controller.

Chapter 2

Kinematics and Control of the CLEVER Concept Car

The following chapter details the handling characteristics of a tilting three wheeler of the 1F1T configuration such as CLEVER through the use of a linear vehicle handling model. This linearised model was used as the basis for design of the vehicle in its current form. The principal kinematic effects required for neutral handling characteristics and the current method of actuation and control are discussed. This chapter summarises the work done by Barker [11] and Drew [35] and discusses the limitations of the current set-up and the scope for improvement within the current structure of the vehicle.

A neutral handling performance can be achieved by the inclination of the tilt axis which resulted in tilt-dependent rear-wheel steering. If the vehicle has a neutral handling characteristic, the steering angle remains close the Ackerman angle and as result it can be used along with the vehicle speed to get an estimate of the lateral acceleration. The aim of the controller used on the CLEVER prototype is to tilt the cabin such that the lateral and gravitational acceleration components acting on the cabin are balanced. This is achieved through the use of two single-ended actuators mounted on the rear module.

2.1 Steady State Characteristics

In order to maintain stability with the narrow wheel-track of the vehicle, CLEVER is set up to lean into corners in a similar fashion to a motorbike. A motorcycle rider must lean the vehicle into a corner in order to balance the moment caused by the vehicle lateral acceleration a_y and the moment caused by gravity. This angle is referred to as the equilibrium or steady state angle, θ_{ss}:

$$\theta_{ss} = tan^{-1}\left(\frac{a_y}{g}\right) \approx \frac{a_y}{g} \tag{2.1}$$

The aim of the original control method is to recreate a similar situation with CLEVER. The ultimate objective is to always have the forces resulting from the lateral acceleration balance with the gravitational force. However, it should be noted that as the rear module of the vehicle does not tilt, the cabin would have to lean past this balancing point in order for the rear axle lateral load transfer to be reduced to zero.

As a result of the combination of a car-like setup at the rear and that of a motorbike at the front, a 1F1T vehicle such as CLEVER has handling characteristics unlike those of a car or motorbike [7]. Due to the high cornering forces at the front wheel as a result of camber thrust, the vehicle would considerably over-steer. In order to obtain neutral handling characteristics, it was necessary to introduce additional rear-wheel steer to offset the effects of the front wheel camber. The required rear-wheel steer was derived from a linearised bicycle model [11]. This model represents the two rear wheels of the vehicle as a single rear wheel with twice the cornering force (figure 2.1). The variable V denotes the forward velocity of the vehicle, R is the radius of the turn, L is the wheelbase and a and b are the distances to the vehicle centre of gravity (CoG) of the front and rear tyre contact patches. The angles ψ, δ_f, α_f and α_r denote the yaw angle, the front steering angle and the front and rear slip angles respectively.

The fundamental steer equation based on small angle approximations is given in equation 2.2. At low speed ($V \to 0$), α_f and α_r are small and the steer angle δ_f required to negotiate a turn tends to $\frac{L}{R}$ [36]. This is referred to as the Ackerman angle. At higher speeds, tyre slip increases and the steering angle deviates from this idealised condition. The slip angles can be written with respect to the lateral acceleration as shown in equations 2.3 and 2.4. The variables m_1 and m_2 represent the front and rear effective axle mass. $C_{\gamma f}$, $C_{\alpha f}$ and $C_{\alpha r}$ represent the front camber coefficient, the

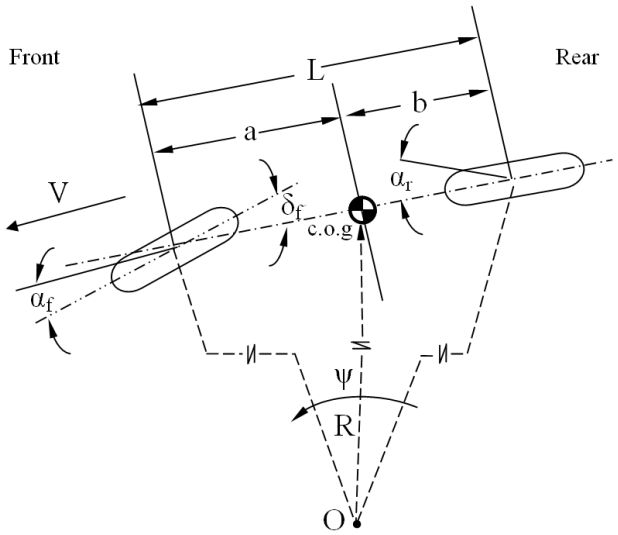

Figure 2.1: Bicycle model

front slip-stiffness and rear slip-stiffness respectively. The initial assumption was made that the camber angle is equivalent to the tilt angle θ. Equations 2.3 and 2.4 can be substituted into equation 2.2 and R can be replaced by $\frac{V^2}{a_y}$. This then yields the new equation for a steady state steer response, equation 2.5.

$$\delta_f = \frac{L}{R} + (\alpha_f - \alpha_r) \tag{2.2}$$

$$\alpha_f = \frac{m_1 a_y - C_{\gamma f}\theta}{C_{\alpha f}} \tag{2.3}$$

$$\alpha_r = \frac{m_2 a_y}{2C_{\alpha r}} \tag{2.4}$$

$$\delta_f = \frac{L a_y}{V^2} + (\frac{m_1 a_y - C_{\gamma f}\theta}{C_{\alpha f}} - \frac{m_2 a_y}{2C_{\alpha r}}) \tag{2.5}$$

Using typical tyre data for a front motorcycle tyre (120/70R17) and rear car tyres (195/65R15) [11], graphs of steer and slip angles vs lateral acceleration were plotted for constant radius turns, shown in figure 2.2. These illustrate that the vehicle would considerably over-steer. This is due to the front tyre generating the majority of the cornering force through camber. The front slip, rear slip and camber angles remain

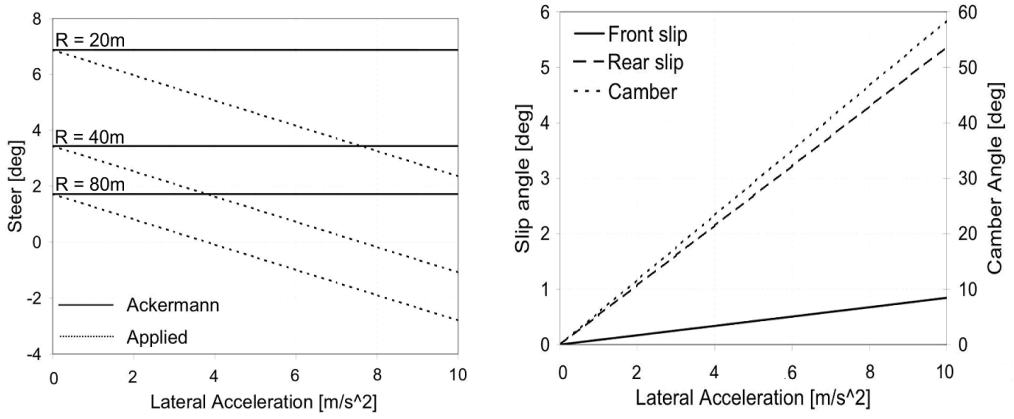

(a) (b)

Figure 2.2: Steady state cornering characteristics [11]

the same for all turn radii because the equations used have been linearised. The linearisation means that the angle approximations become less accurate as the lateral acceleration increases. Similarly, the camber angle is higher than 45 °at 10 m/s^2 cornering because of the linearised tangent function in equation 2.1.

To compensate for the significant oversteer, it is necessary that the rear wheels steer into the corner as the cabin leans. This rear steer is proportional to the tilt angle (equation 2.6). Adding the latter to the front steer angle results in the total steer angle δ as shown in equation 2.7. Rewriting this in the form of equation 2.5 and substituting for θ using equation 2.1, it is possible to differentiate with respect to the lateral acceleration yielding what has been decribed as the oversteer estimation [11] in equation 2.8. From this oversteer estimation, the rear steer gain $K_{\delta r}$ can be calculated (equation 2.9).

$$\delta_r = K_{\delta r}\theta \tag{2.6}$$

$$\delta = \frac{L}{R} + (\alpha_f - \alpha_r) + \delta_r \tag{2.7}$$

$$\frac{d\delta}{da_y} = \frac{L}{V^2} + \frac{m_1 g - C_{\gamma f}}{C_{\alpha f} g} - \frac{m_2}{2C_{\alpha r}} + \frac{K_{\delta r}}{g} \tag{2.8}$$

$$K_{\delta r} = \frac{m_2 g}{2C_{\alpha r}} - \frac{m_1 g - C_{\gamma f}}{C_{\alpha f}} \tag{2.9}$$

2.2 Motion about the Tilt Axis

The orientation and height of the tilt bearing has a number of effects on the kinematics of the vehicle. Most importantly it can be used to introduce tilt-dependent rear-wheel steer. The position of the tilt bearing also affects the location of the cabin roll axis and therefore the angular motion of the cabin relative to the ground. It is important not to confuse the tilt bearing inclination or tilt axis with the cabin roll axis and the vehicle and rear module roll axis. Figure 2.3 depicts each of these against an outline of the CLEVER vehicle.

2.2.1 Rear Steer and Tilt Axis Inclination

In the previous section it was shown that the rear wheels need to steer as the cabin tilts in order to achieve neutral handling characteristics. This was achieved through the inclination of the tilt axis. This effect can be explained through trigonometry by looking at figure 2.3. Figure 2.3 shows a side and top view of the CLEVER car with a positive tilt axis inclination ξ. With a horizontal tilt axis, there is an angle ξ_0 between the tilt axis and the roll axis. On CLEVER, ξ_0 corresponds to 7.9°. Therefore, a tilt inclination of ξ of -7.9° would mean the tilt axis would be in line with the cabin roll axis and there would be no rear-wheel-steer. The perpendicular distance from the tilt-axis to the front tyre contact patch is given by:

$$r = l \sin(\xi_0 + \xi) \tag{2.10}$$

If the cabin tilts through an angle θ about the tilt axis, this will lead to a lateral displacement y of the front tyre contact patch equal to $-r \sin\theta$. Therefore, the distance l_x along the x-axis between the tilt bearing and the front tyre contact patch is given by:

$$l_x = \sqrt{a_\theta^2 - (r \sin\theta)^2} \tag{2.11}$$

Finally, the rear wheel steer angle δ_r (positive from the line joining the front and rear axle) is given by:

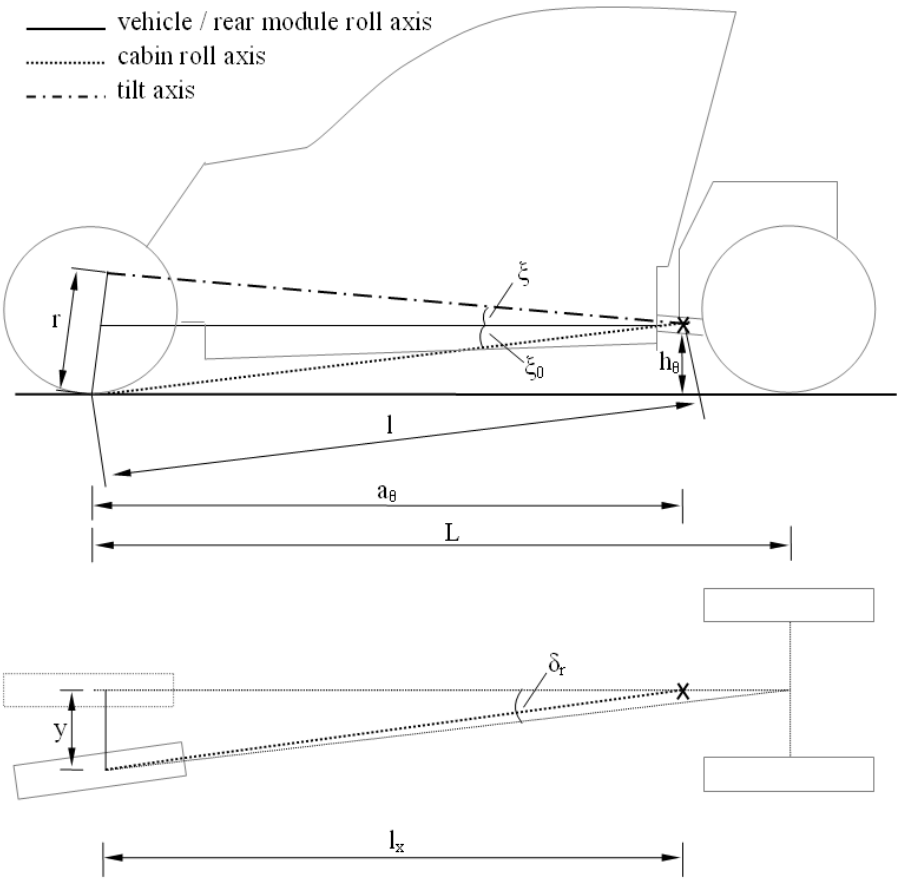

Figure 2.3: Tilt axis height and inclination and front and rear module roll axes

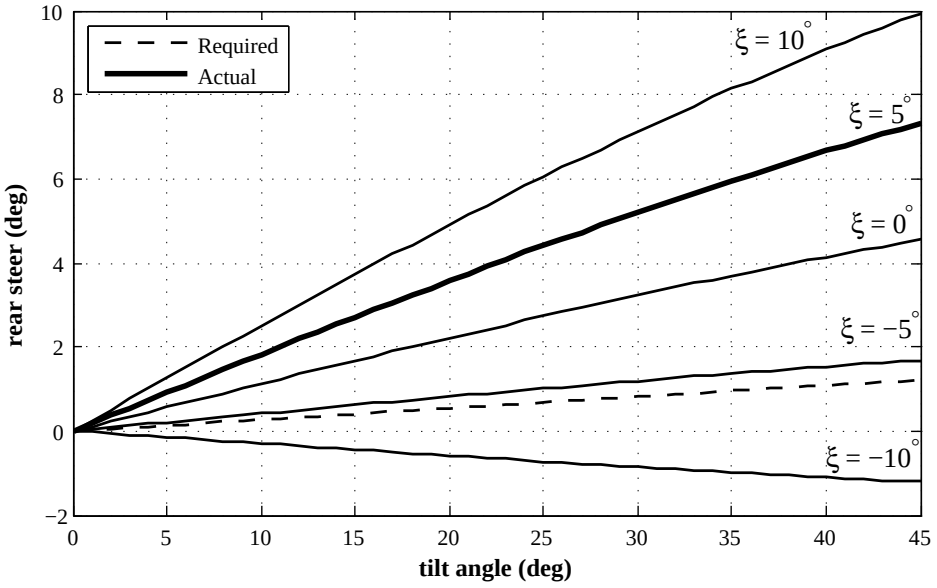

Figure 2.4: Tilt axis effect on rear wheel steer

$$\tan \delta_r = \frac{y}{L} = \frac{l \sin(\xi_0 + \xi) \sin \theta}{L - a_\theta + l_x} \tag{2.12}$$

The rear-wheel steer against tilt angle for a range of tilt-axis inclinations is shown in figure 2.4. The effects of tyre conicity are not taken into account, as these are comparatively small. As mentioned previously, if $\xi = -\xi_0$ = -7.9° there would be no rear-wheel-steer. If the tilt axis angle is smaller than $-\xi_0$, the rear wheels will steer away from the turn. The dashed line shows the necessary inclination to satisfy equation 2.9 for neutral steering and the bold line represents the tilt axis inclination in CLEVER. These do not coincide as the consequences of the tilt axis kinematics were not fully understood at the design stage. The new results are in line with the lateral dynamics performance measured in chapter 5. As a result, the prototype vehicle has an under steering handling characteristic.

2.2.2 Tilt Axis Height and Resultant Tilt Angle

Due to the raised tilt axis, the angle at which the cabin tilts relative to the rear module isn't equal to the absolute tilt angle relative to the ground. This is illustrated in figure 2.5. The relationship between the relative θ and the absolute θ_e tilt angle is given

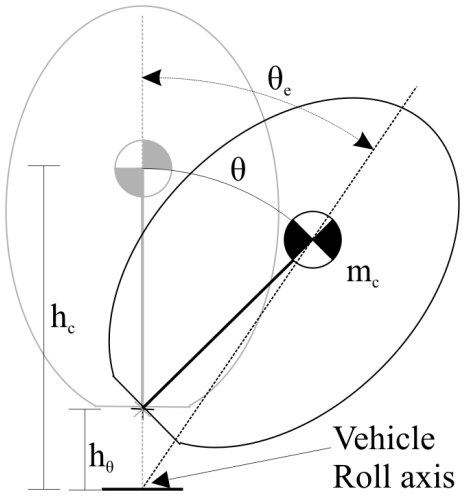

Figure 2.5: Effective tilt angle with raised tilt axis

in equation 2.13 and linearised using a small angles approximation in equation 2.14.

$$\tan\theta_e = \frac{(h_c - h_\theta)tan\theta}{h_c} \tag{2.13}$$

$$\theta_e = \left(1 - \frac{h_\theta}{h_c}\right)\theta \tag{2.14}$$

As the cabin roll axis runs from the tilt bearing to the contact patch of the front tyre, the effective height about which the CoG rotates depends on its longitudinal distance along the cabin roll axis. Using a linear estimation and not including geometrical effects at the tilt bearing, the effective tilt angle is therefore given by equation 2.15.

$$\theta_e = \left(1 - \frac{h_\theta}{h_c}\frac{a_c}{a_\theta}\right)\theta \tag{2.15}$$

where a_c and a_θ are the longitudinal distance of the tilting centre of mass and the tilt bearing from the front tyre contact patch respectively. Using values for CLEVER with a driver only ($h_\theta = 0.271, h_c = 0.540, a_c = 1.155, a_\theta = 1.953$) gives a value of 0.71 for the expression in brackets, indicating that the tilting position only achieves 71% of the required value for the balanced condition. Using the kinematic model developed by Barker [11] gives a more accurate estimate of 82% . In order to compensate for this,

the vehicle must overlean by approximately 18% . Further overlean is also required to compensate for the rear suspension roll.

2.2.3 Pitch Steer

When the vehicle pitches forward, the tilt axis angle is reduced, which in turn leads to smaller levels of rear wheel steer. As the steering of the rear wheels reduced the overall steer angle, the so-called 'pitch steer' can be represented as additional steer (equation 2.16).

$$\delta_{pitch} = K_p x_f \theta \tag{2.16}$$

The deflection of the front suspension, x_f, from the design position is given in equation 2.17. This is obtained from resolving the forces along the line of action of the front suspension springs as shown in figure 2.6 (a). The term $\frac{gm_1}{K_f}$ accounts for the deflection due to the pre-load.

$$x_f = \frac{\sin(\theta - \phi)a_y m_1 + \cos(\theta - \phi)gm_1 - gm_1}{K_f} \tag{2.17}$$

The additional steer as a function of the lean angle over the compression range of the front suspension is shown in figure 2.6 (b). It does not take into account the toroidal shape of the front tyre. When the vehicle is leaned to large angles, further pitch is introduced due to the the reduction in diameter at the edges of the tyre. For a 120/60R17 tyre as used on CLEVER, this could be equivalent to an additional 30mm compression of the suspension at 45° lean angle [11].

The pitch steer effects are most noticeable with high radius, high speed corners. In these conditions small steer angles are applied at a high velocity and due to the linearity of the controller, these conditions result in a smaller tilt angle for a given lateral acceleration. This maximises the value of $\sin(\theta - \phi)a_y m_1 + \cos(\theta - \phi)gm_1$ in equation 2.17.

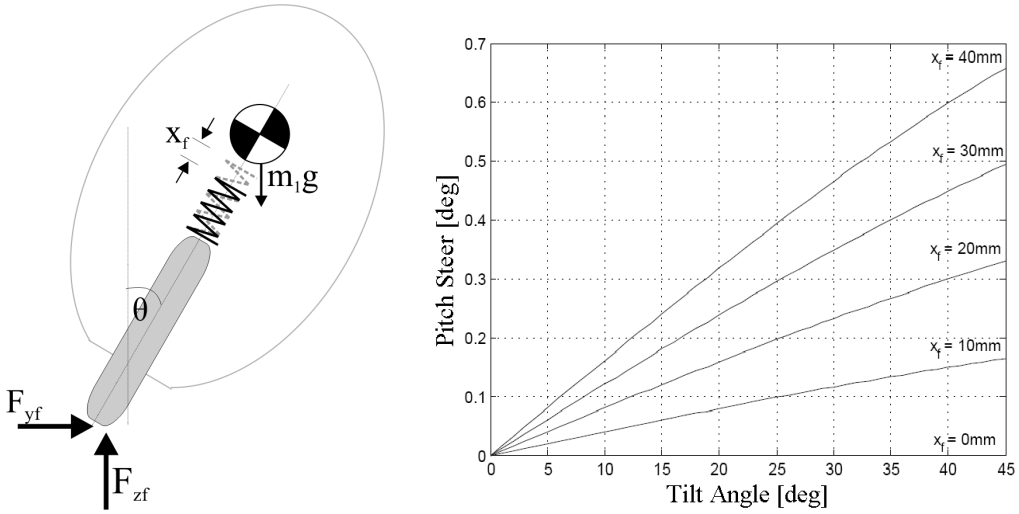

(a) (b)

Figure 2.6: (a) Free body diagram of front tyre and suspension (b) Pitch steer effects

2.3 Active Direct Tilt Control

2.3.1 Hydraulic Actuation

In order to stabilise the vehicle during cornering, CLEVER has an active direct tilt control system. The hydraulic circuit was designed to control the position of the tilting part of the vehicle with two single acting linear hydraulic actuators. When pressurised, these cylinders control the lean angle of the tilting cabin by rotating it with respect to the rear module. A proportional directional control valve with a closed centre position modulates the flow to the actuators, controlling their position and locking the cylinders when no command is given. A diagram of the full circuit is shown in figure 2.7.

Flow in the system is provided by a gear pump driven directly from the engine crankshaft. In order to unload the pump, augment the flow and provide flow in the event of pump or engine failure, an accumulator was incorporated in the circuit in conjunction with an unloading valve. When the desired system pressure is reached, the unloading valve opens, allowing flow generated by the pump to return to tank, decreasing the torque demand on the engine. When the accumulator has discharged and the pressure in the system falls below a minimum threshold value, the unloading valve closes, directing flow from the pump back to the system to charge the accumulator until maximum system pressure is reached. Two pilot operated check valves mounted in a cross-port manifold are implemented between the actuators and the control valve so that the actuators are

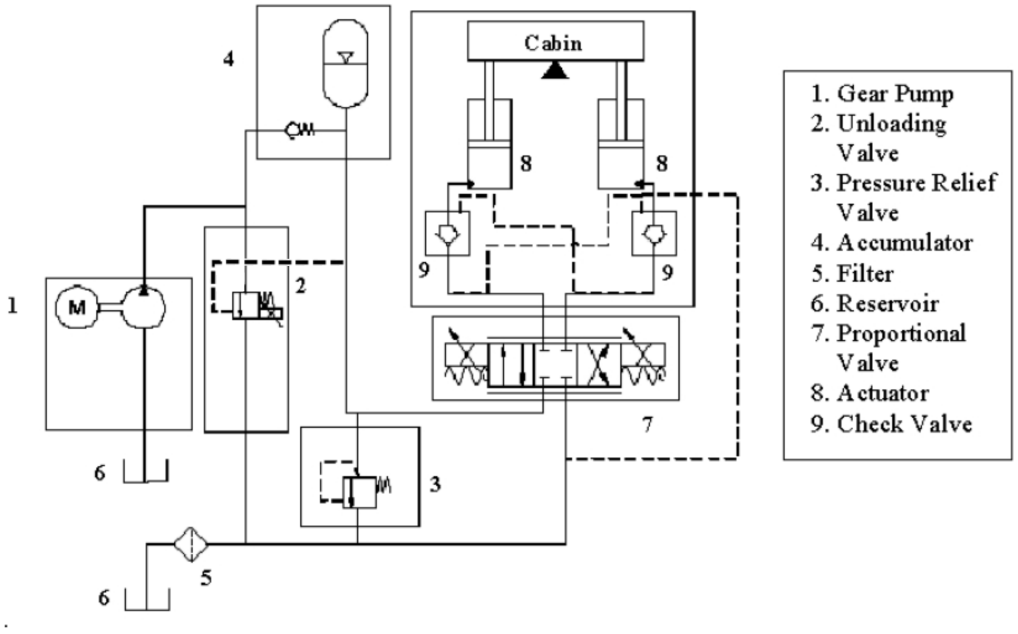

Figure 2.7: Hydraulic circuit on CLEVER [11]

Parameter	**Symbol**	**Value**
Supply pressure	P_s	160 bar
Piston area	A_p	$8.042 \cdot 10^{-4}\text{m}^2$
Average actuator lever arm	$b_{\theta,mean}$	0.127 m
Maximum actuator lever arm	$b_{\theta,max}$	0.144 m
Minimum actuator lever arm	$b_{\theta,min}$	0.085 m

Table 2.1: Hydraulic Circuit Specification

locked when the valve is closed, and any leakages across the ports in the valve does not affect the tilt angle. The bandwidth of these pilot operated check valves is sufficiently high not to affect the dynamic performance of the tilting system [35].

$$T_{max} = P_{max} A_p b_\theta \tag{2.18}$$

Using the data given in table 2.1, it is possible to calculate torque generated by the actuators according to equation 2.18. The maximum torque at the maximum and minimum lever arm can be found to be 1853Nm and 1107Nm respectively.

2.3.2 Closed Loop Control

The controller currently implemented is a simple proportional controller with closed loop feedback from a transducer measuring the actuator displacement.

As discussed in section 2.1, the vehicle was designed to have neutral steering. This is useful from a handling point of view, but furthermore the proximity of the steer angle to the idealised Ackerman response was a necessity for the control of the cabin tilt angle. As a result, a reasonably accurate estimate of the lateral acceleration can be made using the vehicle speed and steer angle.

Inverted Pendulum Cabin Model

As mentioned previously, the moment required to lean the cabin into the corner is provided by the two single-ended actuators and can be represented as a torque about the tilt axis T_{act}. The torque is proportional to the difference between the actual tilt angle (θ) and demand (θ_d) tilt angle as shown in equation 2.19. The proportional gain is represented by the term G.

$$T_{act} = G(\theta_d - \theta) \tag{2.19}$$

The tilting cabin can be represented as an inverted pendulum as shown in figure 2.8 for which the equation of motion can be written as equation 2.20, where I_c is the cabin inertia.

$$I_c\ddot{\theta} = M_x - R_y h_{c\theta} cos(\theta) + R_z h_{c\theta} sin(\theta) - C\dot{\theta} \tag{2.20}$$

The term $C\dot{\theta}$ has been added to represent the damping element introduced as a result of hydraulic valve flow-pressure characteristics and through the friction in the actuators. Without this term, the system can be shown to be unstable under certain conditions [35].

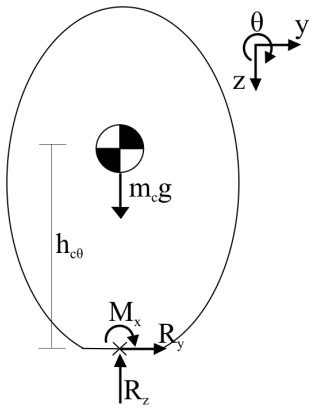

Figure 2.8: FBD of tilting cabin modelled as an inverted pendulum

Determining the Demand Angle

The method used to calculate the demand tilt angle is based on the approximation that the steer angle is equivalent to the Ackerman angle. The cornering radius R can therefore be estimated from the front steer angle δ_f and the wheelbase L as shown in equation 2.21.

$$\tan \delta_f = \frac{L}{R} \Longrightarrow R = \frac{L}{\tan \delta_f} \tag{2.21}$$

The lateral acceleration can be estimated from the vehicle forward velocity as shown equation 2.22.

$$a_y = \omega^2 R = \frac{V^2}{R} \tag{2.22}$$

The demand angle is that for which the lateral acceleration and gravitational components cancel each other out. Equation 2.1, 2.21 and 2.22 can be combined to estimate the necessary steady state θ_{ss} or demand θ_d tilt angle.

$$\theta_{ss} = \theta_d = tan^{-1}\left(\frac{a_y}{g}\right) = tan^{-1}\left(\frac{V^2 \tan \delta_f}{Lg}\right) \approx \frac{V^2 \delta_f}{Lg} \tag{2.23}$$

Equation 2.23 is valid for the inverted pendulum representation of the cabin shown in figure 2.8. However this does not take into account the non-tilting rear module, the height of the tilt-axis about the ground which results in a smaller absolute tilt angle (see section 2.2.2) and the tyre slip angles generated at higher lateral accelerations. Furthermore, the equation was linearised for use in the controller as shown by the approximation in equation 2.23.

Controller Implementation

The controller used in the CLEVER vehicle was a TERN TD40 programmable micro-controller based on a 40MHz 16-bit AMD186 processor. A signal conditioner was also used as an interface between the signal transducers and the controller in order to convert the signals from analog to digital and vice versa. Furthermore a 15Hz filter was implemented in order to reduce the noise in the signals. The schematic is shown in figure 2.9.

The closed loop control for the tilt angle demand is shown in figure 2.10. An additional 'overlean factor' was added to the calculated tilt angle to compensate for the reduction of the effective tilt angle due to the raised tilt axis (section 2.2.2). This value was determined through subjective test and was set to 1.2, i.e. the tilt angle demand was increased by 20% . Although, this resulted in additional cornering forces through camber, the additional rear steer meant that the vehicle handling was not greatly affected.

The control valve implemented on CLEVER used an overlapping spool to minimise leakage across the valve in the closed position. As a result, the valve demand signal had to be adjusted to eliminate the dead-band, which is equivalent to 15 % of the spool displacement. Finally, the valve opening was limited in order to restrict the speed at which the cabin tilts. This was necessary for passenger comfort and for safety reasons. The process for the calculation of the valve position demand is shown in figure 2.11.

It should be noted that as a result of using linear potentiometers to measure signals such as tilt and steer angle, there will be discrepancies between the integer value taken by the controller and the actual angular position. These errors were considered acceptable with regards to the resulting dynamics of the vehicle. Furthermore, it is worth noting

that due to a manufacturing error the actuator mounting positions were not located symmetrically about the tilt axis. As a result, the vehicle has a larger range when leaning to the left than when leaning to the right. These factors were taken into account in the control loop.

2.4 Concluding Remarks

The CLEVER prototype vehicle was developed around a specific control strategy that relied on the neutral handling characteristics of the vehicle. The linearised handling model and the initial assumptions made to develop the control method have resulted in a number of limitations in terms of its current handling and the scope for further development. It was shown that the required tilt axis inclination necessary for neutral handling did not match the implemented angle, resulting in an understeering characteristic. However, as a result of the raised tilt axis, the effective tilt angle of the cabin centre of gravity from the ground was 20 % less than the relative tilt angle between the cabin and the rear module. To compensate for this effect, an 'over-lean' factor was introduced in the control loop. As the linear handling model assumed that the tilt angle and camber angle were equivalent, the extra camber from the 'over lean' results in higher cornering forces and compensates to a certain degree for the increased tilt angle inclination. This brings the handling characteristic closer to the Ackerman condition. Furthermore, linearisations in the handling model as well as in the controller will affect the accuracy of the lateral acceleration estimate. This is discussed further in Chapter 6.

Although the electronic control system allows a certain scope for alterations, the capabilities of the controller could be improved though the use of a floating point processor. However, the kinematic set-up of the vehicle imposes restrictions on further improvement, as the levels of rear wheel steer are directly proportional to the tilt angle of the cabin. This should be taken into account in any control strategy.

Although experimentation has shown that the steady state performance of the vehicle is acceptable ([35], [11]), the direct tilt control approach means that there are limitations in terms of transient response if the handling of the vehicle is to remain safe. These limitations will be explored in detail through the use of a non-linear full vehicle model.

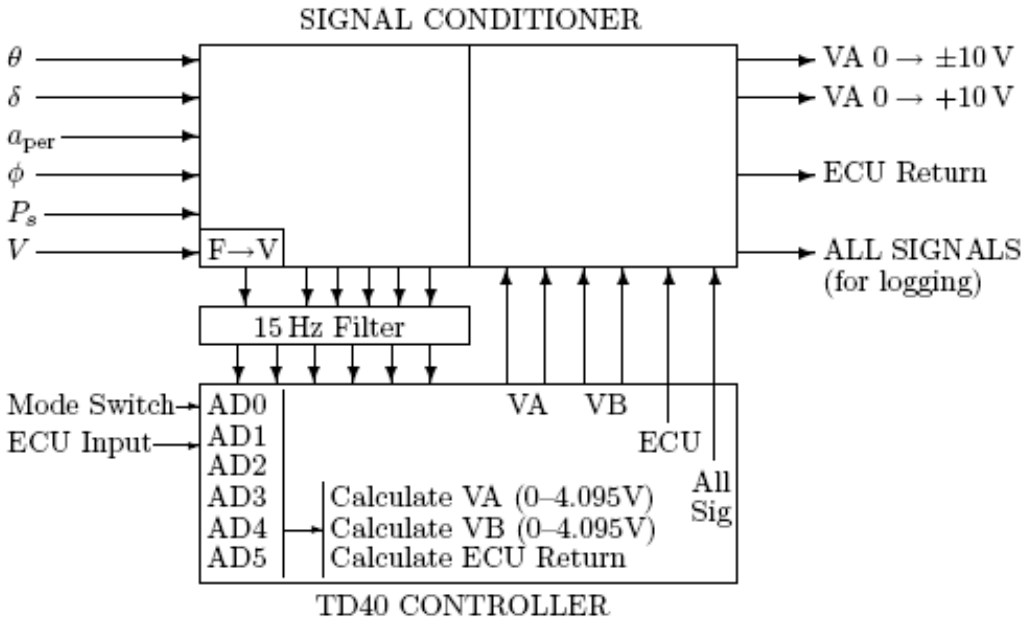

Figure 2.9: Schematic diagram of the signal conditioner and controller [35]

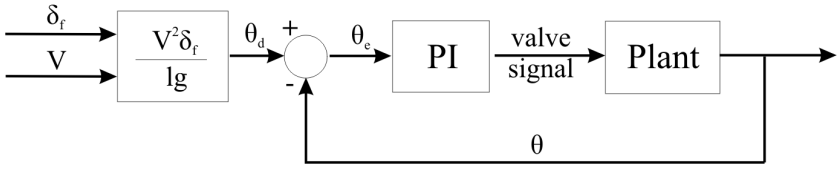

Figure 2.10: Block diagram of CLEVER control loop

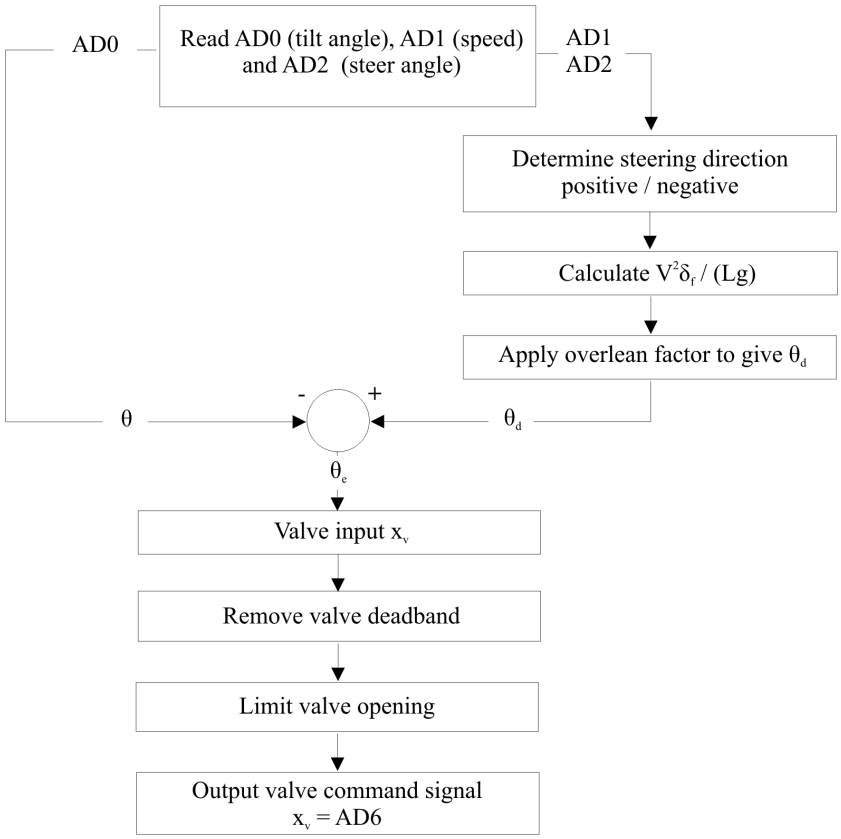

Figure 2.11: Flow chart for position demand calculation

Chapter 3

Vehicle and Systems Modelling

This chapter focuses on CLEVER's roll dynamics and ride characteristics. Preliminary estimates of mass locations and inertias were taken from CAD models of the vehicle and these were refined through measurements. The rear spring stiffness and damping coefficients were measured using a dedicated rig.

In order to create a better understanding of the mechanism that can lead to the roll-over of the vehicle, the roll dynamics of the vehicle can initially be described with a five degree-of-freedom system where the cabin is represented as an inverted pendulum mounted on top of the rear module. The principal degrees of freedom are the roll of the rear module and tilt angle of the cabin. The model also includes the vertical motion of the rear wheels as these affect the angular position of the rear module. The vertical motion of the wheels is also coupled to the vertical displacement of the rear module and cabin. The model assumes that the roll and bounce dynamics can be decoupled from the pitch mode.

The ride characteristics or in-plane dynamics are modelled using a series of single degree of freedom systems. It was possible to decouple the system due to the symmetry of the vehicle. The assumption that the bounce and pitch modes can be decoupled is verified using a two degree of freedom model.

Finally, the roll and in-plane dynamics were combined in a SimMechanics multi-body model. The development of the model was required to obtain a better understanding of the results obtained in the three post rig experiments (chapter 4), which were significantly different from those expected using the decoupled models.

3.1 Parameter Identification

Assuming the 5 DoF model captured the important dynamics, it was necessary to obtain accurate parameter values. The location of the centre of gravity of the front and rear modules and their respective masses had to be identified. The values used in previously studies ([11], [35]) stemmed from CAD models based on the fully trimmed vehicle. It was therefore attempted to refine these initial estimates through measurements based on the experimental vehicle available for testing purposes. Furthermore, additional measurements were taken with the driver as this represents a significant percentage of the overall cabin mass. Further tests were performed to verify the spring and damping coefficients of the suspension, and hydraulic valve coefficients were estimated from manufacturer data sheets. Although simplifications have been made through linearisation and other approximating techniques, the aim of the model is to investigate dominant effects in the vehicle handling and stability rather than predict exact values. The values taken were therefore deemed reasonable for the purpose of the model.

3.1.1 Determination of the Vehicle Mass and Centre of Gravity

Using load cells under each wheel, the vehicle mass without driver was measured as 329.5kg. The tests were repeated with the driver. The person and seating position were identical to those used in the dynamic tests. The lengths a and b can be calculated using the loads at the front W_f and rear wheels W_r according to equation 3.1. Where W_t is the total vehicle weight and $(a + b)$ is equivalent to the wheel base L. Table 3.1 shows the weight distributions with and without a driver as well as the corresponding horizontal distances of the front and rear contact patches to the vehicle CoG location, a and b respectively.

$$a = \frac{W_r(a+b)}{W_t} \qquad \text{and} \qquad b = \frac{W_f(a+b)}{W_t} \tag{3.1}$$

The height of the CoG of the vehicle was determined by lifting the front wheel and measuring the vertical reaction at the rear wheels. Using the load cells, the new longitudinal distances to the front and rear wheels, a_2 and b_2 respectively, can be calculated with equations 3.1. The height of the centre of gravity from the ground can be calculated using equation 3.2. The distance from the rear wheel bearing to the ground is denoted as r. This process is shown graphically in figure 3.1 (a).

	Without driver		With driver	
	kg	N	kg	N
Front tyre	97.6	957	136.8	1342
Rear left tyre	116.4	1142	138.0	1354
Rear right tyre	115.4	1132	137.0	1344
Total	329.4	3231	411.8	4040
a	1.69 m		1.60 m	
b	0.71 m		0.80 m	

Table 3.1: Vehicle weight distribution and longitudinal c.o.g location

$$h = \frac{b\cos\theta - b_2}{\sin\theta} + r \tag{3.2}$$

Using this method, the height h of the vehicle centre of gravity without a driver was located at 0.53m from the ground. Due to safety concerns, this test was not repeated with a driver inside the vehicle. Instead, the location of the driver CoG in the seated position was estimated at 0.73m from the ground. Adding this to the known vehicle CoG height results in a combined CoG height of the cabin and the driver of 0.57m.

The next step was to determine the mass and centre of gravity locations of the front and rear modules individually. This was achieved by tilting the cabin statically and measuring the resultant weight transfer using the load cells as shown in figure 3.1 (b). The individual wheel loads had to be measured at two different tilting angles while keeping the orientation of the rear module constant so that the weight shift can be associated entirely to the position of the cabin CoG. The calculations for this are shown in equations 3.3 to 3.5. The subscripts 1 and 2 refer to the first and second test

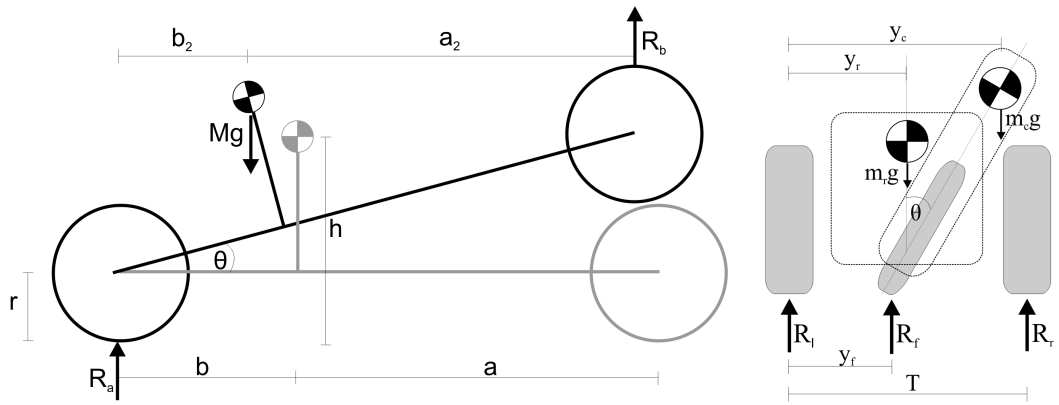

Figure 3.1: Determining the the height of the vehicle and cabin CoG

respectively.

$$m_r g y_r + m_c g y_{c1} = R_{f1} y_{f1} + R_{r1} T \tag{3.3}$$

$$m_r g y_r + m_c g y_{c2} = R_{f2} y_{f2} + R_{r2} T \tag{3.4}$$

$$y_c = h_c \sin\theta + y_f \tag{3.5}$$

In section 2.2.2 it was shown that the absolute or effective tilt angle θ_e is dependent on the longitudinal location of the CoG due to the raised tilt axis as shown in equation 2.13. The longitudinal location of the cabin CoG can be derived using the location of the rear module CoG, which can be estimated reasonably accurately from CAD data and the estimated masses of the cabin and rear module. The cabin CoG can then be found by equating moments about the overall vehicle CoG. Using this method, the cabin CoG is estimated to be located at 1.09m from the front tyre contact patch. This is close to the value from CAD estimates of 1.13m. The relationship between the cabin tilt angle and the distance from the cabin to the left tyre y_c is given in equation 3.5. It should be noted that the lateral position of the front tyre varies due to the kinematics resulting from the tilt axis inclination (section 2.2.1). Although the kinematic effects due to the tilt axis are not represented in the equations for simplicity, they were taken in account in the calculation process. With $m_r g y_r$ constant it is possible to combine equations 3.3, 3.4 and 3.5 to obtain an a value for $m_c h_c$. The estimated value of the cabin mass must then be used to obtain the cabin CoG height. These were estimated to be 176.5kg and 0.54m respectively. This in turn results in a rear module mass m_r of 162.0kg and rear module CoG height h_r of 0.54m. The final values are summarised in table 3.2.

3.1.2 Suspension

The suspension geometry and stiffness and damping properties are vital to the dynamic behaviour of the vehicle. The rear suspension in particular has the task of reacting the forces produced by the actuators and acting as a stable platform for the tilting system. Simultaneously it should provide satisfactory ride and handling performance. The

Symbol	Value		Description
m_v	329.4	[kg]	Total vehicle mass
m_d	82.5	[kg]	Driver mass
m_c	167.4	[kg]	Cabin mass
m_r	162.0	[kg]	Rear module mass
a_c	1.09	[m]	Dist. front cabin CoG to front tyre contact patch
b_c	1.31	[m]	Dist. front cabin CoG to rear tyre contact patch
h_c	0.52	[m]	Height of front cabin CoG
a_r	2.35	[m]	Dist. rear module CoG to front tyre contact patch
b_r	0.05	[m]	Dist. rear module CoG to rear tyre contact patch
h_r	0.54	[m]	Height of rear module CoG
a_d	1.24	[m]	Dist. driver CoG to front tyre contact patch
b_d	1.16	[m]	Dist. driver CoG to rear tyre contact patch
h_d	0.74	[m]	Height of driver CoG

Table 3.2: Weight distribution of individual vehicle components

suspension parameters required for the model were taken from vehicle specifications [11] and verified experimentally.

Suspension Geometry

The rear module of the vehicle uses a trailing arm suspension setup with an Öhlins spring and damper shock absorber. The geometry of the suspension was set up to give a near-linear relationship between wheel vertical movement and suspension compression by positioning the spring and damper units tangential to the arc of the trailing arm [11]. This is shown in figure 3.2 (b). The lever ratio in the design position is 1.38. The front suspension set-up is shown in figure 3.2 (a). The front wheel is attached to the chassis by two parallel swingarms and a single Öhlins spring and damper shock absorber. Figure 3.2 (a) also shows the hub centre steering mechanism. The lever ratio of the front spring and damper is 1.19 in the design position.

Parameter identification

The spring stiffnesses of the front and rear suspension units are 25N/mm and 21N/mm respectively when taking into account lever arms. The damping units are adjustable in compression and rebound. The rear dampers were set to a maximum to reduce the rear module roll in transient states. To evaluate the damping coefficients with this setting, a damper was tested separately on a test bench at several operating frequencies. The

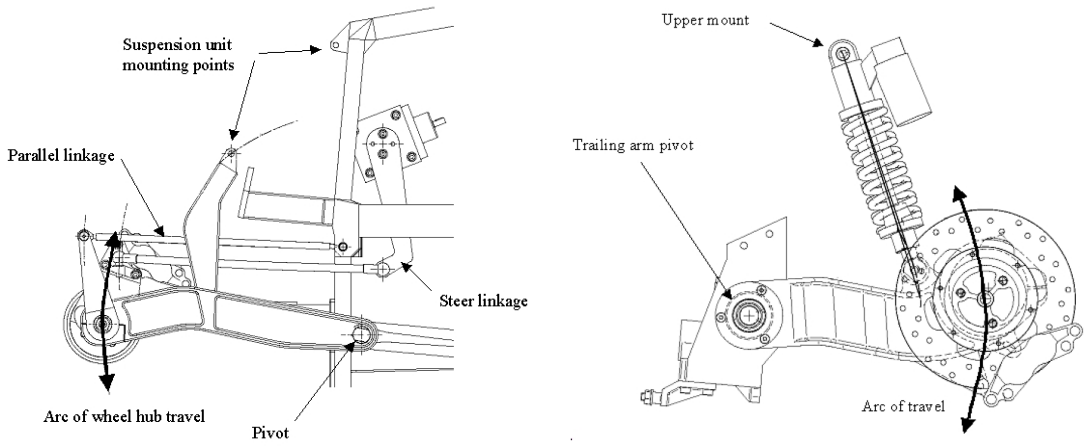

(a)Front (b)Rear

Figure 3.2: Front and rear suspension geometry

data was used to obtain a linear coefficient for the damping in compression and in rebound. The results are shown in figure 3.3.

The damping coefficients in compression and rebound were approximated as 2500 Ns/m and 4500Ns/m respectively. The damping coefficient of the front shock absorber was taken as 1400Ns/m [11].

The rear shock absorbers were set up with a preload of 410N. As a result, the ratio of compression and rebound travel in the design position was 60:40 mm. The effect of the pre-load and the bump stop on the suspension stiffness is shown in figure 3.4.

Roll Stiffness

The roll stiffness of the vehicle due to the rear suspension $K_{\phi s}$ can be calculated through equation 3.6, where K_s is the stiffness of the rear springs and has a value of 21N/mm when taking into account lever arms and T is the vehicle track of 0.84m.

$$K_{\phi s} = \frac{T^2 K_s}{2} \tag{3.6}$$

Using equation 3.6 with the above mentioned values results in a roll stiffness of 7400Nm/rad or 129Nm/deg. The same calculation can be performed to find the vehicle roll due to the tyres. With a tyre stiffness of 270kN/m and using the vehicle track $T = 0.84$m, the

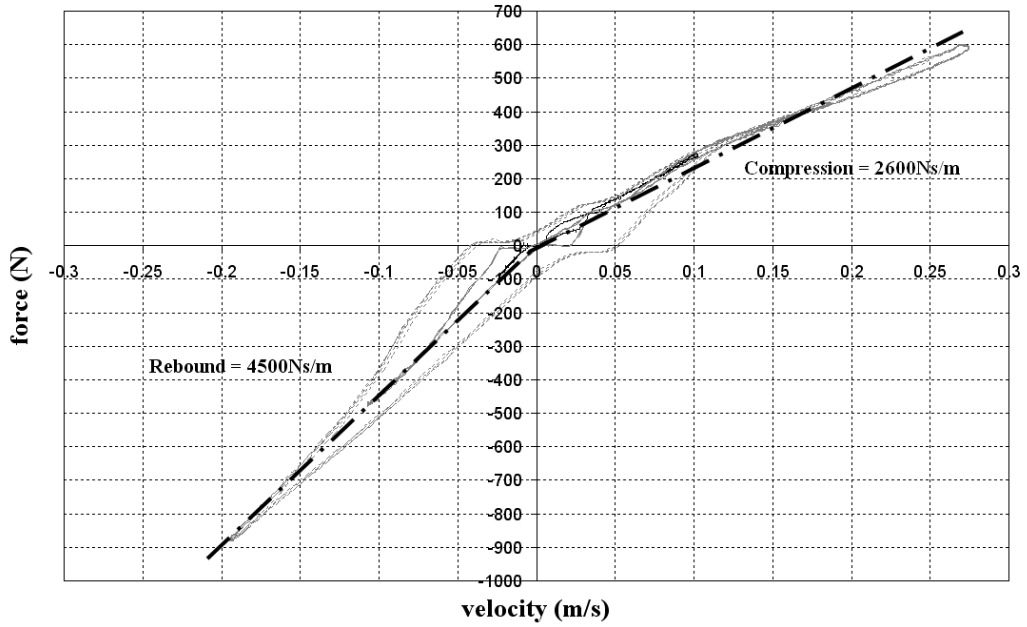

Figure 3.3: Results of rear damper tests and linear damping coefficient approximation

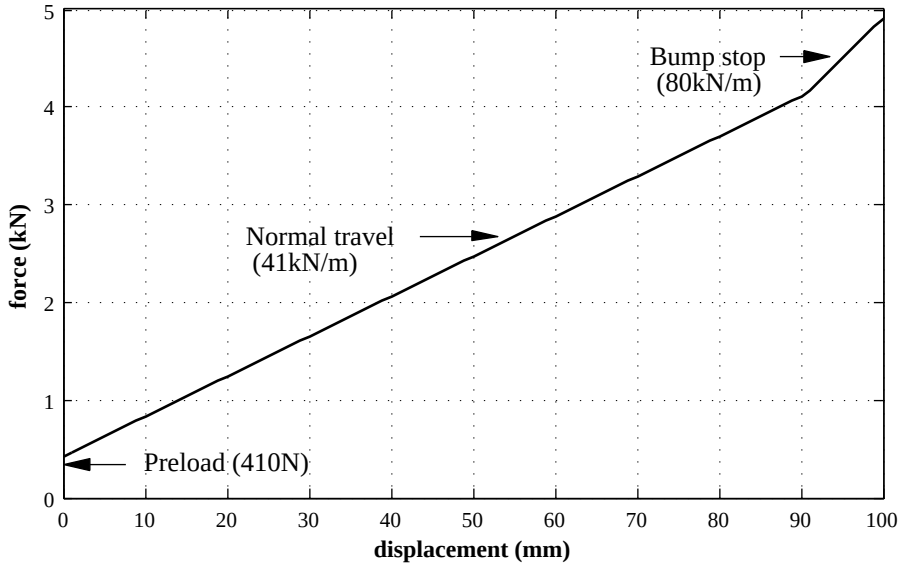

Figure 3.4: Effect of spring preload and bump stop stiffness for rear suspension

roll stiffness due to the tyres is 95.3kNm/rad or 1660Nm/deg.

It is necessary to keep the suspension roll to a minimum and to increase the effective lean angle to reduce the load transfer that can result in roll-over of the vehicle. For this reason a roll bar is used which increased the overall rear module roll stiffness K_ϕ to 307Nm/deg. Theoretically, the highest achievable roll stiffness is limited by the tyre stiffness.

The roll resonant frequency of the vehicle can be estimated using equation 3.7.

$$\omega_{n\phi} = \sqrt{\frac{K_\phi}{I_\phi}} \tag{3.7}$$

With an estimated roll inertia of $108kgm^2$ the natural frequency of the entire vehicle without the driver (with locked hydraulics) rolling on the suspension is estimated at 1.3Hz and rolling on just the tyres at 4.5Hz. With the addition of the roll bar the natural roll frequency of the vehicle on the suspension is increased to 2.4 Hz.

3.2 Front Cabin

The free body diagram of the forces acting on the cabin is shown in figure 3.5. The front cabin is supported vertically by the reaction forces F_{zf} at the front wheel and R_z at the tilt bearing. Similarly, the lateral forces are provided by the reactions F_{yf} and R_y. Finally, there is a moment M_x about the tilt bearing that is provided by the actuators.

For simplicity, the following equations refer to the values of the cabin without driver. The equations of motion of the cabin in the vertical (z) and lateral (y) directions are given by equations 3.8 and 3.9, where the lateral acceleration a_y is made up of the components $\ddot{y}$ and $V\dot{\psi}$ as shown in equation 3.10 and V represents the forward velocity of the vehicle. The rotation θ about the tilt axis is given in equation 3.11. Finally, the yaw motion (ψ) of the cabin is given in equation 3.12.

$$m_c\ddot{z} = m_c g - F_{zf} - R_z \tag{3.8}$$

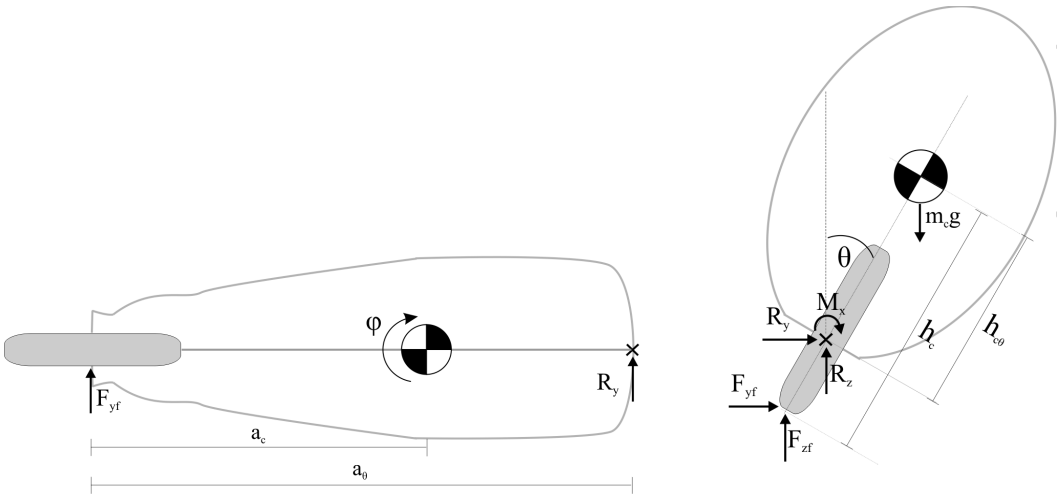

(a) Top View (b) Rear view

Figure 3.5: Free body diagram of the cabin

$$m_c a_y = F_{zf} + R_z \tag{3.9}$$

$$a_y = \ddot{y} + V\dot{\psi} \tag{3.10}$$

$$I_{xc}\ddot{\theta} = M_x + (F_{zf}h_c + R_z h_{c\theta})\sin\theta - (F_{yf}h_c + R_y h_{c\theta})\cos\theta \tag{3.11}$$

$$I_{zc}\ddot{\psi} = R_{y1}a_c - R_{y2}(a_\theta - a_c) \tag{3.12}$$

As the yaw acceleration remains small ($\ddot{\psi} \to 0$)[1], we can combine equations 3.9 and 3.12 to resolve for F_{yf} and R_y. Assuming that $\ddot{z} = 0$, the vertical reactions F_{zf} and R_z can be determined from the weight distributions shown in table 3.2.

In the model, the cabin alone has a single degree of freedom, namely the angulular motion θ about the tilt-axis described in equation 3.11. The motion in the z-y plane is determined by the motion of the rear module. It is also necessary to calculate the weight distribution of the front cabin across the rear axle R_{zr}, so that the reaction forces at the rear tyres are equal to the loads measured. The load across the rear

[1]This is verified in Chapter 5

	a_c	m_c&m_{cd}	h_c&h_{cd}	R_{zr}
Without driver	1.09m	167.4kg	0.52m	746N
With driver	1.14m	249.9kg	0.59m	1156N

Table 3.3: Cabin CoG location and resultant reaction at the rear axle

axle is dependent on the cabin mass and the longitudinal location of the cabin centre of gravity. Using the values in table 3.2 from section 3.1.1 it is possible to obtain the values shown in table 3.3 for the longitudinal distance of the cabin CoG from the front tyre contact patch a_c and resultant vertical reaction at the rear axle R_{zr} for the cabin with and without driver. The values for the mass of the cabin with and without driver are denoted as m_{cd} and m_c respectively. Equally, the overall centre of gravity height of the cabin will increase when the driver is seated in the cabin. The height of the cabin CoG from the ground with and without driver is denoted as h_{cd} and h_c respectively. It should be noted that depending on the seating position of the driver and possibly the presence of an additional passenger, these values can vary significantly. As experiments were conducted either without a driver or with a specific driver, the resultant mass distributions for these two cases is presented.

3.3 Rear Module

The rear module holds the engine and ancillaries as well as all the hydraulic components. It also acts as a base for the hydraulic actuators to react against in order to tilt the cabin to the required angle. The vertical and roll dynamics of the rear module are especially important as they affect the drivability and comfort of the vehicle as well as the tilting dynamics. It was decided to model the rear module as a four degree of freedom system. A representation of the system is shown in figure 3.6.

The suspension units are modelled as vertical spring and damper systems, where the values of the spring stiffness K_s and the damping C_s take into account the lever arm of the suspension. As previously mentioned, separate rebound and compression coefficients are used. The vertical stiffness and damping of the tyres are modelled with a linear spring and damper with coefficients $K_t = 269$ N/mm and $C_t = 1151$ Ns/mm [11]. Due to the trailing arm type suspension, the rear wheels will have the same roll angle ϕ as the rear module. The forces acting on the rear module can be summarised as vertical forces resulting from the spring and damper elements, a lateral wheel force, a vertical reaction R_z at the tilt bearing from the front cabin and the reaction from the hydraulic actuators M_x. For the 4DoF rear module model R_z is replaced with the

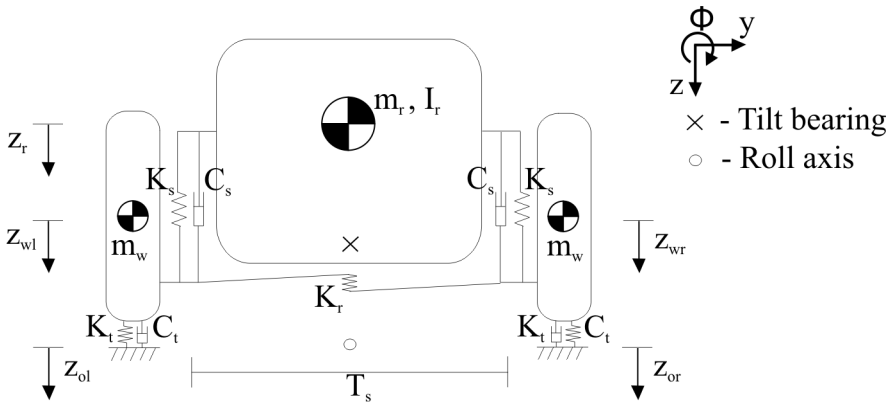

Figure 3.6: Four DoF representation of the rear module viewed from the rear

effective weight transfer of the front cabin onto the rear axle R_{zr}. As the rear module CoG is positioned closely to the rear axle, the weight transfer to the front axle can be ignored. The roll bar has been modelled as a linear spring, where the displacement is equal to the relative displacement between the two axles. The roll bar has an effective stiffness K_r of 25kN/m. The additional roll stiffness due to the roll bar is given in equation 3.13.

$$K_{\phi r} = K_r T_s^2 \tag{3.13}$$

The equations of motion for each element is shown in equations 3.14 to 3.17

$$\begin{aligned} m_w \ddot{z}_{wl} = m_w g + K_t(z_{ol} - z_{wl}) + K_s(z_r - z_{wl} + \phi\frac{T_s}{2}) + K_r(z_{wr} - z_{wl} - \phi T_s) \\ - C_t(\dot{z}_{ol} - \dot{z}_{wl}) + C_s(\dot{z}_r - \dot{z}_{wl} + \dot{\phi}\frac{T_s}{2}) \end{aligned} \tag{3.14}$$

$$\begin{aligned} m_w \ddot{z}_{wr} = m_w g + K_t(z_{or} - z_{wr}) + K_s(z_r - z_{wr} - \phi\frac{T_s}{2}) - K_r(z_{wr} - z_{wl} - \phi T_s) \\ - C_t(\dot{z}_{or} - \dot{z}_{wr}) + C_s(\dot{z}_r - \dot{z}_{wr} - \dot{\phi}\frac{T_s}{2}) \end{aligned} \tag{3.15}$$

$$m_r\ddot{z}_r = m_r g + K_s(z_{wl} - z_r + \phi\frac{T_s}{2}) + K_s(z_{wr} - z_r - \phi\frac{T_s}{2}) + C_s(\dot{z}_{wl} - \dot{z}_r + \dot{\phi}\frac{T_s}{2}) + C_s(\dot{z}_{wr} - \dot{z}_r - \dot{\phi}\frac{T_s}{2}) \quad (3.16)$$

$$I_r\ddot{\phi} = K_s(z_{wr} - z_r - \phi\frac{T_s}{2})\frac{T_s}{2} - K_s(z_r - z_{wl} + \phi\frac{T_s}{2})\frac{T_s}{2} + C_s(\dot{z}_{wr} - \dot{z}_r - \dot{\phi}\frac{T_s}{2})\frac{T_s}{2} - C_s(\dot{z}_r - \dot{z}_{wl} + \dot{\phi}\frac{T_s}{2})\frac{T_s}{2} - R_z(h_r - h_\theta)\phi - M_x \quad (3.17)$$

3.3.1 Swingarm Friction

It was established that there was a considerable amount of friction in the rear swingarms. For a good correlation between experimental and simulated results, a stiction model was included in the simulation.

A number of standard approaches to modelling friction were tried, however, a reliable numerical solution could not be found with these models. The solution was to model the stiction force F_{stic} as a stiff spring being activated when certain conditions are met. These conditions were taken as follow:

- the stiction force $|F_{stic}|$ is less than 100N
- the relative velocity between the sprung and unsprung mass $|\dot{z}_w - \dot{z}_r|$ is less than 0.01 m.s^{-1}.

It was necessary to use the condition $|\dot{z}_w - \dot{z}_r| < 0.01 m.s^{-1}$ rather than detect zero crossings as when the spring representing the friction is active there will be small oscillations about zero due to the lack of a damping term. When both the conditions are met, the spring holds the strut in place until the stiction is overcome. Once the stiff spring is active, the relative displacement between the wheel and the body is measured and multiplied by the spring stiffness K_{stic} to get the stiction force (up to a maximum of 100N):

$$F_{stic} = K_{stic}(\Delta x_w - \Delta x_b) \quad (3.18)$$

where:

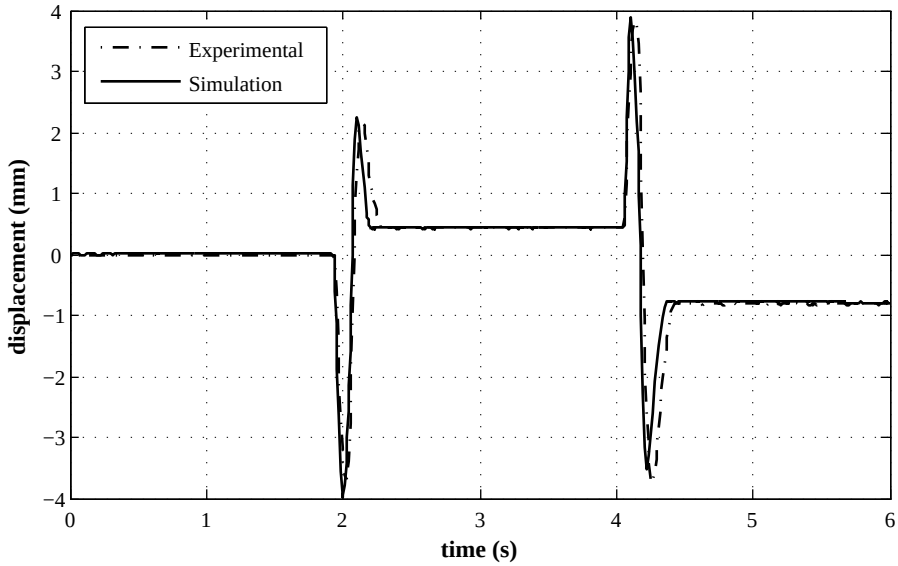

Figure 3.7: Frictional effects on suspension displacement resulting from a rapid ramp input

$$\Delta x_w = x_w - x_{w0} \tag{3.19}$$

$$\Delta x_b = x_b - x_{b0} \tag{3.20}$$

The subscript 0 denotes the value of the displacement when the stiction spring was activated.

The presence of friction can be clearly recognised in the experimental data shown in figure 3.7. The dashed line represents the measured suspension displacement as a result of a rapid ramp input (20mm in 0.1seconds) applied to the tyres at ground level. After the motion of the suspension has settled the vehicle is then dropped back to its initial position at the same rate. The solid line represents the simulated result to the same input. It can be seen that the friction model gives a good fit to the experimental data. It is also noted that the phase of the simulated data does not match the experimental data. This is likely to be a result of the linearization of the damping coefficients and the unmodelled coulomb friction.

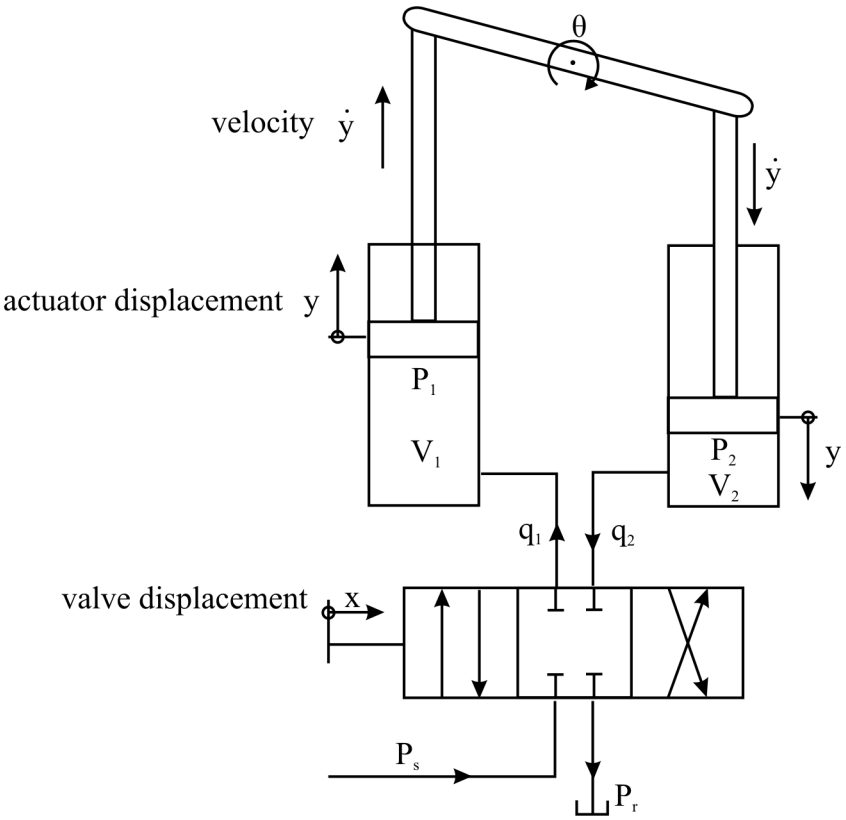

Figure 3.8: Valve operated system with two actuators

3.4 Hydraulic Control Valve and Actuators

The two actuators that tilt the cabin left and right can be modelled as shown in figure 3.8. The actuator motion is controlled by a proportional directional control valve. Using the zero lapped spool flow equations [37], the flow through the valve is defined as:

$$q_1 = Kx\sqrt{P_s - P_1} \tag{3.21}$$

$$q_2 = Kx\sqrt{P_2 - P_r} \tag{3.22}$$

The actuator flow is given by:

$$A\dot{y} = q_1 - q_{c1} \tag{3.23}$$

$$A\dot{y} = q_2 + q_{c2} \tag{3.24}$$

where q_c is the flow into the volume due to the effect of increases in pressure. Therefore:

$$q_{c1} = \frac{V_1}{\beta}\frac{dp_1}{dt} = \frac{V_1}{\beta}sP_1 \tag{3.25}$$

$$q_{c2} = \frac{V_2}{\beta}\frac{dp_2}{dt} = \frac{V_2}{\beta}sP_2 \tag{3.26}$$

where s is the Laplace operator and V_1 and V_2 are the volumes in each hydraulic cylinder and depends on the position of the actuator piston:

$$V_1 = V_0 + Ay \tag{3.27}$$

$$V_2 = V_0 - Ay \tag{3.28}$$

V_0 represents the volume of fluid with the actuator in the central position. Rearranging equations 3.23 and 3.24 and 3.25 and 3.26, we get an expression for the pressures P_1 and P_2 at either side of the piston.

$$P_1 = (q_1 - A\dot{y})\frac{\beta}{V_1}\frac{1}{s} \tag{3.29}$$

$$P_2 = (A\dot{y} - q_2)\frac{\beta}{V_2}\frac{1}{s} \tag{3.30}$$

Finally, the force exerted by the actuator is the difference in pressure in the two actuators $(P_1 - P_2)$ times the piston area A. This force is multiplied by the lever arm about which it acts and results in an equal and opposite torque acting on the rear module and the cabin. In the 5DOF model, the lever arm is taken as a constant equivalent to the average lever arm of 0.127m. In reality, the lever arm varies with tilt angle, as shown in figure 3.9 (a). This is incorporated in the multi-body model where the actuators are modelled as they are installed on the vehicle. A linear approximation of actuator displacement with tilt angle was taken. Figure 3.9 (b) shows the left actuator extension and the linear approximation used. This approximation was used to convert from the linear displacement measured on the left actuator to the required tilt angle feedback.

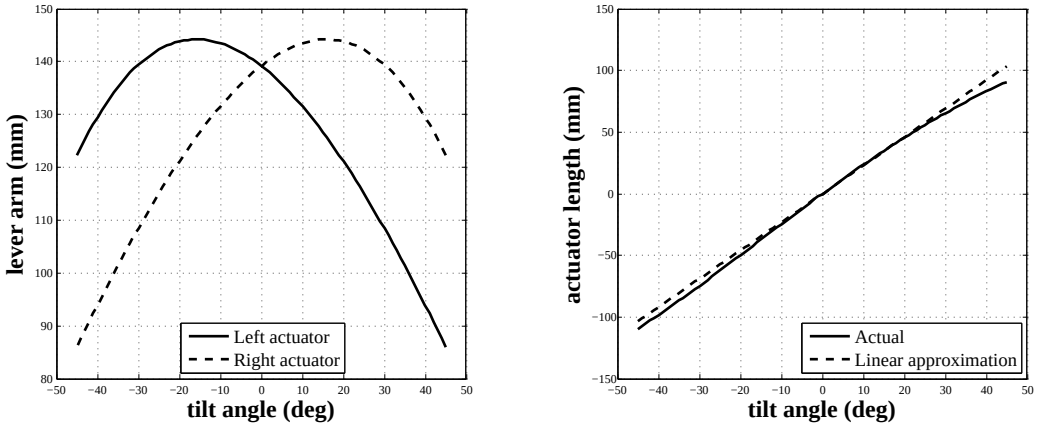

(a) (b)

Figure 3.9: Actuator lever arm (a) and actuator length (b) against tilt angle

The valve dead-band of 13.5% was added so that the valve drive signal from experimental results could be fed into the model for comparison. The frequency response characteristics of the spool were provided in the valve data sheet. The spool dynamic characteristics were therefore included in the form of a black box model, where a transfer function was fitted to the amplitude and phase characteristics using a least squares approach. The resultant transfer function relating valve input to output is of the 7^{th} order. The frequency response plot obtained from the data sheet represents the dynamics of the spool for a demand of $\pm$ 25% and is denoted by the solid line in figure 3.10. The dashed line represents the match from the black box model.

3.5 Control Unit

As explained in chapter 2, the original control method utilises speed and steer signals to calculate an estimation of the lateral acceleration and hence a required tilt angle. This is compared to the current tilt angle measured from a linear potentiometer mounted on one of the actuators to produce an error term which is proportional to the valve opening demand.

The control loop has a sample rate of 150Hz. The analogue channels are read sequentially at a rate of 2.17kHz which results in a delay of approximately 0.46ms between each successive channel. In order to minimise the delay between the main control channels (tilt, steer and speed), these were positioned in adjacent channels. The sampling frequency was regarded as sufficiently high as not to affect the dynamics of the vehicle

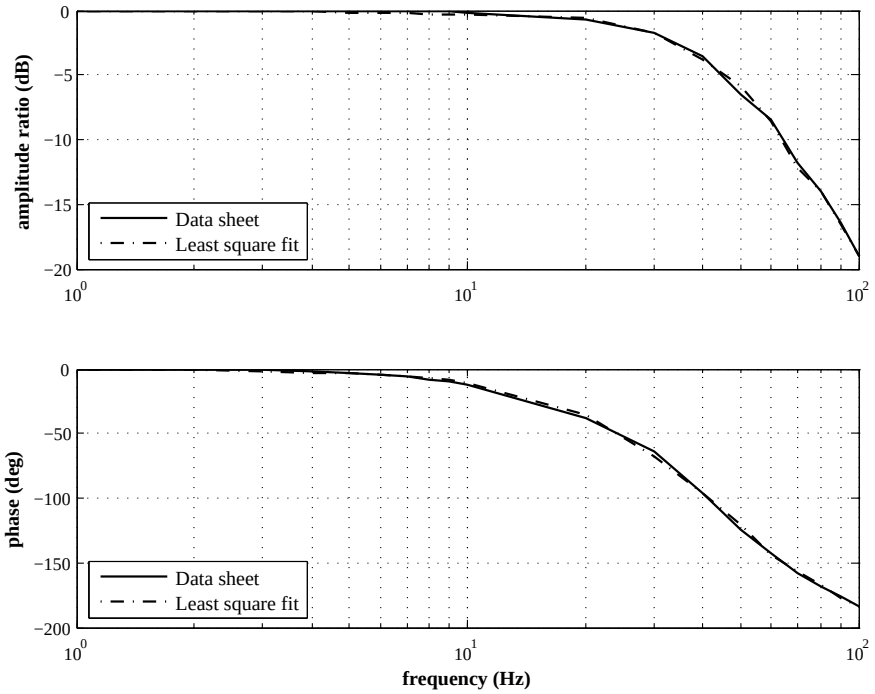

Figure 3.10: Black box model of the valve frequency response (± 25% stroke)

and was therefore not regarded in the model.

Before the analogue transducer signals are sampled by the AD converter, they are passed through a 15.9Hz analogue filter (signal conditioner) in order to attenuate the noise present in the signals. This is primarily due to the proximity of some of the sensors to the alternator and high tension circuit, which corrupts the signal with electromagnetic noise. Furthermore, the contacts on linear potentiometers can wear quite rapidly under certain driving conditions which leads to momentary voltage drops in the signal and hence erroneous readings. The filter characteristics can be modelled by the first order transfer function shown in equation 3.31, where τ has a value of 0.01s for a low-pass filter frequency of 15.9Hz. In this case, v_i and v_o represent the input and output voltage respectively.

$$\frac{v_i}{v_o} = \frac{1}{\tau s + 1} \tag{3.31}$$

Finally, a first order lag filter with a 2Hz cut-off frequency was implemented within the control loop. This was necessary to reduce the high frequency noise which affected the

spool displacement. The shuttling of the spool led to flow across the valve resulting in motion of the cabin.

3.6 In-Plane Dynamics

In straight line driving, the in-plane motion of a three wheeled tilting vehicle can be considered as the combination of vertical motion (bounce) and rotational motion (pitch and roll). These motions correspond to the principal vibration modes of the vehicle in the Z-Y and Z-X plane. As the vehicle can be considered to be symmetrical about the x-axis, it is possible to decouple the roll mode from the bounce and pitch modes. The pitch and bounce mode can only be decoupled if the following condition between front K_F and rear K_R stiffnesses and weight distribution is fulfilled:

$$K_F a - K_R b = 0 \tag{3.32}$$

The weight distribution depends significantly on the presence of a driver and passenger. As experimental tests have been performed both with and without driver, these two scenarios will be explored. The principal modes of vibration will be studied initially by uncoupling the individual modes. As the weight distribution varies depending on the presence of a driver and does not satisfy equation 3.32, a two degree of freedom model will be used to find the undamped natural frequency when the pitch and bounce modes are coupled. When studying the modes of vibration of the cabin and rear module system, it is possible to ignore the unsprung masses as the stiffness of the suspension is approximately 10 times smaller than the vertical stiffness of the tyres. The influence of the unsprung masses becomes important at higher frequencies.

3.6.1 One Degree of Freedom Models

Bounce, pitch and roll motion

We can consider the vehicle to be composed of one mass, sustained by three springs which represent the combined stiffness of the suspension K_i and the tyre K_{ti}. The subscript i denotes the location of the suspension and tyre (f, r and l for the front,

right and left respectively). The effective stiffness of the suspension is connected in series with the stiffness of the tyre, so that the equivalent elastic constants for each section is given by:

$$K_{i_0} = \frac{K_i K_{t_i}}{K_i + K_{t_i}} \tag{3.33}$$

By considering the three degrees of freedom as uncoupled, we can treat the vehicle as three individual single degree of freedom systems. The equilibrium equations of the vertical force and the moments about X and Y axes are given by:

$$m\ddot{z} + (K_{l_0} + K_{r_0} + K_{f_0})z = 0 \tag{3.34}$$

$$I_y\ddot{\mu} + ((K_{l_0} + K_{r_0})b^2 + K_{f_0}a^2)\mu = 0 \tag{3.35}$$

$$I_x\ddot{\psi} + (K_{l_0} + K_{r_0})\frac{T^2}{4}\psi = 0 \tag{3.36}$$

The natural frequencies $\omega_{n,z}$, $\omega_{n,\mu}$ and $\omega_{n,\psi}$ for the bounce, pitch and roll mode are therefore given by:

$$\omega_{n,z} = \frac{1}{2\pi}\sqrt{\frac{K_{l_0} + K_{r_0} + K_{f_0}}{m}} \tag{3.37}$$

$$\omega_{n,\mu} = \frac{1}{2\pi}\sqrt{\frac{(K_{l_0} + K_{r_0})b^2 + K_{f_0}a^2}{I_y}} \tag{3.38}$$

$$\omega_{n,\psi} = \frac{1}{2\pi}\sqrt{\frac{(K_{l_0} + K_{r_0})T}{4I_x}} \tag{3.39}$$

Using the values shown in table 3.6.1 results in the following resonant frequencies:

- Undamped bounce natural frequency w.o. driver $\omega_{n,z} = 2.07$Hz
- Undamped bounce natural frequency w. driver $\omega_{n,z} = 1.87$Hz
- Undamped pitch natural frequency w.o. driver $\omega_{n,\mu} = 3.02$Hz
- Undamped pitch natural frequency w. driver $\omega_{n,\mu} = 3.00$Hz
- Undamped roll natural frequency w.o. driver $\omega_{n,\psi} = 2.72$Hz
- Undamped roll natural frequency w. driver $\omega_{n,\psi} = 2.39$Hz

It can be seen that the driver does not have a significant influence on the principal harmonic frequencies.

Dist. CoG to Front w.o. driver	a_1	1.69m
Dist. CoG to Front w. driver	a_2	1.60m
Dist. CoG to Rear w.o. driver	b_1	0.71m
Dist. CoG to Rear w. driver	b_2	0.80m
System mass w.o. driver	m_v	329kg
System mass w. driver	m	412kg
Front unsprung mass	m_{uf}	30.0kg
Rear left unsprung mass	m_{ul}	27.0kg
Rear right unsprung mass	m_{ur}	27.0kg
System Roll Inertia w.o. driver	I_{x1}	27.8 kgm^2
System Roll Inertia w. driver	I_{x2}	36.0 kgm^2
System Pitch Inertia w.o. driver	I_{y1}	234 kgm^2
System Pitch Inertia w. driver	I_{y2}	252 kgm^2
Front effective stiffness	K_f	25.0 kN/m
Left effective stiffness	K_l	21.0 kN/m
Right effective stiffness	K_r	21.0 kN/m
Vertical tyre stiffness	K_t	250 kN/m
Front combined stiffness	K_{f_0}	22.7 kN/m
Left combined stiffness	K_{l_0}	19.4 kN/m
Right combined stiffness	K_{r_0}	19.4 kN/m
Wheelbase	L	2.4m
Wheeltrack	T	0.84m

Table 3.4: Vehicle system parameters for resonant frequency estimation

Wheel hop resonance

As a first approximation, it is possible to model the unsprung masses as one degree of freedom systems, where the mass is supported between the vertical stiffness of the tyre and the suspension stiffness. This is possible as the unsprung masses are significantly smaller than the sprung mass (15 - 18 times). The natural frequency of the unsprung masses are therefore given by:

$$\omega_{n,u_i} = \frac{1}{2\pi}\sqrt{\frac{K_i + K_{ti}}{m_{u_i}}} \tag{3.40}$$

Again, the subscript i denotes the position of the unsprung mass. This results in the following natural frequencies for the vertical motion of the unsprung masses:

- Rear left and right unsprung natural frequency $\omega_{n,u_l} = \omega_{n,u_r} = 15.24$ Hz
- Front unsprung natural frequency $\omega_{n,u_f} = 15.95$ Hz

3.6.2 Two Degree of Freedom Model

If the pitch and bounce motions remain coupled, the free oscillations, ignoring the damping effect, are described by the following equations:

$$\begin{bmatrix} m & 0 \\ 0 & I_y \end{bmatrix} \begin{Bmatrix} \ddot{z} \\ \ddot{\mu} \end{Bmatrix} + \begin{bmatrix} K_{f_0} + K_{l_0} + K_{r_0} & K_{f_0}a - (K_{l_0} + K_{r_0})b \\ K_{f_0}a - (K_{l_0} + K_{r_0})b & K_{f_0}a^2 - (K_{l_0} + K_{r_0})b^2 \end{bmatrix} \begin{Bmatrix} z \\ \mu \end{Bmatrix} = 0 \tag{3.41}$$

The frequency equation then becomes:

$$-mI_y\omega^4 + \left[(I_y + mb^2)(K_{l_0} + K_{r_0}) + (I_y + ma^2)K_{f_0}\right]\omega^2 - L^2(K_{l_0} + K_{r_0})K_{f_0} = 0 \tag{3.42}$$

The two roots of the equation are the undamped system's two natural frequencies, giving:

- Undamped bounce natural frequency w.o. driver $\omega_{n,z} = 2.03$Hz
- Undamped bounce natural frequency w. driver $\omega_{n,z} = 1.86$Hz
- Undamped pitch natural frequency w.o. driver $\omega_{n,\mu} = 3.05$Hz
- Undamped pitch natural frequency w. driver $\omega_{n,\mu} = 2.89$Hz

These are within 2 % of the values calculated when considering the systems to be uncoupled.

3.7 Multi-Body Model

As a result of the measurements obtained through the three-post rig experiments (chapter 4), it was decided to combine the roll and in-plane dynamics of the vehicle using a multi-body approach, implemented in SimMechanics. Using a 3 dimensional multi-body modelling approach as opposed to the simplified systems previously presented should allow for any coupling effects of the various modes to come through and simplify the addition of any effects which had not been modelled previously. The model was inititially verified against the simplified models before including any additional effects. Furthermore, where the 5DoF model uses linear approximations for the vehicle kinematics, these can be accurately represented using the multi body approach.

Figure 3.11 depicts an image of the model as represented in the SimMechanics model visualisation mode. The image is presented as an overlay on top of an image of CLEVER such that the individual bodies can be associated with each part of the vehicle. The individual bodies and their properties are listed in table 3.5. The values of mass and inertia were obtained through CAD models and through the experiments discussed in section 3.1.1. The inertia of the front cabin and the rear module had to be estimated as accurate assemblies were not available. The actuators and suspension struts were also modelled as two mass systems. Their mass and inertia values have not been listed as they are small compared to the other main bodies. Although it would have been possible to combine the model with CAD drawings to create a virtual reality visualisation, this would have come at high cost in terms of computational time and was not deemed to be within the scope of this project.

The hydraulic and control systems were represented using the same modelling approach as that discussed for the 5DoF model. The exception being that rather than a moment being applied at the tilt axis, the actuators are individually actuated using the calculated hydraulic force. The increased accuracy of the model comes with a high computational cost compared to the 5DoF model. The 5DoF model was therefore still deemed a useful tool to investigate the principal dynamics of the vehicle and the effects of major parameter changes. The multi-body model on the other hand was useful to investigate more subtle effects, and create a better understanding of the results obtained in the three post rig experiments. The top level of the multi-body model is shown in figure A.1 in the appendix.

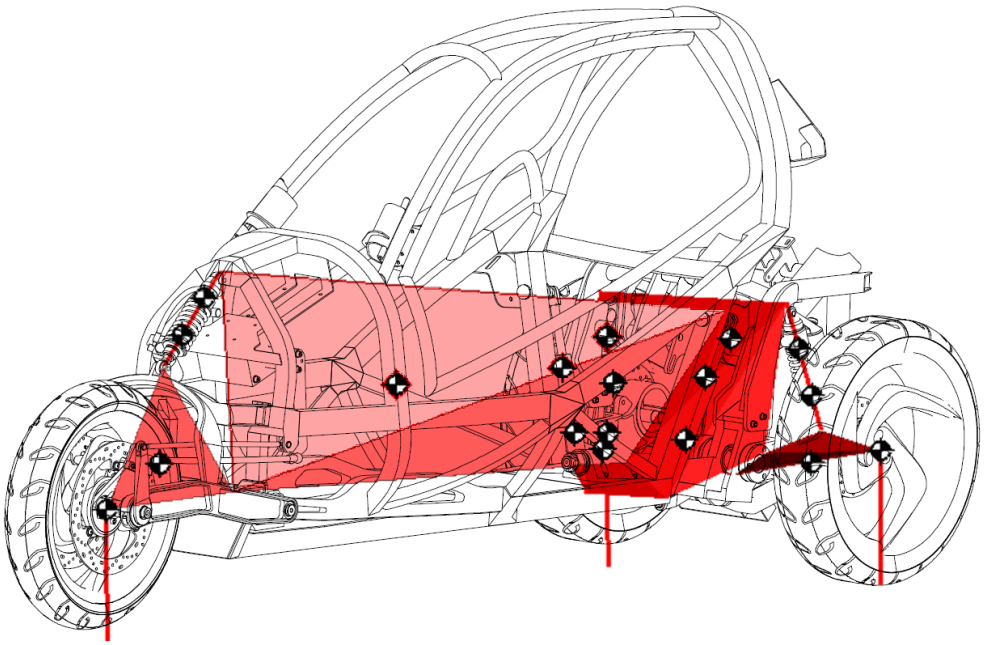

Figure 3.11: Vehicle multi-body model visualisation

Body	**Mass** $[kg]$	**Inertia** $[I_{xx} \quad I_{yy} \quad I_{zz}]$ $[kgm^2]$
Cabin	137	[14.5 200 170]
Rear Module	118	[13.3 13.3 13.3]
Driver	83	[8.2 7.3 1.4]
Front Swingarm	18	[0.43 0.60 0.77]
Rear Swingarms	15	[0.048 0.1 0.37]
Front Wheel	12	[0.27 0.54 0.27]
Rear Wheel	12	[0.27 0.54 0.27]

Table 3.5: Weight and inertia of main model components

3.8 Concluding Remarks

This chapter detailed the modelling approach of the vehicle as a five degree-of-freedom system where the cabin was modelled as an inverted pendulum mounted on the rear module. The 5DoF model is a simplified representation of the vehicle and is useful to investigate the basic dynamics of the vehicle. It is simple to make changes to specific parameters and investigate their individual effects. The model was then expanded to a full multi-body model of the vehicle to achieve a better fit to the results obtained in the three post rig experiments carried out to investigate the roll and bounce dynamics of the vehicle. The results of these tests were used to obtain a better understanding of the vehicle dynamics and refine the model parameters as well as validate the vehicle model.

Chapter 4

Three Post Rig Experiments and Validation of the Vertical and Roll Dynamics Model

The dynamics and ride characteristics of the CLEVER vehicle were investigated on a three post rig. The rig was set up such that each wheel was resting on a platform connected to a vertical hydraulic actuator and these were used to give various inputs to the vehicle. The study focuses on the bounce and roll dynamics of the vehicle, as these modes are likely to be affected by the additional tilt actuator forces as the vehicle is cornering. Furthermore, it was anticipated to use the data to validate the vehicle model described in chapter 3.

The experiments revealed that the frequency response of the vehicle was very non-linear and that a number of previously unknown characteristics inherent to the tilting vehicle design played an important role in the dynamics of the vehicle. Finally, the measured frequency response was compared with the simulated frequency response. Due to the high non-linearity and complexity of the measured frequency response an accurate fit was not obtained. However, the principal trends of the frequency response were reflected in the simulated data, and are considered sufficient for model validation purposes.

Further stationary tests were performed to investigate the relative roll motion of the cabin and the rear module and the effect of the hydraulic actuation on the system

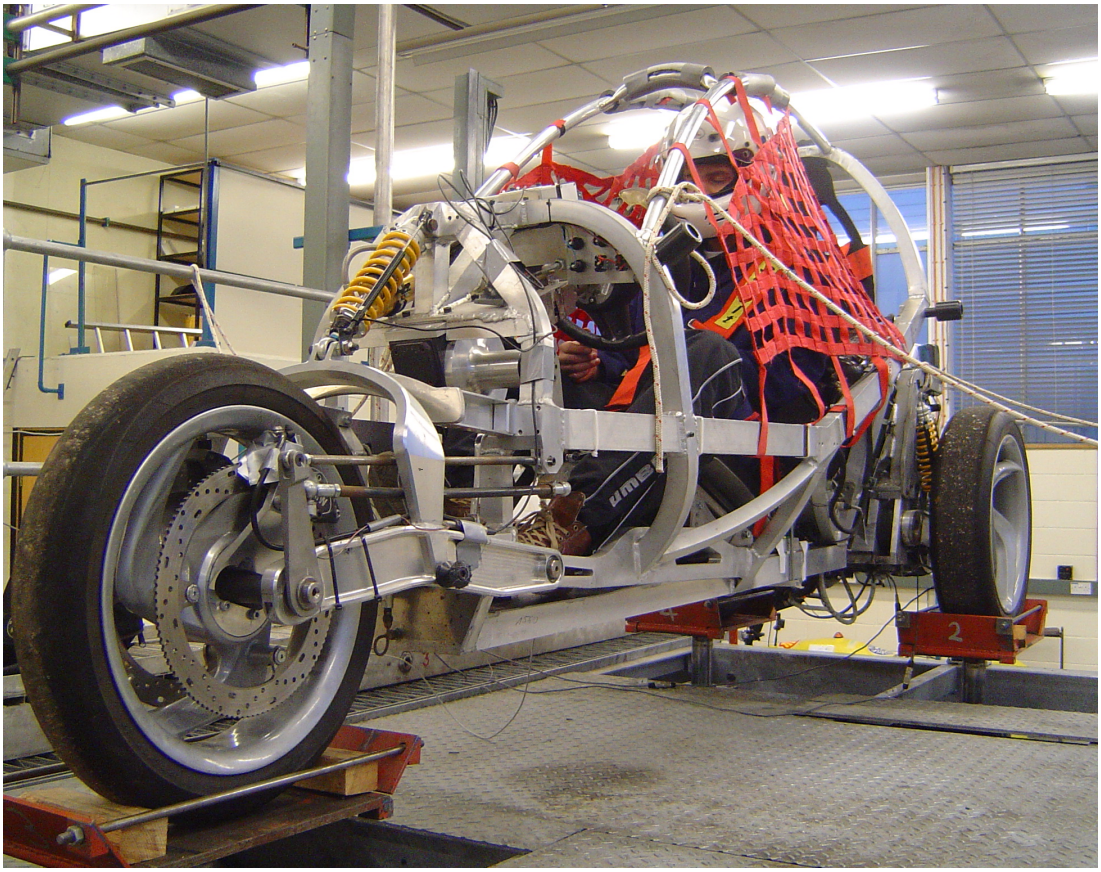

Figure 4.1: CLEVER vehicle on 3 post rig

dynamics. Virtual steer and speed signals were fed to the controller and the valve drive signal and relative tilt angle was measured. A good fit was obtained between measured and simulated signals.

4.1 Experimental Setup and Procedure

As shown in figures 4.1 and 4.2, each vehicle wheel was placed on a hydraulically actuated platform. The main parameter of interest in these experiments was the rear suspension displacement as it is key to the stability of the vehicle. The displacement of each of the three suspension units on the vehicle was measured using linear potentiometers mounted in line with the shock absorber. The vertical acceleration at the seat mounting point was also measured in order to obtain an idea of the accelerations perceived by the driver. After initial testing revealed a number of unexpected vibration modes, the vehicle was fitted with further sensors to measure the relative motion

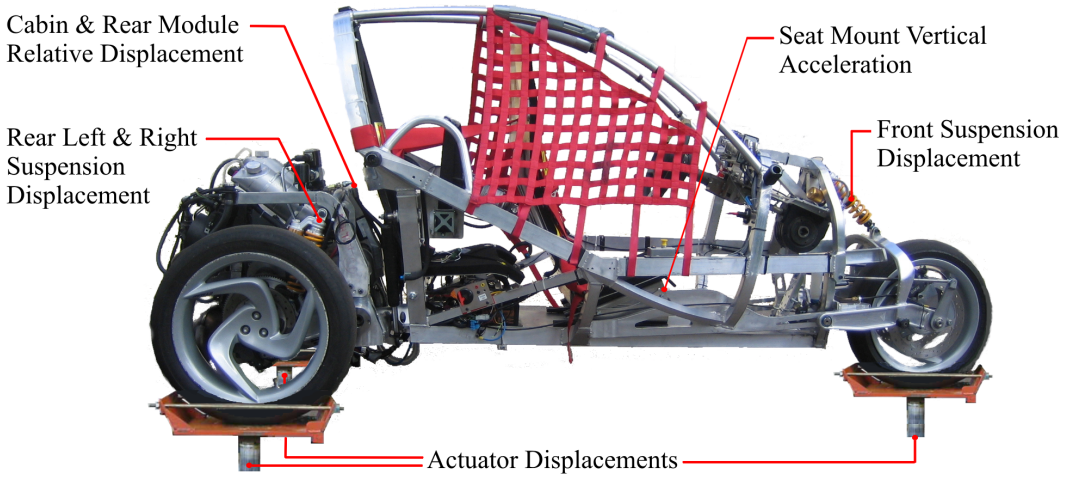

Figure 4.2: Sensors for three post rig experiments

between the cabin and the rear module. Linear potentiometers, set up to measure the relative pitch motion and roll motion of the cabin and the rear module, were mounted in the location indicated in figure 4.2. A detailed picture of the sensors can be seen in figure A.2 in the appendix. Figure 4.2 summarises all of the measured parameters and sensor locations.

The results were expected to reveal the primary natural frequencies of the vehicle in bounce and in roll, i.e. the body bounce and wheel hop mode and their equivalent modes in roll. Initially, the vehicle was excited at individual frequencies in order to give the system time to settle, however due to the complexity of the frequency response, the excitation was changed to a frequency sweep from 0.1Hz to 30Hz in 128 seconds. The amplitude was made frequency dependent such that the lowest frequencies were applied at the highest amplitudes. This approach was taken as it is similar to the amplitude frequency ratios encountered on open roads where low frequencies usually result from long wavelength undulations in the road and high frequency excitations usually result from short wavelength, low amplitude, surface irregularities in the road. The amplitude (in metres) at each frequency is given by equation 4.1.

$$A = \frac{5 \cdot 10^{-3}}{2\pi\omega} \tag{4.1}$$

The tests were repeated three times to check for repeatability and again at half amplitude to check the linearity of the system.

4.2 Results

4.2.1 Bounce Frequency Response

Firstly, the vehicle characteristics in bounce were investigated. It was anticipated that this would result in a good fit with simulated data as the frequency response would be dominated by the vehicle mass, spring and tyre stiffnesses which were all measured parameters. However, results revealed that there was considerable non-linearity in the system and that other effects played a significant part in the dynamics of the vehicle.

Estimates of the principal resonant frequencies using one and two degree of freedom models (section 3.6) resulted in an anticipated resonant frequency of the body bounce mode of 2.0 Hz. This mode will be coupled with some pitching motion, although the analysis in section 3.6 has shown that this will be minimal. The front and rear left and right wheel hop modes were estimated at 16.0Hz and 15.3Hz respectively.

Figure 4.3 shows a frequency response plot of the average suspension displacement of the rear shock absorbers over the input displacement of the road actuators. It should be noted that measurements at each end of the frequency range lack accuracy. At the lower end of the frequency spectrum (from 1- 4Hz) this was found to be due to the friction in the system (see section 4.2.3). This resulted in the shock absorbers locking until the force on them was sufficiently high to overcome the friction. The amplitude recorded at these lower frequencies is therefore simply a reflection of the amplitude of the noise in the potentiometers over the input displacement, and does not reflect the actual suspension displacement. Furthermore, the system might not have had sufficient settling time due to the frequency sweep at lower frequencies. At the opposite end of the frequency spectrum (around 30Hz) both the actuator and suspension displacements become so small that noise levels start to dominate, resulting in a noisy and inaccurate frequency response.

Looking at the frequency response plot, the variation in the measurements can be seen to be significant. Firstly, there is a considerable difference between the two amplitudes, showing that the system behaves in a non-linear way. Furthermore, there is variation in the measurements for the same input amplitudes. It is believed this effect is primarily as a result of the friction in the rear trailing arms. It can be seen that the suspension displacement is very small in the lower frequency range (around 2Hz) and then gradually rises and reaches a peak at around 6Hz after which there is a gradual decrease. The

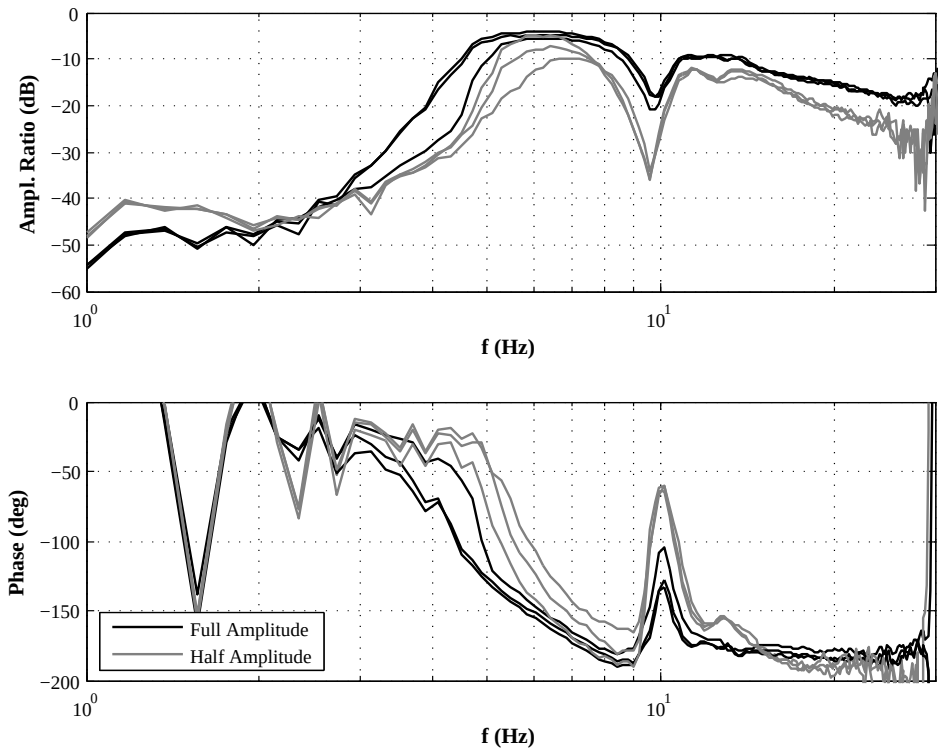

Figure 4.3: Average rear suspension displacement to bounce road input

frequency response around 10Hz is dominated by an additional effect which causes a sharp change in the amplitude ratio and phase. Upon inspection it was found that this anti-node coincided with the natural frequency of the tilt bearing, i.e. most of the energy was absorbed by the flexing of the joint about the y-axis. This was verified by placing a linear potentiometer between the rear module and the tilt cabin to measure their relative displacement as shown in appendix A.2. The resulting frequency response is shown in figure 4.4. As expected the frequency response displays a peak located around 10Hz.

As a result of the friction dominating the suspension displacement at low frequencies and the effect of the tilt joint at higher frequencies, it is difficult to discern the resonant frequencies resulting from body bounce and wheel hop modes. This makes it hard to confirm the previously estimated values. However, it is shown in section 4.3.1 that this frequency response can be obtained in simulation when taking the previously mentioned effects into account.

When looking at the difference in the rear suspension displacement it can be seen that there is some excitation of the vehicle roll modes as a result of vehicle a-symmetry

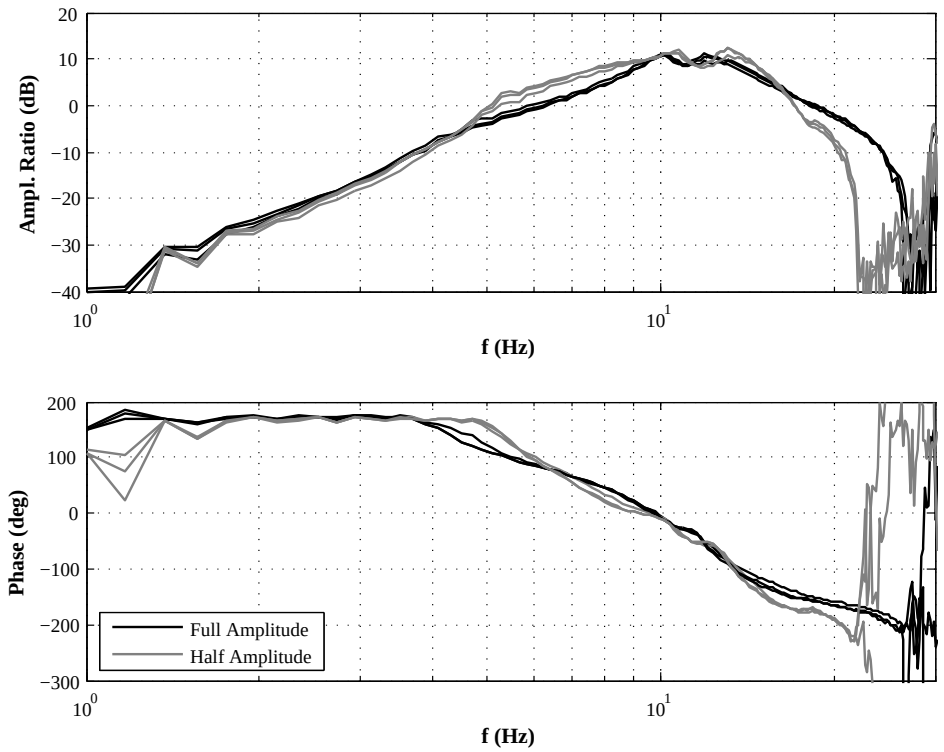

Figure 4.4: Frequency response of tilt joint to bounce road input

(figure shown in appendix A.2), although these effects remain fairly small and the vehicle is therefore modelled as symmetrical.

If we look at the frequency response of the front suspension shown in figure 4.5 we can see a similar shape to that obtained for the rear suspension displacement. The effect of the friction in the front swing arm on the frequency response can be seen quite clearly up to a frequency 3.5Hz, after which there is a sudden break in the frequency response where the suspension starts moving. The response shown is merely the amplitude of the noise over the input at the actuator. The locked state of the suspension at the lower frequencies can be seen clearly in the time domain plot shown in figure 4.6.

Although it is important that the main effects shown in the frequency response are understood, the dynamics displayed relate very much to the experimental nature of the vehicle. It will be assumed that if the vehicle were designed for manufacture and had not suffered a number of crashes, the friction in the trailing arms would be significantly less and the tilt joint would be reinforced. As the vehicle's dynamic response is likely to be significantly different if this was a production vehicle, it is not considered essential to get a very accurate fit for the data. Without these unwanted effects, the vehicle

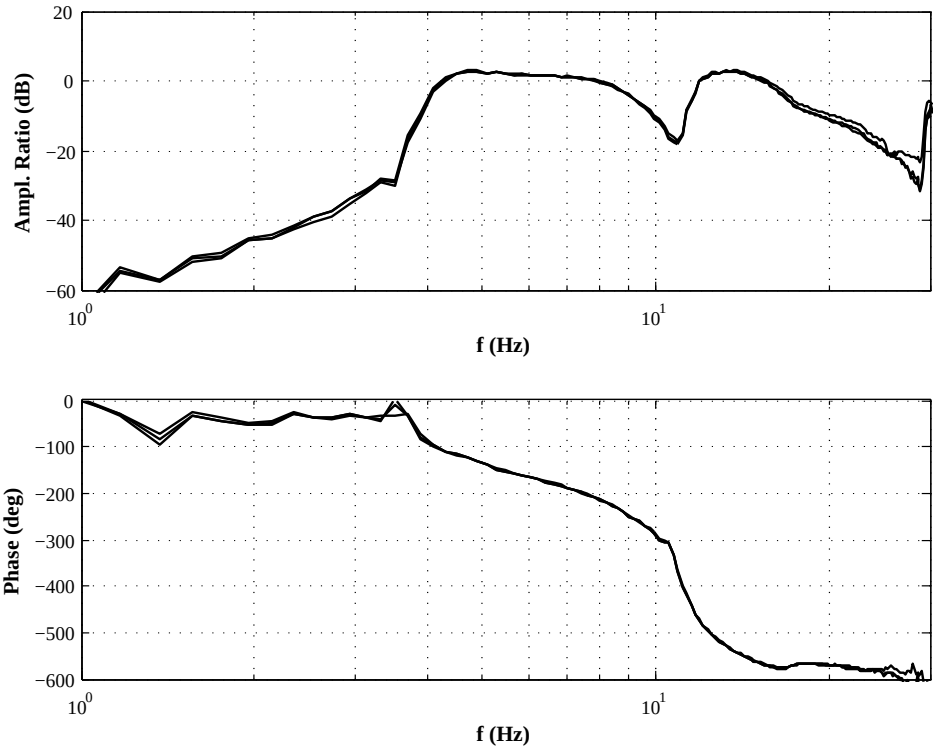

Figure 4.5: Frequency response of front suspension to bounce road input

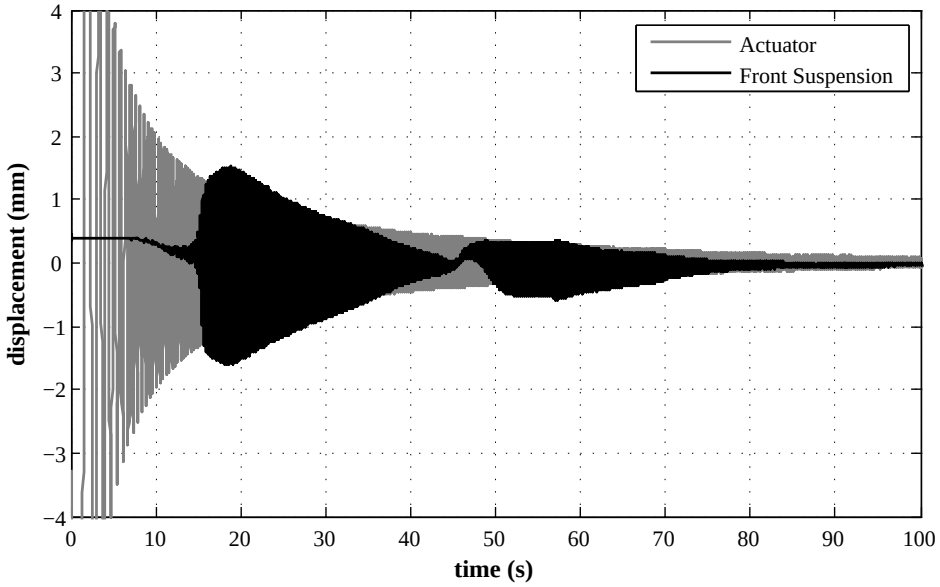

Figure 4.6: Time domain response of front suspension

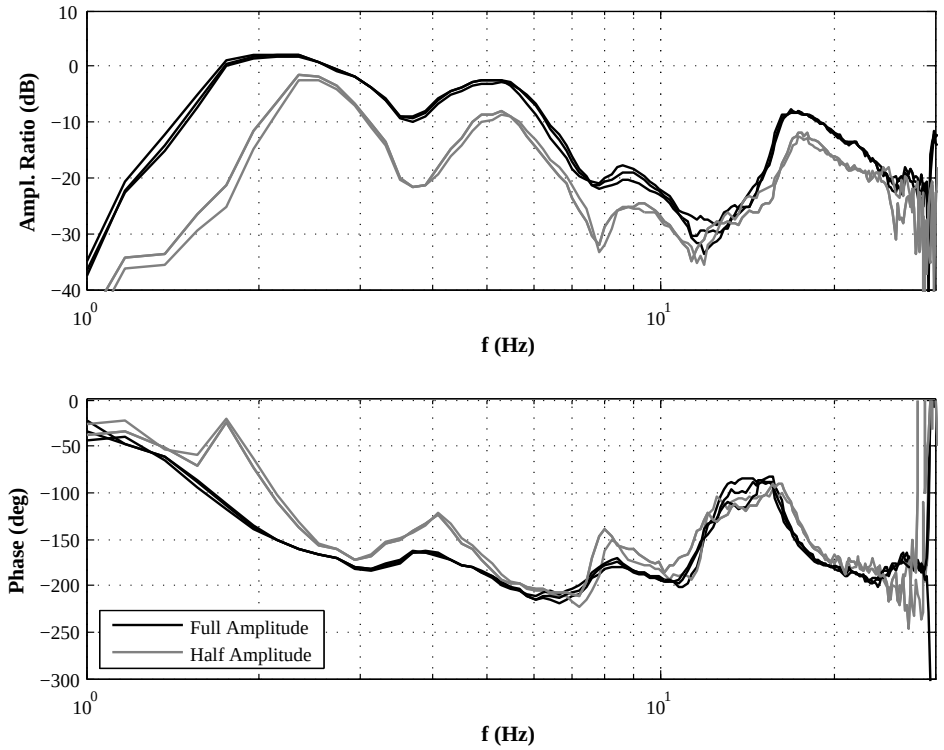

Figure 4.7: Frequency response of suspension in roll

frequency response is likely to look much more like the idealised SimMechanics vehicle model response presented in section 4.3.

4.2.2 Roll Frequency Response

The roll dynamics of the vehicle are especially important as in addition to possible excitations from road inputs, the reactions from the actuator forces can result in additional roll moments. Similarly to the previous results, the frequency response of the vehicle in roll was complex. By taking the difference in the suspension displacement, the roll modes of the vehicle can be observed. Figure 4.7 shows the difference in suspension displacements for a roll excitation. It should be pointed out that there are differences between the left and right suspension displacement which again shows that the vehicle is not perfectly symmetrical. Figure 4.7 also displays the non-linear behaviour. The individual displacement for the left and right suspension displacement as well as average suspension displacement, can be seen in appendix A.2.

It is observed that, unlike the bounce frequency response, the lower end of the frequency

A	$8.04 \cdot 10^{-4}$	m^2
β	18000	bar
β_e	4500	bar
V	$1.21 \cdot 10^{-4}$	m^3

Table 4.1: Parameters for the estimation of the hydraulic stiffness

spectrum appears to be fairly well represented. In other words the friction in the trailing arms does not appear to have a significant effect on the roll response. As a result, the roll natural frequency can be seen at 2.4 Hz which is in line with the estimate made in chapter 3. The reduced effect of the friction could be due to the weight shift across the axle far outweighing the friction in the trailing arms.

Again, it was seen that at certain frequencies the cabin and the rear module moved out of phase, which is why a second linear potentiometer was positioned to measure the relative displacement of the cabin and the rear module about the x-axis. The results are shown in figure 4.8. Unlike in the bounce frequency response, there is no obvious connection between the frequency response of the relative displacement of the modules and that of the suspension motion. The only observation that can be made is that the peak response of the tilt joint at 17Hz coincides with the peak in suspension displacement. The origin of the modes was initially investigated visually using slow motion video footage of the frequency response. The footage revealed that the lateral tyre stiffnesses and rotational stiffness about vertical axis of the tyre play a significant part. It could also be seen that there was a significant amount of flexibility in the vehicle frame. The video footage could also be used as a visual check for the simulated frequency response results.

As the results reveal that the relative motion between the two modules play an important role in the frequency response, it was necessary to model the actuator in the locked position. An estimate of the actuator stiffness was made according to equation 4.2 [37]. The variable A represents the actuator area, V the volume in the actuator and pipes up to the valve and β_e the effective bulk modulus. The effective bulk modulus for a system with flexible hose can be approximated as 25% of the oil bulk modulus β [37]. The values used are shown in table 4.1

$$K_{act} = \frac{2A^2\beta_e}{V} \tag{4.2}$$

Using these values results in an estimated hydraulic actuator stiffness of 4810kN/m.

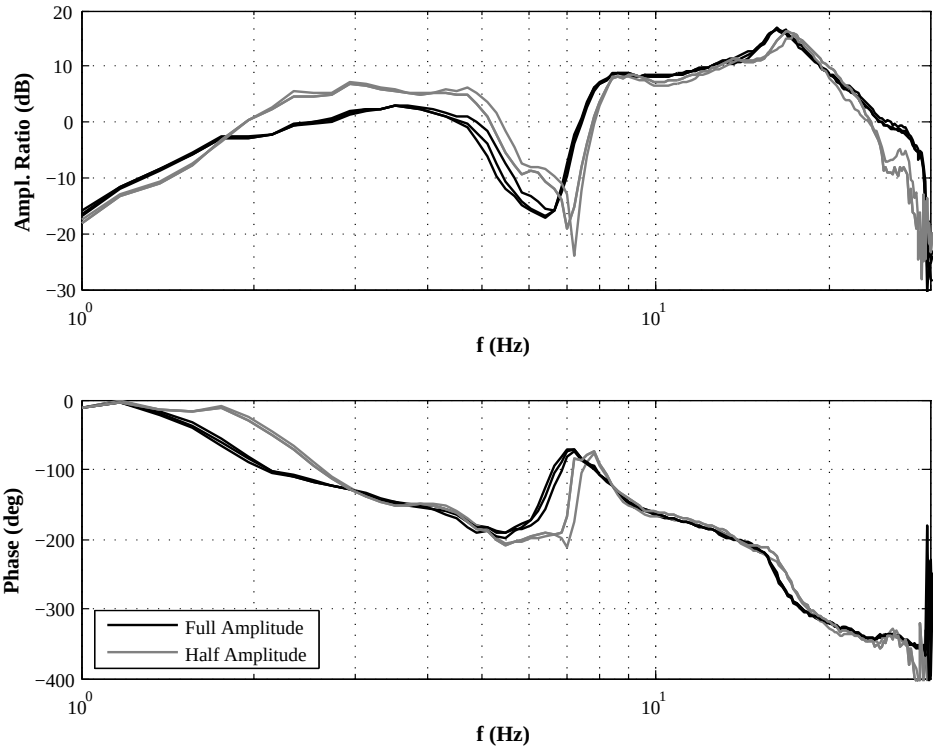

Figure 4.8: Frequency response of tilt joint in roll

However, the results suggest that the stiffness is in fact a lot lower in practice. In simulation, a better data fit was obtained with a stiffness of 1050kN/m. This could be due to the hose flexibility being more important than initially assumed or air being trapped in the system and thus increasing compressibility. Alternatively the reduced stiffness could be a result of the stiffness of the actuator mounting points rather than the actuators themselves.

The frequency response of the vehicle roll has been shown to be quite complex. Through video footage it was observed that lateral and rotational tyre stiffnesses as well as chassis flexibility play an important part in the response. Estimates of the tyre stiffnesses and hydraulic stiffness will be used to validate the model and create a better understanding of the observed frequency response. However, factors such as the flexibility of the frame will not be taken into account as this can again be attributed to the experimental nature of the vehicle. Identifying all the necessary parameters would be highly time consuming without serving any further purpose in this research. Clearly some of the modes will therefore not appear in simulation. By including the lateral and torsional tyre stiffnesses, the key features of the response should come through in simulation and give a better understanding of the measured data (see section 4.3).

4.2.3 Step Response

As a step input is physically impossible in practice, a rapid ramp input was applied. The wheel actuators were displaced by 20mm in 0.1 seconds, held for 2 seconds and then ramped back down. This process was repeated several times to get an impression of the repeatability and an idea of the levels of friction in the system. The resulting displacement of the rear suspension unit is shown in figure 4.9.

The presence of friction is clearly reflected in the results as the strut does not settle back to its position of origin. It was observed that high levels of friction were present in the trailing arms. These showed stick-slip like behaviour, although the friction is likely to be a combination of stiction and coulomb friction as shown in figure 4.10. This would have the effect of locking the swing arms at low frequencies, where insufficient force is applied to overcome the stiction. The effect of the stiction on the frequency response is shown in section 4.3.1. Once the stiction force is overcome, the system is subjected to coulomb friction. This would have the effect of decreasing the amplitude of the suspension displacement as a constant force would oppose the motion of the shock absorber. Unfortunately the effect could not be investigated in simulation as a reliable numerical solution could not be found for a model with coulomb friction.

As previously mentioned, the high levels of friction are likely to be linked with the experimental nature of the vehicle. It is therefore not considered necessary to get a detailed simulation of these effects, as a production vehicle would not display such high friction levels. The purpose of the friction model is to investigate the effects of friction and to confirm that the differences in the simulated and measured frequency response can indeed be attributed to frictional effects.

4.3 Model Validation

One of the main motivations for the three post rig experiments was to use the data to validate the vehicle model. The five degrees of freedom of the Simulink model discussed in chapter 3 were insufficient to model the complex vehicle dynamics revealed as a result of the three post rig experiment. The vehicle model was therefore expanded to a multi-body model using SimMechanics. Using this approach meant that the pitch dynamics of the vehicle could be included. For validation, the measured wheel actuator displacement was used as the input signal for the simulation. In this fashion any attenuation of the

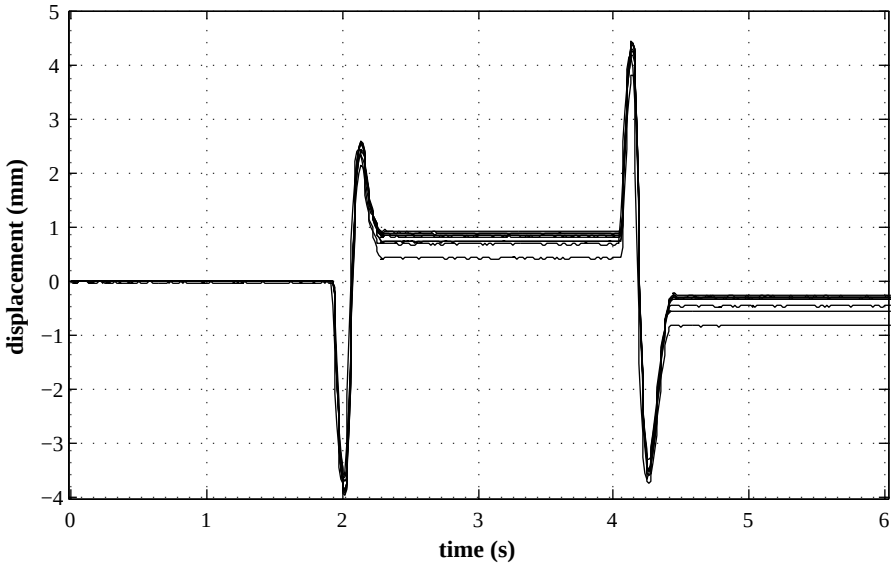

Figure 4.9: Suspension displacement for a series of step inputs

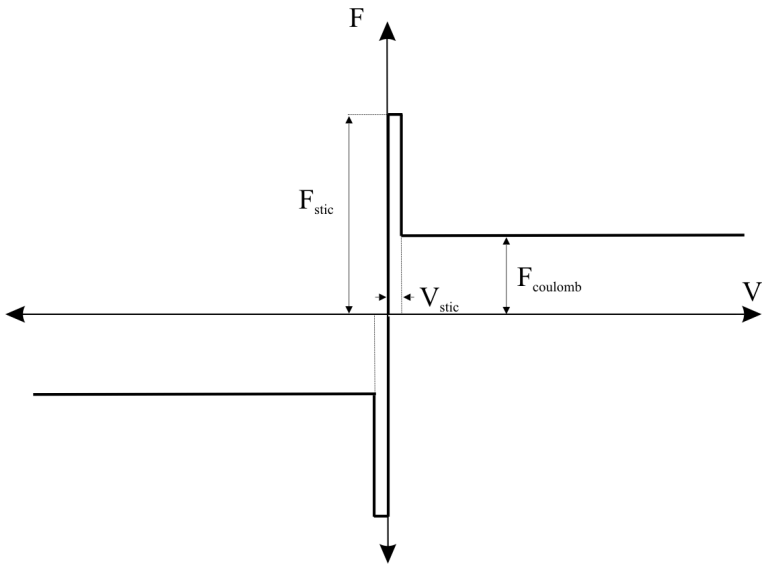

Figure 4.10: Friction model for rear swingarms

displacement demand signal due to the actuator dynamics is accounted for. The results of the validation process are shown in figures 4.11 to 4.14 for a constant actuator input amplitude, rather than the decreasing amplitude shown previously. This was chosen as the frictional effects can be more clearly recognised as the amplitude remains (approximately) constant up to the point where the stiction is overcome. Furthermore, by using a constant amplitude sweep, the amplitude at higher frequencies is sufficiently large to get an accurate response up to 30Hz.

As shown previously, the system behaves in a non-linear way and has a fair amount of variability. It is therefore unnecessary to strive for a perfect fit in simulation. The objective of the comparison with the multi-body model is to create an understanding of the principal effects that are displayed in the frequency response and to validate the parameters chosen for the model.

4.3.1 Frequency Response in Bounce

As was discussed previously, a number of unexpected effects came to light as a result of the frequency sweep. One of these effects was that of the tilt-joint flexibility causing the relative pitch motion of the cabin and rear module about the tilt bearing. To model this effect, an additional degree of freedom was added in the model by using a rotational joint with a stiffness of 1500Nm/deg and damping coefficient 2.5Nms/deg located between the two modules. Adding this extra degree of freedom results in the relative cabin and rear module displacement frequency response shown in figure 4.11. The amplitude ratio relates to the longitudinal displacement measured (along the x-axis) as measured 0.5m from the tilt bearing (see figure A.2 in appendix A.2). Figure 4.11 shows that adding the additional DoF and estimated stiffness gives a good fit with the measure frequency response. Furthermore, the dynamics of the joint are reflected in the suspension displacement at the anti-node at 10Hz, as shown in figure 4.12.

The dynamics at the lower end of the frequency range are thought to be dominated by frictional effects in the trailing arms. The stiction model presented in section 3.3.1 was implemented to confirm that stiction could prevent suspension motion at the lower frequencies. As can be seen in figure 4.12 adding the stiction does indeed restrict the suspension motion at the lower frequencies without much effect on the higher frequencies. By adding the extra degree of freedom at the tilt joint and the stiction in the swingarms, the shape of the measured frequency response can be fairly well replicated. However, there remains a significant difference in the amplitude ratio and

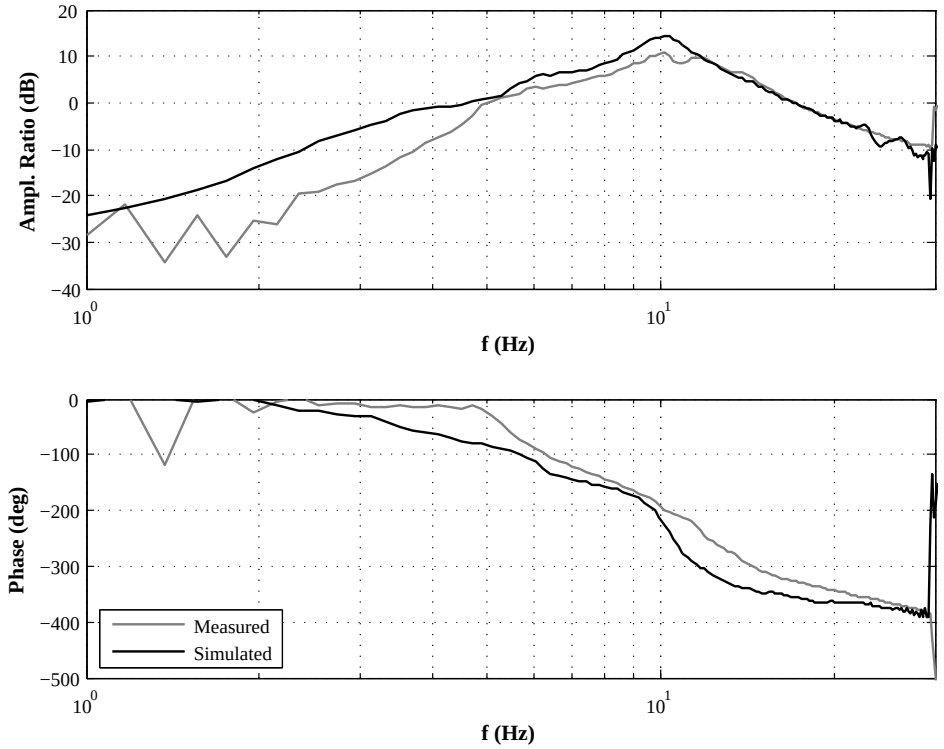

Figure 4.11: Relative cabin and rear module displacement in bounce

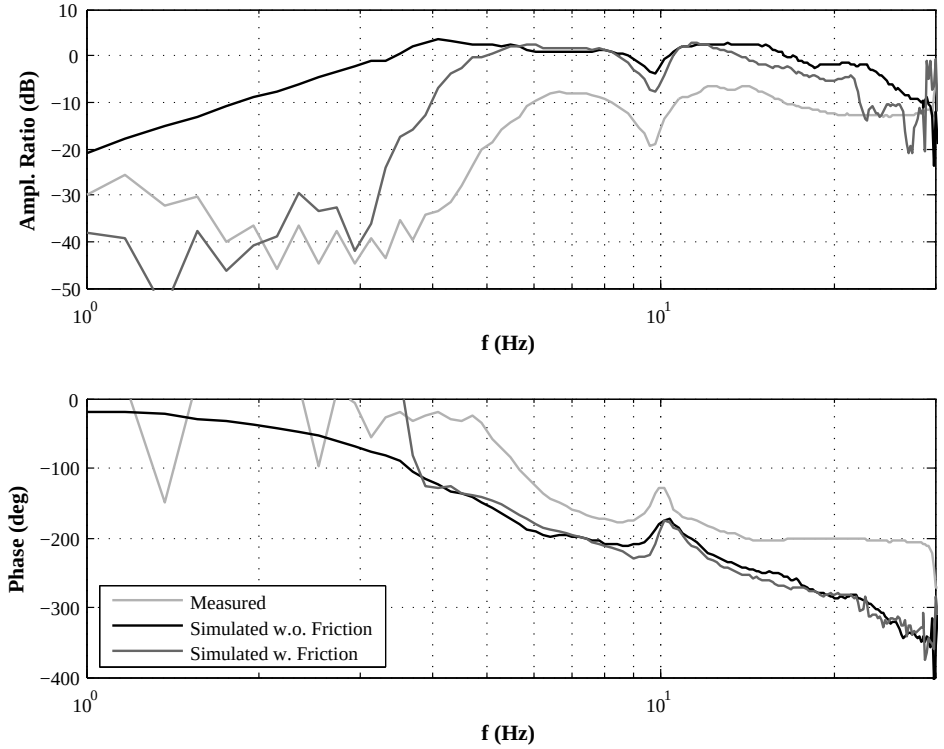

Figure 4.12: Average rear suspension displacement in bounce

phase. The amplitude ratio is 10dB lower than the measured amplitude ratio across the spectrum and the phase lags by approximately 45 °. It is believed that this large difference in measured and simulated data could be due to additional coulomb friction in the system. The coulomb friction would add a constant force opposing the motion of the suspension and therefore reduce the amplitude ratio across the spectrum. To verify this, an element of coulomb friction was added to the friction model. Unfortunately, it was not possible run the SimMechanics model successfully with this additional effect. As the modelling of this effect was not integral to this study, this was not pursued further.

4.3.2 Frequency Response in Roll

As seen from the frequency response plots previously shown, the dynamics of the vehicle in roll are quite complex. Although it is unlikely to recreate a perfect fit for the data, it is important that the main modes are understood, as when the vehicle is driving the roll modes will be further excited by the actuators tilting the cabin.

To obtain a reasonable fit it is clear that a higher order model is required. Whereas in bounce, modelling the vertical dynamics of the system was sufficient, the roll mode excites rotational and lateral dynamics as well as vertical dynamics. As the vehicle rolls, there is a lateral force component at each wheel that stops the wheel from sliding. Similarly, there will be rotational component at the wheels. It was therefore necessary to estimate the lateral and rotational stiffnesses of the tyres. The vertical tyre stiffness was taken as a reference point and the values were adjusted to match the measured frequency response. Further parameters that were not measured had to be adjusted (within reason) for the frequency response to match. As frictional effects did not appear to play as important a roll as in the bounce mode, the effects of stiction are not included in the roll results.

It can be seen that the simulation gives a good fit with the measured data for both the difference in suspension displacement shown in figure 4.13 and the relative motion of the rear module and cabin about the tilt bearing shown in figure 4.14. Using the simulation, the frequency response of the individual bodies could be looked at in detail and checked visually with the recorded video footage to create a better understanding of the results. Using this approach, it could be concluded that the peak in the response at 3Hz corresponds to the entire vehicle body rolling on the rear suspension. This corresponds with the estimates made in chapter 3. The second peak at 5Hz occurs as a

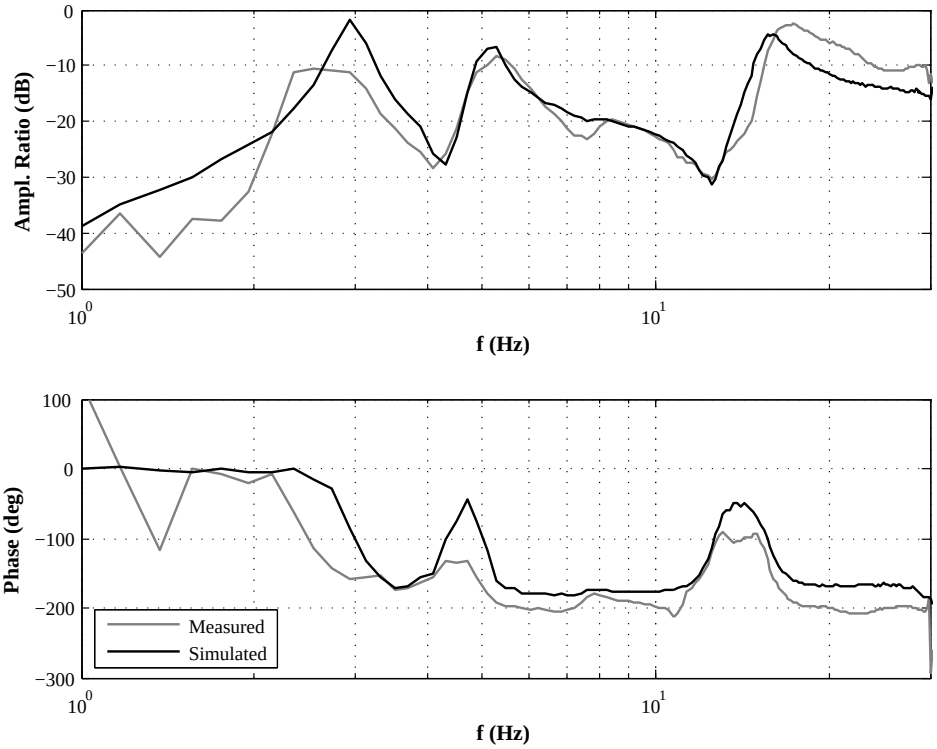

Figure 4.13: Difference in rear suspension displacement in roll

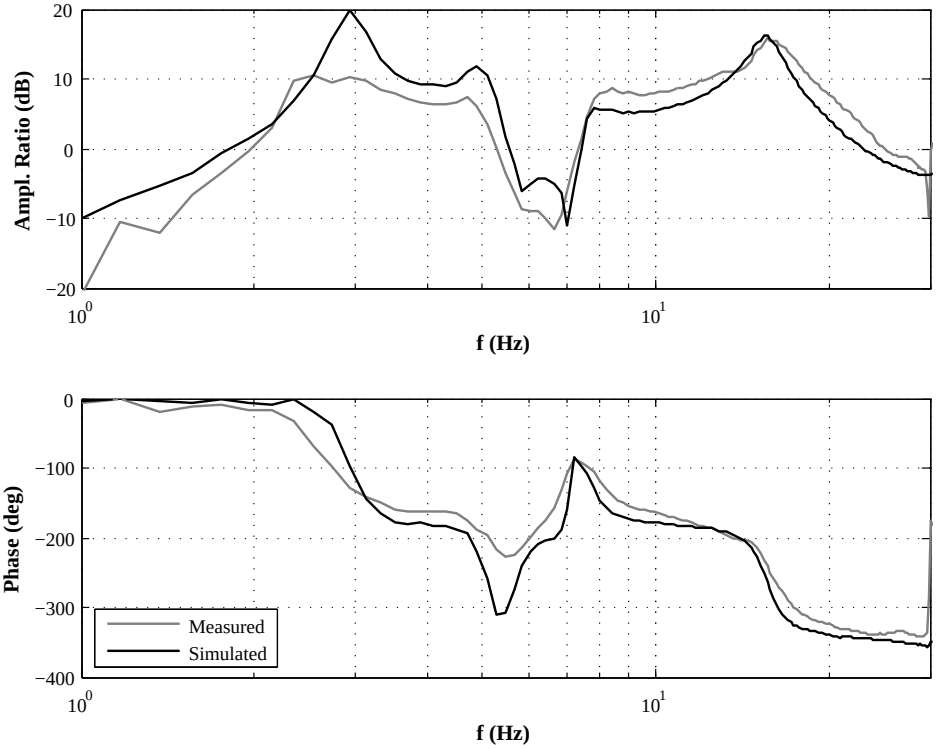

Figure 4.14: Relative front and rear module displacement in roll

result of the body rolling on the tyres with the cabin moving out of phase. This results in the peak in amplitude and drop in phase seen in the relative cabin displacement at 5Hz. Finally the peak at 16.5Hz corresponds to the wheel hop frequency that was estimated in 4.2.1

The final values of the stiffness and damping parameters used in the simulation are shown in table A.1 in appendix A.2.

4.4 Cabin and Rear Module Relative Roll Motion

The relative roll motion between the cabin and the rear module is dependent on the hydraulic system response. In order to test the system response, virtual speed and steer signals were generated and the resultant valve drive signal and relative tilt angle were recorded. The system input was a sinusoidal frequency sweep from 0-8 Hz with a steering-wheel angle amplitude of $\pm$ 45°at a speed of 16.7km/h. Figures 4.15 and 4.16 show the recorded valve drive signal and resultant tilt angle and their simulated counterparts up to 3Hz, as this encompasses the frequency range that could practically be applied by the driver.

The valve signal represents the percentage opening, where 1 is fully open. Overall, there is a good match between the measured and the simulated results. Some deviation from the measured data can be seen at the lower frequencies, especially in the tilt angle response. It can be seen that there is some deviation in the valve drive signal at these frequencies. Taking into account the 13.5% overlap of the spool, the valve opening is quite small at the lower frequencies. There would be some leakage around this point and as the flow is not yet fully developed, there is some variation in the flow coefficient C_q and the flow equation does not give a good representation of the actual situation [38]. As a good match was obtained over the principal frequency range and inputs at very low frequencies are unlikely to lead to dangerous transient stability states, the model was not developed further in order to obtain a better fit at lower frequencies.

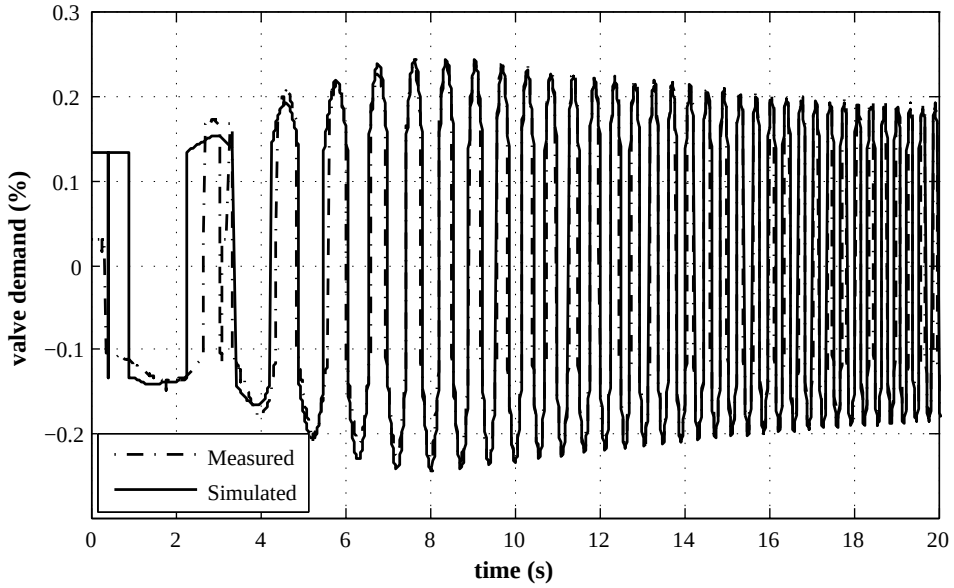

Figure 4.15: Resultant valve drive signal to virtual steer and speed input

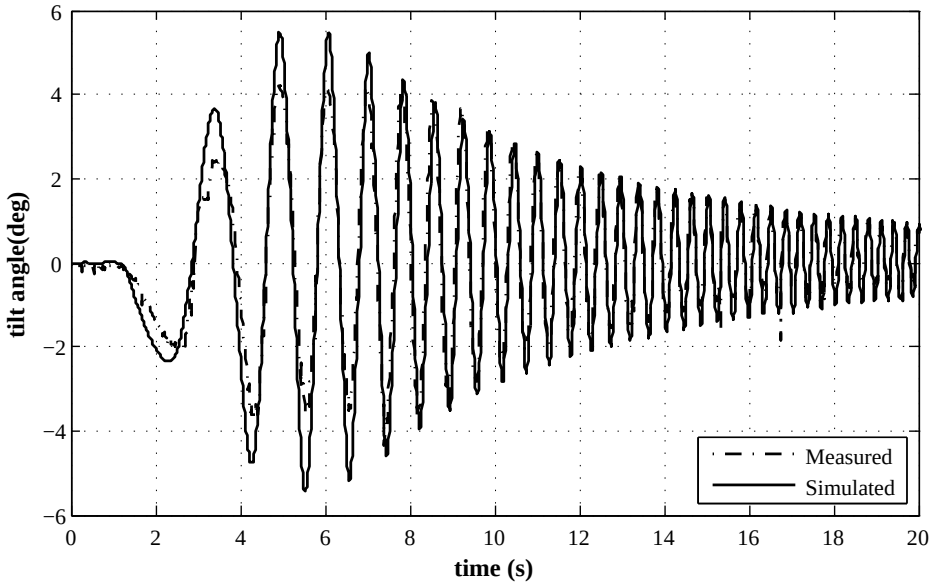

Figure 4.16: Tilt angle response to virtual steer and speed input

4.5 Concluding Remarks

Using the multi-body simulation and comparing the results with the measured frequency response gave a good understanding of the vehicle's behaviour in bounce and roll. The friction in the trailing arm was found to have a significant effect on the frequency response in bounce by locking the suspension in the lower frequency range and restricting the motion of the suspension across the frequency spectrum. Furthermore, it was found that there was a significant amount of flexibility in the tilt joint which also had an impact on the frequency response. These effects were modelled in order to verify that the inconsistencies in the frequency response could indeed be attributed to the trailing arm friction and tilt joint flexibility. However, as these are in essence unwanted effects that should be removed, they will not be included further in the study.

The frequency response tests were repeated a number of times for several amplitudes and this revealed that there was a significant amount of variability and non-linearity in the system. The non-linearity of the system response was much greater than initially anticipated and it should be said that using frequency response analysis is not ideally suited for non-linear systems. However, it did reveal the major harmonic frequencies which were particularly clear in the roll response and were in line with the estimates made in chapter 3.

The simulated frequency response was sufficiently accurate to validate the vehicle model in bounce and roll. The next stage is therefore the development of a lateral dynamics model. This will then be incorporated in the vehicle multi-body model along with the hydraulic valve and actuator model described in chapter 3. The full vehicle model will then be used as the platform to test a new control approach.

Chapter 5

Lateral Dynamics Modelling and Validation

The lateral and yaw dynamics of the vehicle are analysed using a single-track (bicycle) model of the vehicle, where the total force produced by the rear tyres is combined in a single component. This is permissible as the rear track width is small with regards to the turning radius. This modelling approach was chosen for its simplicity and its scope to determine some of the vital tyre characteristics through experimentation. As this study focuses on the vehicle dynamics at constant velocity, pure slip conditions were assumed. Fore and aft weight transfer resulting from acceleration, braking and aerodynamic drag have been ignored. The initial equations of motion are expressed with linear cornering and camber stiffnesses such as the ones used in the steady state handling study discussed in chapter 2. The tyre model is then expanded to use non-linear tyre characteristics and transient state dynamics are incorporated. Finally, the model is validated against test data for quasi-steady state manoeuvres and a good fit is established between the measured and simulated results. Rapid transient state steer inputs were not performed due to safety restrictions.

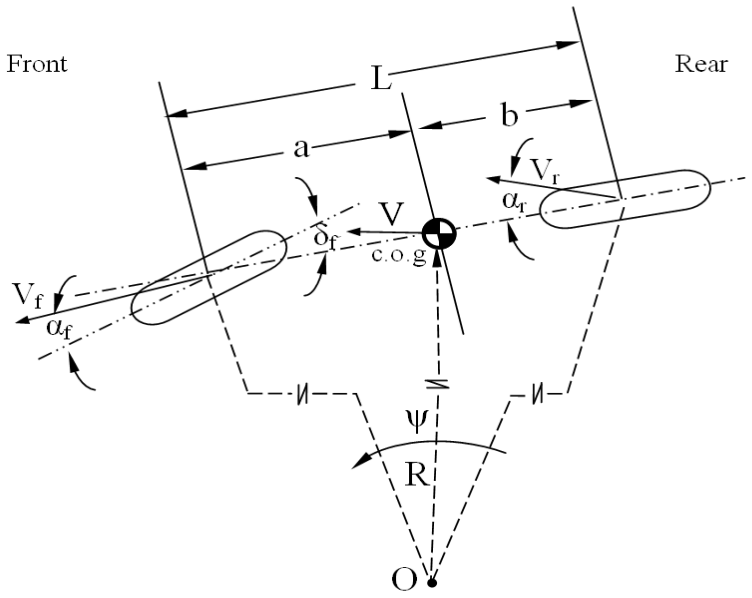

Figure 5.1: Bicycle model

5.1 Model Description

5.1.1 Equations of Motion

The bicycle model is often used for linear analysis where steer and slip angles are restricted to fairly small angles. This allows the variation in geometry to remain linear ($\cos\alpha \approx 1$ and $\sin\alpha \approx \alpha$ and similarly for the steer angle δ). However, a model such as the one shown in figure 5.1 lacks body roll and load transfer and therefore limits the theory to steady state scenarios where the roll moment remains small. This restriction is overcome by using effective axle characteristics in which the effects of body roll and load transfer have been included.

Using the model shown in figure 5.1, the equations of motion can be derived as shown in equations 5.1 and 5.2. The front side force F_{yf} is generated through sideslip α_f and camber γ_f, whereas the rear side force F_{yr} is generated principally through the rear tyre slip angle α_r. As we are representing the two rear tyres as a single component, the side force has to be doubled. The camber force of the rear tyres due to roll is minimal, and can therefore be neglected in the initial equations. The force resulting from the slip and camber are dependent on the tyre slip stiffness and camber stiffness $C_{\alpha f}$ and $C_{\gamma f}$ respectively. Their values depend on the type of tyre, on driving conditions and numerous other factors. The relationship between the side force and the slip and

camber angles are shown in equations 5.3 and 5.4. The slip angles are a result of the difference between the tyre direction and its velocity. The equations that describe this are equations 5.5 and 5.6. Note the rear steer term in equation 5.6, caused by the additional steer due to the inclination of the tilt axis. This is explained in detail in section 2.2.1.

$$m(\ddot{y} + \dot{x}\dot{\psi}) = F_{yf} + F_{yr} \tag{5.1}$$

$$I_z\ddot{\psi} = aF_{yf} - bF_{yr} \tag{5.2}$$

$$F_{yf} = C_{\alpha f}\alpha_f + C_{\gamma f}\gamma_f \tag{5.3}$$

$$F_{yr} = 2C_{\alpha r}\alpha_r \tag{5.4}$$

$$\alpha_f = \delta'_f - \tan^{-1}\left(\frac{\dot{y} + a\dot{\psi}}{\dot{x}}\right) \tag{5.5}$$

$$\alpha_r = \delta_r - \tan^{-1}\left(\frac{\dot{y} - b\dot{\psi}}{\dot{x}}\right) \tag{5.6}$$

5.1.2 Front Steer, Camber and Transient Slip Angles

To determine the side force F_y acting on the front wheel, the respective camber and steer angles are needed. For the rear wheels these can be found in a straightforward way. For the front wheel, the orientation of the wheel plane is defined by three successive rotations. Figure 5.2 depicts the coordinate systems which are needed to define the orientation of the driver cabin and front wheel. The line of intersection of the centre plane of the cabin and the road plane coincides with the x axis and the vehicle roll axis. The origin of the moving axis system (x, y, z) is reference point A and has the forward and lateral velocity components u and v. Furthermore this system rotates with a yaw rate $r = \dot{\psi}$. The cabin rotates around the tilt axis giving the relative tilt angle θ and the rear module rolls about the vehicle roll axis (x axis) with the angle ϕ. This gives rise to the rotated axes system $(x_\varphi, y_\varphi, z_\varphi)$ where $\varphi = \theta - \phi$ which is attached to the cabin frame. In this centre plane the steering axis is positioned at an angle of inclination equivalent to the caster angle ε with respect to the z_φ axis. The coordinate system

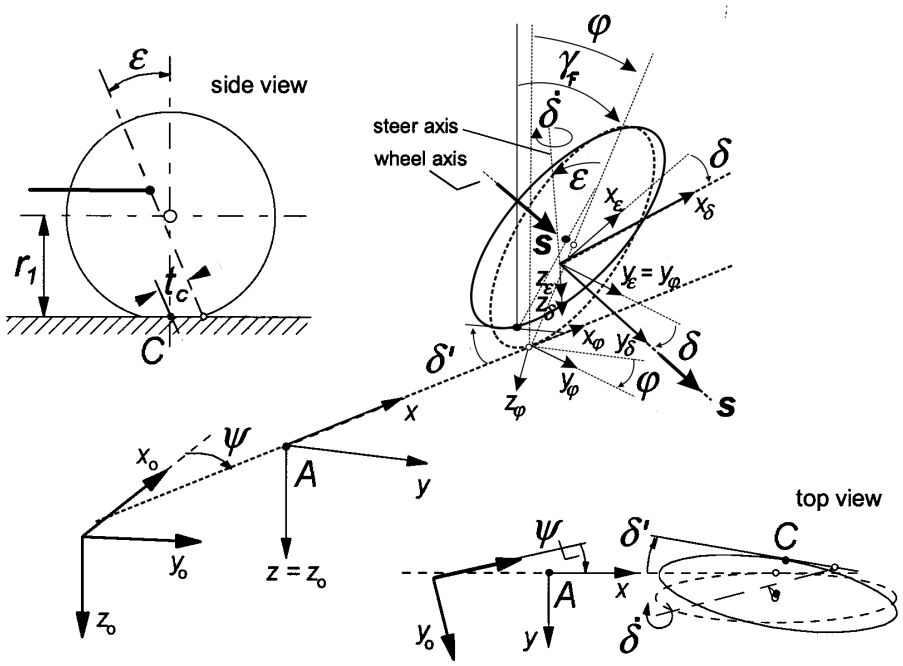

Figure 5.2: Front wheel assembly and coordinate systems (adapted from [36])

$(x_\varepsilon, y_\varepsilon, z_\varepsilon)$ is also attached to the frame with the z_ε axis along the inclined steering axis. Finally, the system $(x_\delta, y_\delta, z_\delta)$ is attached to the wheel hub and is rotated with steer angle δ with respect to the $(x_\varepsilon, y_\varepsilon, z_\varepsilon)$ reference frame. By introducing a unit vector $\mathbf{s}$ directed according to the wheel spin axis that is along the y_δ axis, the components of this vector along the axes of the moving horizontal system (x, y, z) can be determined by successive rotation transformations.

$$\mathbf{s}_\delta = \begin{pmatrix} 0 \\ 1 \\ 0 \end{pmatrix}, \qquad \mathbf{s}_\varepsilon = \begin{pmatrix} \cos\delta & -\sin\delta & 0 \\ \sin\delta & \cos\delta & 0 \\ 0 & 0 & 0 \end{pmatrix} \mathbf{s}_\delta,$$

$$\mathbf{s}_\varphi = \begin{pmatrix} \cos\varepsilon & 0 & \sin\varepsilon \\ 0 & 1 & 0 \\ -\sin\varepsilon & 0 & \cos\varepsilon \end{pmatrix} \mathbf{s}_\varepsilon, \qquad \mathbf{s} = \begin{pmatrix} 1 & 0 & 0 \\ 0 & \cos\varphi & -\sin\varphi \\ 0 & \sin\varphi & \cos\varphi \end{pmatrix} \mathbf{s}_\varphi \tag{5.7}$$

After this series of transformations, the unit vector is given by:

$$\mathbf{s} = \begin{pmatrix} -\sin\delta\cos\varepsilon \\ \cos\delta\cos\varphi - \sin\delta\sin\varepsilon\sin\varphi \\ \cos\delta\sin\varphi + \sin\delta\sin\varepsilon\cos\varphi \end{pmatrix} \tag{5.8}$$

The ground steer angle δ_f and the camber angle γ_f can be determined from the unit vector components, giving the non-linear expressions:

$$\tan\delta_f = -\frac{s_x}{s_y} = \frac{\sin\delta\cos\varepsilon}{\cos\delta\cos\varphi - \sin\delta\sin\varepsilon\sin\varphi} \tag{5.9}$$

$$\sin\gamma_f = s_z = \cos\delta\sin\varphi + \sin\delta\sin\varepsilon\cos\varphi \tag{5.10}$$

For the steady state scenario the slip angles are given by equations 5.5 and 5.6.

When looking at the non-steady state scenario, it is necessary to include the time rate of change of δ_f and the front slip angle becomes:

$$\alpha_f = \delta'_f - \tan^{-1}\left(\frac{\dot{y} + a\dot{\psi} - t_c\dot{\delta}_f}{\dot{x}}\right) \tag{5.11}$$

As the rate of change of δ_r is small, equation 5.6 remains valid for the transient state. With the steer, camber and slip angles it is possible to find the resulting lateral forces.

5.1.3 Front Tyre Model

The non-linear force description of the front motorcycle tyre makes use of a simplified version of the magic formula [36]. As we are looking at lateral motion of the vehicle only, the effects of fore and aft load transfer resulting from braking, accelerating and air drag have been omitted.

C_α	$9.74\ F_z$	d_4	1.2	d_7	0.15
C_γ	$0.86\ F_z$	d_6	0.1	d_8	1.6

Table 5.1: Front Tyre Magic Formula Parameters

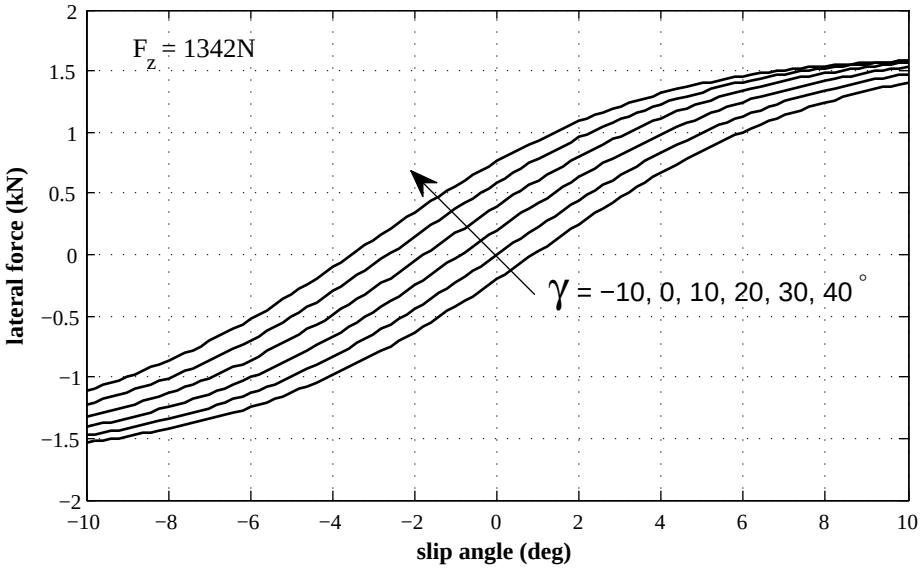

Figure 5.3: Effect of camber on lateral force

$$F_y = D\sin[C\tan^{-1}(B(\alpha' + S_H))] + S_V \tag{5.12}$$

$$C = d_8 \tag{5.13}$$

$$D = \frac{d_4 F_z}{1 + d_7\gamma^2} \tag{5.14}$$

$$B = \frac{C_\alpha}{CD} \tag{5.15}$$

$$S_{Hf} = \frac{C_\gamma \gamma'}{C_\alpha} \tag{5.16}$$

$$S_V = d_6 F_z \gamma' \tag{5.17}$$

$$S_H = S_{Hf} - \frac{S_V}{C_\alpha} \tag{5.18}$$

The values for the parameters involved have been listed in table 5.1. The parameters $d_4 - d_8$ relating to the non-linear region of the slip - lateral force curve were taken from Pacejka's tyre model [36].

5.1.4 Rear Tyre model

The rear tyres were modelled based on Pacejka's 'Magic Formula' or semi-empirical tyre model for car tyres. Due to the limiting testing facilities available, the Similarity Method [36] will be used to determine the parameters. This method is based on the observation that the pure slip curves remain approximately similar in shape when the tyre runs at conditions that are different from the reference condition. For the purposes of this study, the reference condition is defined as the state where the tyre runs at its nominal load (F_{z0}) at camber angle equal to zero ($\gamma = 0$), free rolling and on a given road surface (μ_0). A similar shape means that the characteristics that belong to the reference condition is regained by shifting and multiplication in the horizontal and vertical direction. A demonstration that in practice similarity does indeed occur is given by Radt and Milliken [39] and by Milliken and Milliken [40]. The formula used to calculate the lateral force is shown in equation 5.19.

$$y = D \sin[C \tan^{-1}(Bx - E(Bx - \tan^{-1} Bx))] \tag{5.19}$$

with

$$F_y = y(x) + S_v \tag{5.20}$$

$$x = \tan\alpha + S_h \tag{5.21}$$

and the other variables are named as follows:

- B: stiffness factor
- C: shape factor
- D: peak value
- E: curvature factor
- S_h: horizontal shift
- S_v: vertical shift

The Magic Formula $y(x)$ generally produces a curve that passes through the origin $x = y = 0$, reaches a maximum and then tapers to a horizontal asymptote. For certain

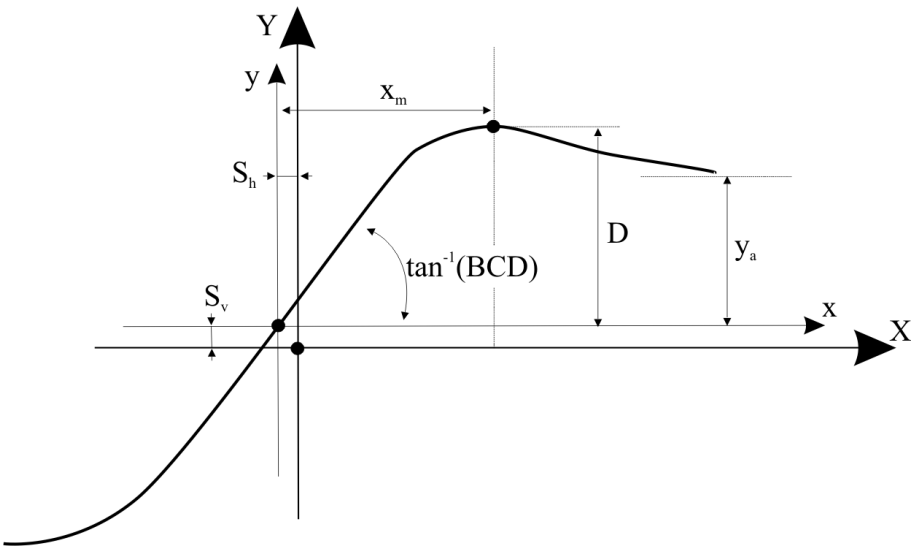

Figure 5.4: Curve produced by the Magic Formula, equation 5.19

.

values of the coefficients B,C,D and E the curve shows an anti-symmetric shape with respect to the origin. The vertical and horizontal shifts S_v and S_h allow the curve to have an offset with respect to the origin. The meaning of the curve parameters are indicated in figure 5.4.

From the heights of the peak and of the horizontal asymptote, the shape factor C can be calculated according to equation 5.22

$$C = 1 \pm \left(1 - \frac{2}{\pi} \tan^{-1} \frac{y_a}{D}\right) \tag{5.22}$$

B can be determined from the slope at the origin corresponding to the product BCD. From B and C and the location of x_m of the peak value of E can be obtained through equation 5.23

$$E = \frac{Bx_m - tan(\frac{\pi}{2C})}{Bx_m - tan^{-}1(Bx_m)} \quad (if \quad C > 1) \tag{5.23}$$

To accommodate for the asymmetry of the F_y vs α curve that is often associated with the offsets S_v and S_h (which can be considerable when applying wheel camber), the curvature factor E is made dependent of the sign of the (x) value. Shown in

equation 5.24.

$$E = E_0 + \Delta E \, sgn(x) \tag{5.24}$$

According to these definitions, the individual coefficients can be derived with experimental data. It was attempted to obtain experimental data (section 5.2.2) to determine accurate parameters for the model. However, due to insufficient instrumentation accuracy, it was necessary to use suggested values from Pacejka's tyre model instead [36]. The similarity method will be used to derive the tyre characteristics at the operating load for the rear tyres on CLEVER (1350N) and compared to the characteristics at the nominal load F_{zo} given in [36] of 3000N. The parameters used are listed in table 5.2.

The cornering stiffness is given as a function of the wheel load:

$$C_\alpha = c_1 c_2 F_{zo} \sin\left(2 \tan^{-1}\left(\frac{F_z}{F_z o}\right)\right) \tag{5.25}$$

The peak factor for the side force is given by:

$$D_o = \mu_0 F_{zo} \tag{5.26}$$

The stiffness factor is given by:

$$B_o = \frac{C_\alpha}{C D_o} \tag{5.27}$$

Finally, the side force at nominal load F_{zo} is given by:

$$F_{yo} = D_o \sin[C \tan^{-1}(B_o x - E(B_o x - \tan^{-1} B_o x))] \tag{5.28}$$

where $x = \tan \alpha$.

The wheel load affects both the peak level (where the saturation of the curve takes

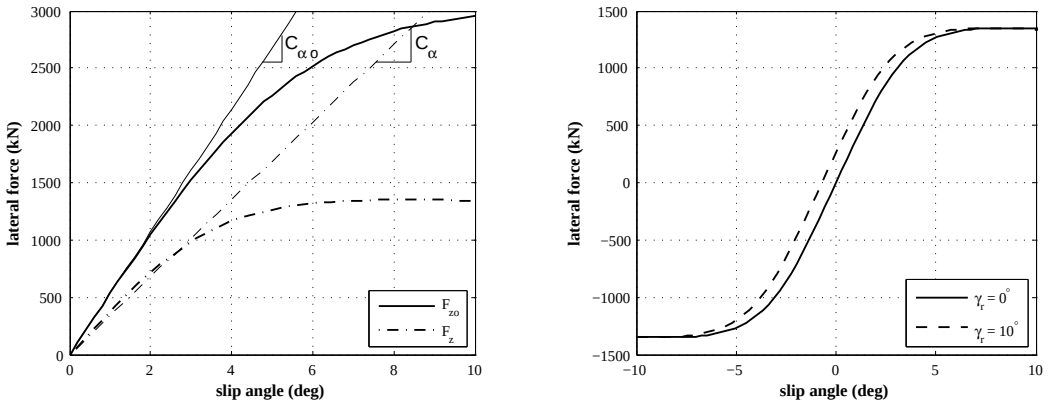

(a) (b)

Figure 5.5: Using the similarity method to adapt F_y to a new load (a) and to introduce a camber angle (b)

place) and the slope where $\alpha \to 0$ i.e. the slip stiffness C_α. The first effect is obtained by multiplying the original characteristic equation by the ratio F_z/F_{zo}. This results in the new function:

$$F_y = \frac{F_z}{F_{zo}} F_{yo}(\alpha_{eq}) \tag{5.29}$$

The second step in the manipulation of the original curve is the adaptation of the slope at $\alpha = 0$ which is achieved by horizontal multiplication of the new characteristic curve accomplished with the equivalent slip angle:

$$\alpha_{eq} = \frac{F_z o}{F_z} \alpha \tag{5.30}$$

The resultant transformation in the F_y against α characteristic curve is shown in figure 5.5 (a).

As the rear module rolls, small levels of camber thrust will be introduced as a result of the rear wheel camber $\gamma_r = \phi$. For small angles the camber thrust generated by the rear tyres can be approximated by the product of the camber stiffness and the camber angle [36]. This results in a horizontal shift S_h of the α_r against F_{yr} curve equivalent to:

F_{zo}	3000N	C	1.3	c_1	8	μ_0	1
F_z	1350N	E	-1	c_2	1.33		

Table 5.2: Rear tyre magic formula parameters

$$S_h = \frac{C_\gamma(F_z)}{C_\alpha(F_z)}\gamma \tag{5.31}$$

This gives the equivalent slip angle α_{eq} (5.30) where α is replaced with $\alpha + S_h$. The resultant shift in lateral force for a given slip angle is shown in figure 5.5 (b).

5.1.5 Single Contact Point Transient Tyre Model

As the transient state lateral forces play an important role in this study, tyres with a side force subject to a first order lag will be introduced. The relaxation length of a tyre is the distance a wheel has to travel to reach 63 % of the steady state force [41] and is denoted as σ. The relaxation length for the camber angle has been shown to be negligible [41], [36]. The following equations describe the generation of the transient state side slip angles $\alpha_f^{'}$ and $\alpha_r^{'}$ and resulting lateral force:

$$F_{yf} = C_{\alpha f}\alpha_f^{'} + C_{\gamma f}\gamma_f \tag{5.32}$$

$$F_{yr} = 2C_{\alpha r}\alpha_r^{'} \tag{5.33}$$

$$\alpha_f = \frac{\sigma}{\dot{x}}\dot{\alpha}_f^{'} + \alpha_f^{'} \tag{5.34}$$

$$\alpha_r = \frac{\sigma}{\dot{x}}\dot{\alpha}_r^{'} + \alpha_r^{'} \tag{5.35}$$

Figure 5.6 shows the normalised lateral force response or lateral acceleration response to a step steer input with and without lagged tyres.

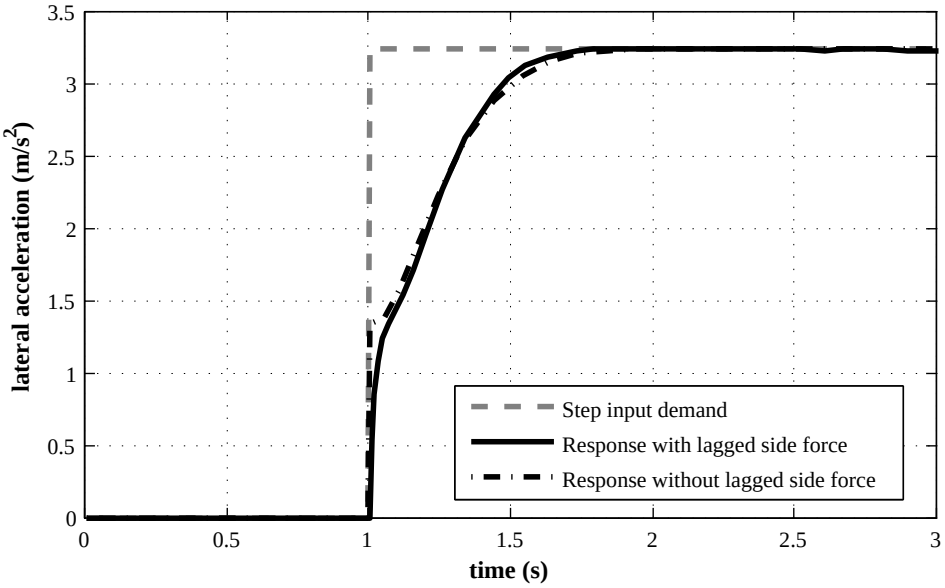

Figure 5.6: Example of lateral acceleration response to a step steer input using a tyre model with and without lagged side force

5.1.6 Effective Axle Cornering Characteristics

To incorporate the effects resulting from the load transfer across the rear axle, effective axle cornering characteristics are used. This should enable prediction of the steady state and quasi- steady state handling characteristics of the vehicle. This approach can be used as long as the steering wheel angle input frequency can be considered small relative to the body roll natural frequency [36]. In the case of CLEVER, the roll natural frequency of the vehicle is 2.4Hz with roll-bar and 1.3Hz without, as determined analytically (chapter 3) and confirmed through practical experiments (chapter 4).

In order to accurately estimate the load transfer across the rear wheels it is necessary to have an estimate of the rear module roll. As the rear module rolls out of the corner, the vehicle weight is shifted towards the outer wheel. Furthermore, the rear roll angle reduces the absolute tilt angle of the cabin, which causes further weight shift onto the outer wheel. The rear module rolls about the vehicle's roll axis, which connects the front and the rear roll centres. In CLEVER's case, the front roll centre is clearly located at ground level. Similarly, as a result of the trailing arm suspension setup at the rear, the rear roll centre is also located at ground level. The roll axis therefore lies along the centre of the vehicle at road height. There are no compliance effects resulting from the suspension that affect the front and rear wheel steer and slip angles. However,

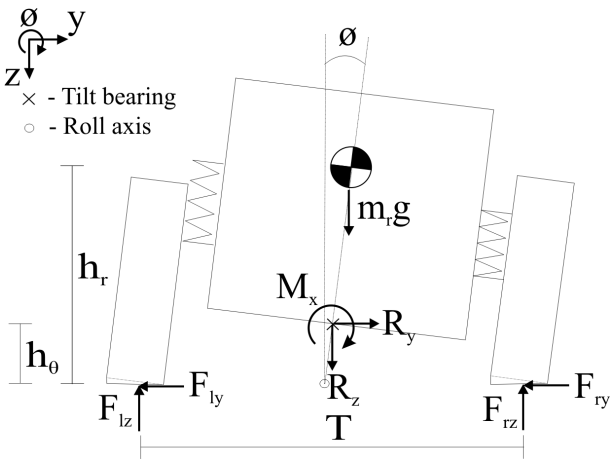

Figure 5.7: Free body diagram of the rear module

camber at the rear wheels is induced by body roll. It is common to model the effects of body roll using a torsional spring located at the roll centre to represent the roll stiffness which results from the suspension springs and anti-roll bars. This approach was taken for the analysis of the data obtained through testing. The rear roll stiffness K_ϕ as a function of the rear suspension spring stiffness K_s and anti-roll bar stiffness K_r is shown in equation 5.36. The modelling of the suspension and the calculation of the roll stiffness is discussed in detail in chapter 3.

$$K_\phi = \frac{K_s T^2}{2} + K_r \tag{5.36}$$

The vehicle roll can be calculated based on the forces acting about the roll centre. As the tests were performed in steady state or at low frequencies, it is possible to neglect the dynamics of the damping elements. Figure 5.7 depicts the forces acting on the rear module in steady state.

If we assume small angles, the moments about the rear module CoG are given by:

$$M_R = F_{lz}(\frac{T}{2} + h_r\phi) - F_{rz}(\frac{T}{2} - h_r\phi) + (F_{ly} + F_{ry})h_r - R_z(h_r - h_\xi)\phi - R_y(h_r - h_\xi) + M_x \tag{5.37}$$

where in steady state, the moment M_x is given by

$$M_x = (g \sin\theta_e - a_y \cos\theta_e) m_{cd} h_{cd} \tag{5.38}$$

where m_{cd} and h_{cd} are the combined cabin and driver mass and CoG height from the ground. The equivalent cabin tilt angle resulting from the raised tilt axis (section 2.2.2) θ_e is given by:

$$\theta_e = \tan^{-1}\left(\left(1 - \frac{h_{cd}}{h_\xi}\frac{a_c}{a_\theta}\right)\tan(\theta - \phi)\right) \tag{5.39}$$

An accurate estimation of the forces acting on the cabin is necessary in order to calculate the resulting moment acting on the rear module. As the angles here can be large, it was chosen not to linearise this equation. The roll angle is given by the quotient of the moment and the roll stiffness:

$$\phi = \frac{M_R}{K_\phi} \tag{5.40}$$

Combining equations 5.37 and 5.40 results in the following expression for roll angle ϕ:

$$\phi = \frac{(F_{lz} - F_{rz})\frac{T}{2} + (F_{ly} + F_{ry})h_r - R_y(h_r - h_\xi) + M_x}{K_\phi + R_z(h_r - h_\xi) - (F_{rz} + F_{lz})h_r} \tag{5.41}$$

Using the above equation, it is possible to estimate the vehicle or rear module roll at steady state at any tilt angle position. The load transfer ΔF_z from the inner to the outer wheel in a steady state cornering motion is given by the quotient of the moments acting on the rear module and its track.

$$\Delta F_z = \frac{M_R}{T} \tag{5.42}$$

Using the calculated load transfer, the loads on the individual rear wheels can be calculated. In experiments, when the vehicle moves steadily around a circular path, the body roll angle can be calculated through the rear suspension displacement at either side, which will be used to evaluate the effective axle cornering characteristics.

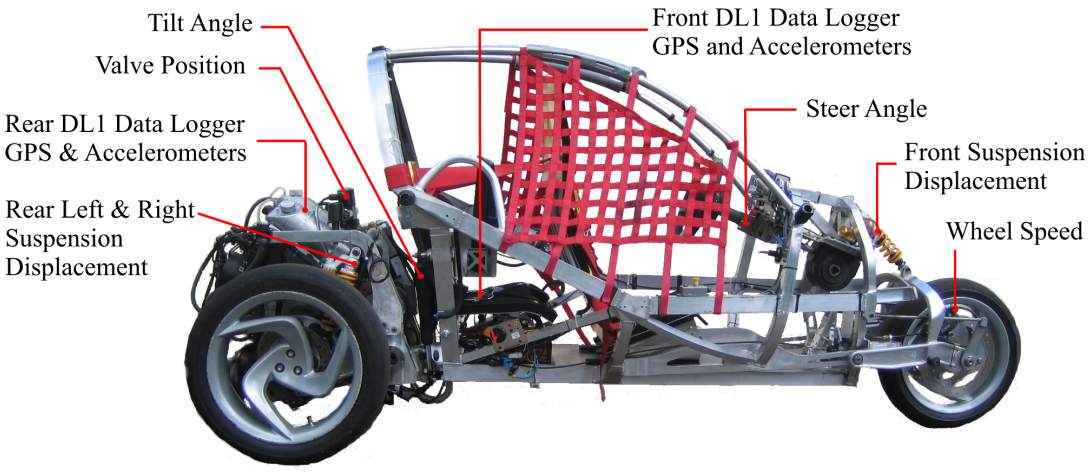

Figure 5.8: Sensor and data logger locations

5.2 Lateral Dynamics Testing

The CLEVER vehicle was set up with a range of sensors in order to obtain experimental data and validate the lateral dynamics model. A number of standard dynamic tests were performed to obtain the required data. As previously mentioned, in order for the bicycle model to be valid, it is necessary to keep the forward speed constant. Ideally the tests would be performed on a smooth surface with constant texture and zero gradient, and be performed by a driving robot in order to keep all parameters constant. For numerous reasons this was not possible. However, the theory is also said to hold approximately for quasi-steady-state situations, i.e. with moderate braking or driving [36]. It was therefore deemed to be useful to perform the tests with a human driver. The testing area was located on a military airfield on a tarmac surface with a marginal gradient. This meant that in steady state the vehicle still had changes in acceleration due to the slope of the test grounds. Although it was attempted to smooth out these variations in longitudinal acceleration as best as possible by the driver, they can still be seen in the test results. However, the results show a good correlation between the measured and simulated data and are mainly unaffected by these small accelerations.

5.2.1 Experimental Setup

The sensor locations are shown in figure 5.8. The DL1 is a data logging system with GPS receiver and dual axis accelerometers (lateral and longitudinal). The sampling

	Sampling Frequency	Range	Resolution
Accelerometers	100 Hz	2g	0.005g
GPS	10Hz	-	Position: 3m Speed : 0.1mph

Table 5.3: GPS and accelerometer specifications

Symbol	Description	Unit
GPS		
t	Time	[s]
v	Vehicle speed	[m·s^{-1}]
R	Cornering radius	[m]
X	X position from reference point A	[m]
Y	Y position from reference point A	[m]
$\dot{\psi}$	Yaw rate	[rad·s^{-1}]
ψ	Yaw	[rad]
Accelerometers		
a_{yc}	Acceleration measured inside the cabin	[m·s^{-2}]
a_{yr}	Acceleration measured on rear module	[m·s^{-2}]
Potentiometers		
x_f	Front suspension deflection	[m]
x_{rl}	Rear left suspension deflection	[m]
x_{rr}	Rear right suspension deflection	[m]
δ_f	Steer angle at the front wheel	[rad]
θ	Relative angle between cabin and rear module	[rad]

Table 5.4: Measured Test Parameters

frequency and accuracy of the GPS sensor and accelerometers are given in table 5.3. The DL1 uses the GPS data to derive several useful parameters for the analysis of the vehicle's dynamics. These are listed in table 5.4 along with the other measured signals. Furthermore, the DL1 utilises the accelerometer data to interpolate between the 0.1s time steps from the GPS data to obtain signals of 100Hz. The details of this interpolation procedure were unavailable. The other sensors are all sampled at 100Hz, which was considered sufficient to capture all the dynamic effects that are to be investigated.

5.2.2 Tyre Model Identification from Test Data

The parameters required for the bicycle simulation model that are inherent to the vehicle are its mass m, the yaw inertia I_z, the longitudinal distances of the front and

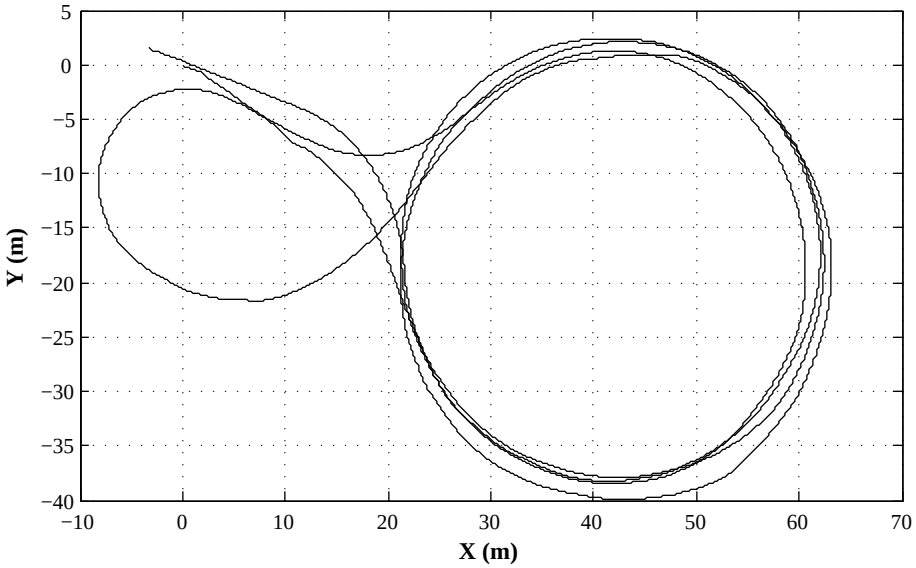

Figure 5.9: Path of a steady state manoeuvre

rear tyre contact patches to the vehicle's centre of mass a and b, the slip stiffness of the front and rear tyres $C_{\alpha f}$ and $C_{\alpha r}$ and the front camber stiffness $C_{\gamma f}$. The total mass and its distribution across the front and rear axles could be accurately measured using a set of scales (chapter 3). The yaw inertia was estimated from CAD data and the tyre stiffnesses were initially estimated from references to similar tyres in published literature. The front tyre is an Avon 120/70ZR17 motorcycle tyre, whereas the rear tyres were custom 160/55R18 tyres made by Avon with a construction similar to that of a car tyre. A range of techniques have been used in the past to measure tyre slip stiffnesses and include trailer tests ([42], [43]), flat plank tests [44], rolling drum tests [45] and rotating disc tests [46]. A GPS based approach has also proven to be successful for estimating tyre stiffnesses and friction coefficients ([47], [48], [49]), although it was noted that some of the accuracies of the GPS recievers used in the aforementioned studies were much higher (up to a position accuracy of 25mm). The tests performed here were conducted on a clear day on an open airfield away from any objects that could obstruct the direct communication of the GPS reciever to the GPS satellites.

Figure 5.9 shows the path followed for a steady state measurement test, plotted from the X and Y coordinates obtained from the GPS. The vehicle sets off from point A at the origin, enters a left hand turn, completes two full circles, turns around and completes two right handed circles and returns to its point of origin.

It can be seen that the radius of these turns are not perfectly constant, which is due to

the driver having to regulate the vehicle velocity in order to compensate for the small slope on the test ground. As previously mentioned the experimental data referred to as being steady state in this report is in fact in 'quasi' steady state, but can still be used for steady state analysis.

To obtain the front and rear slip angles (equation 5.5 and 5.6), it is necessary to separate the lateral and longitudinal velocity components of the vehicle. The Cartesian coordinates X and Y provided from the GPS from a reference point A [0,0] need to be transferred to the moving axis coordinate system of x and y. The relations between the two sets of variables are shown in equations 5.43 and 5.44.

$$\dot{x} = \dot{X}\cos\psi + \dot{Y}\sin\psi \tag{5.43}$$

$$\dot{y} = -\dot{X}\sin\psi + \dot{Y}\cos\psi \tag{5.44}$$

The lateral velocity $\dot{y}$ is the critical parameter in the successful derivation of the front and rear slip angles. As it is derived by taking the difference between two sinusoidal signals, its accuracy is entirely dependent on the positional accuracy of the GPS signal.

Data processing

The majority of the signals required filtering due to high frequency noise corrupting the signal. In accelerometer signals, the majority of the noise came from irregularities in the road surface. On the rear accelerometer, vibrations caused by the engine and drivetrain significantly corrupted the signal. The main noise source on the potentiometers was due to their susceptibility to damage. Nearly all potentiometers had small track sections that were damaged and where the voltage would drop momentarily to zero. Finally, the GPS speed data required filtering to smooth the noisy signal caused by the combination of a comparatively low sampling rate and poor resolution and the requirement to differentiate the position. The effective sampling frequency of 10Hz means that the maximal measurable (Nyquist) frequency of the test data was 5Hz. Thus, it was necessary to apply a 2Hz low-pass Butterworth filter to filter out the majority of the noise in all signals. Although this meant that some dynamic effects would be lost in the filtering, the frequencies investigated in quasi-steady state analysis stayed well below the 1.3Hz body roll natural frequency. A 2Hz cut-off frequency was therefore deemed appropriate for this analysis.

Results

Using the raw data to derive the lateral velocity $\dot{y}$ according to equation 5.44, resulted in a very noisy signal. Even with filtering, it was not possible to derive a useful signal. Figure 5.10 shows the resultant values for the steady state manoeuvre depicted in figure 5.9. The simulated results using the cornering and camber stiffnesses from literature are also depicted to show the order of magnitude that was expected. The inputs to the simulation were the measured speed (GPS) and steer. It can be seen that the noisiness of the signal, which is believed to be a result of the lack of accuracy of the GPS, is too significant to obtain coherent values for the lateral velocity. The only section which appears to approximately match the simulated results is the transient section where the vehicle is turned around mid-test. The evaluation procedure was repeated for a figure of 8 test, to see if this led to better results (figure 5.11). Similarly to the steady state results, a trend showing the lateral velocity drifting into positive and negative regions depending on the steering direction could be seen. It was, however, still impossible to obtain a clear and usable signal. This method purely based on GPS data therefore had to be disregarded due to its lack in accuracy.

Another method of calculating the lateral velocity is to use the measured lateral acceleration. If this represents the total lateral acceleration, the product of the yaw and speed GPS signals could be subtracted from it to give the linear lateral acceleration (equation 5.45), which could be integrated to give the lateral velocity. However, simulation showed that the values for the linear lateral acceleration $\ddot{y}$ are typically far below the 0.05m/s^2 tolerance of the accelerometer. Furthermore, external effects such a road and engine vibrations as well as lower frequency effects due to vehicle roll would significantly affect the accelerometer signal, such that variations of the order of 0.05m/s^2 would be meaningless.

$$\ddot{y} = a_y - v\dot{\psi} \tag{5.45}$$

In conclusion the accuracy of the measurement system used was insufficient to obtain accurate estimates of the lateral velocity. This means that it was impossible to calculate slip angles and derive cornering stiffnesses with the current set-up. This is emphasised when looking at the effect of the slip stiffnesses on the yaw rate and lateral acceleration of the vehicle, which is discussed in section 5.3. Much higher accuracy could be achieved by the use of a differential global position system (DGPS), which uses an earthbound

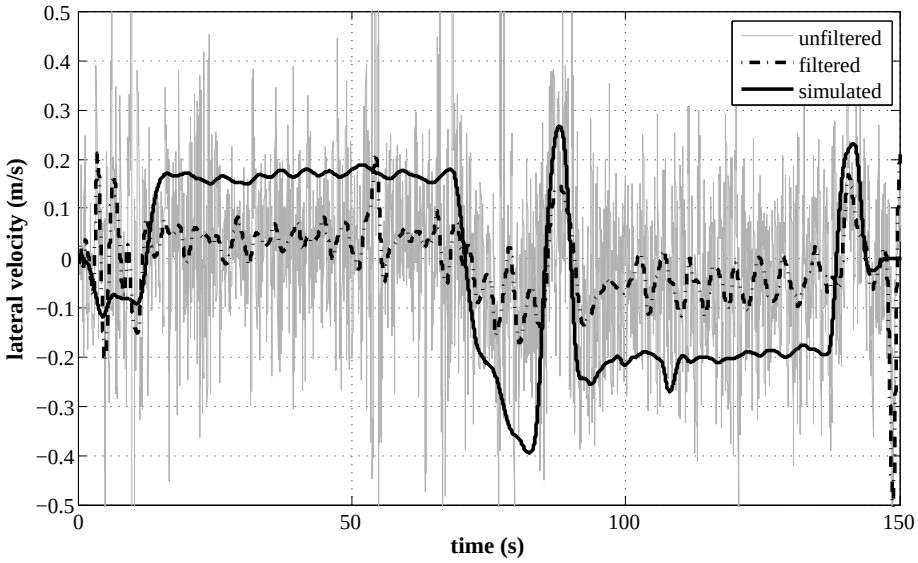

Figure 5.10: Steady state lateral velocity (t = 20-70 seconds and t = 100-140 seconds); derived from GPS data and simulated

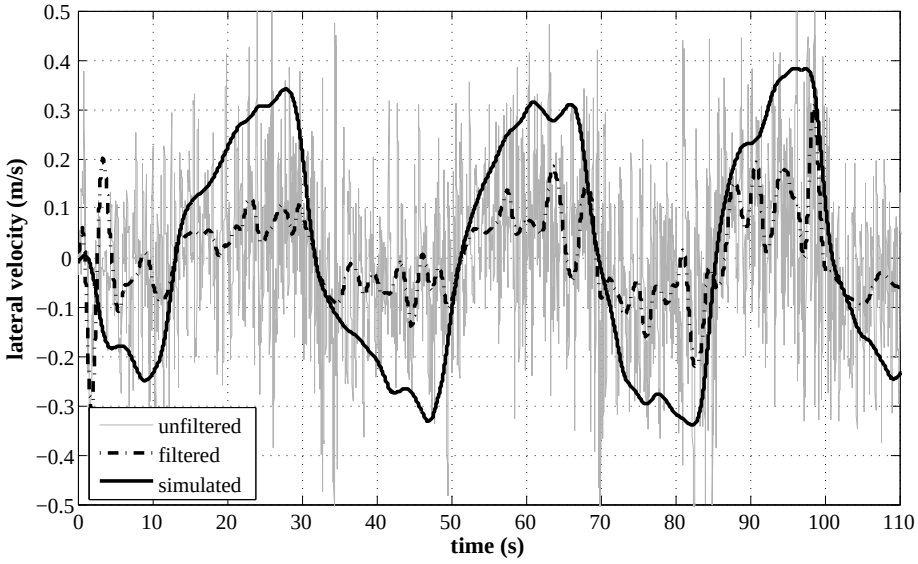

Figure 5.11: Lateral velocity for a figure of 8 manoeuvre

reference station in addition to the three required satellites. These systems can provide a position accuracy of 200mm and this can be increased to 25mm by performing the tests close to the reference station and statically initialising the system [48].

5.3 Lateral Dynamics Model Validation

The main quantity of interest in the model and handling analysis is the lateral acceleration. It relates directly to the forces generated by the tyres which can lead to the roll-over of the vehicle and also determines the trajectory of the vehicle. Although the bicycle model is generally limited to steady state driving, the accuracy of the model was also explored for quasi-steady state manoeuvres, figure of 8 tests and regular driving with moderate steering inputs. Transient performance resulting from rapid steering inputs was not investigated due to safety concerns and limitations in the instrumentation.

5.3.1 Lateral Motion without Tilting

As discussed previously the main unknown parameters were the yaw inertia, the tyre slip stiffnesses and the camber stiffness. It was previously shown that it was not possible to measure the lateral velocity and therefore slip angles and slip stiffness coefficients. It was therefore decided to do a sensitivity study of the parameters to investigate their effect on the lateral acceleration. The input parameters for the simulation were the vehicle speed measured from the GPS and the steer angle.

The vehicle yaw inertia was found to have almost no effect on the lateral acceleration of the vehicle in steady state when varying it within a reasonable range, and is therefore not shown. The front and rear slip stiffnesses were varied by +/- 50 % which led to small changes in the lateral acceleration. The results for a steady state circle test such as the one shown in figure 5.9 and a figure of 8 manoeuvre are shown in figures 5.12 to 5.15.

The low frequencies present in the steady state sections are a result of small adjustments in the speed and steer of the vehicle which were required for the driver to follow the desired trajectory. It can be seen that when changing the front and rear slip stiffnesses within a reasonable range, there is very little effect on the lateral acceleration of

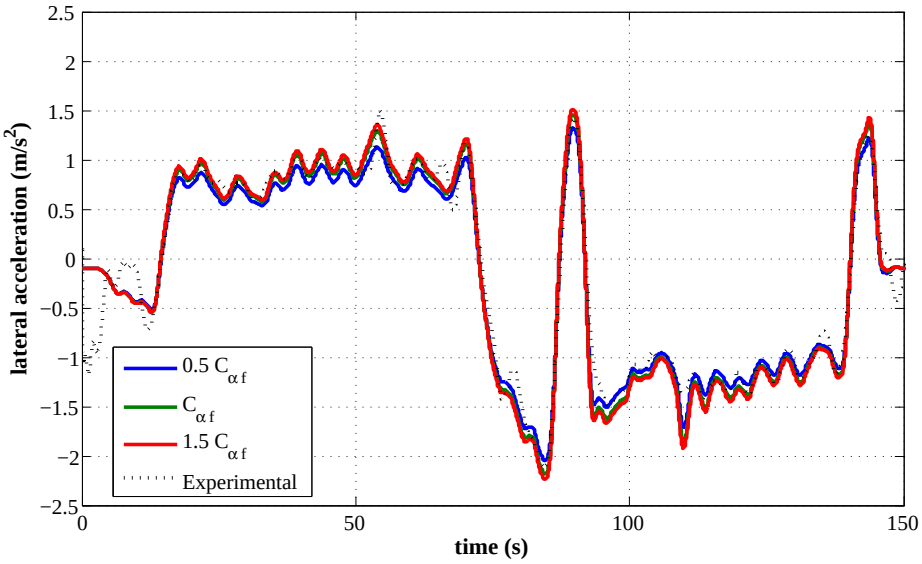

Figure 5.12: Effect of front tyre slip stiffness on lateral acceleration for a steady state manoeuvre (t = 20-70 seconds and t = 100-140 seconds)

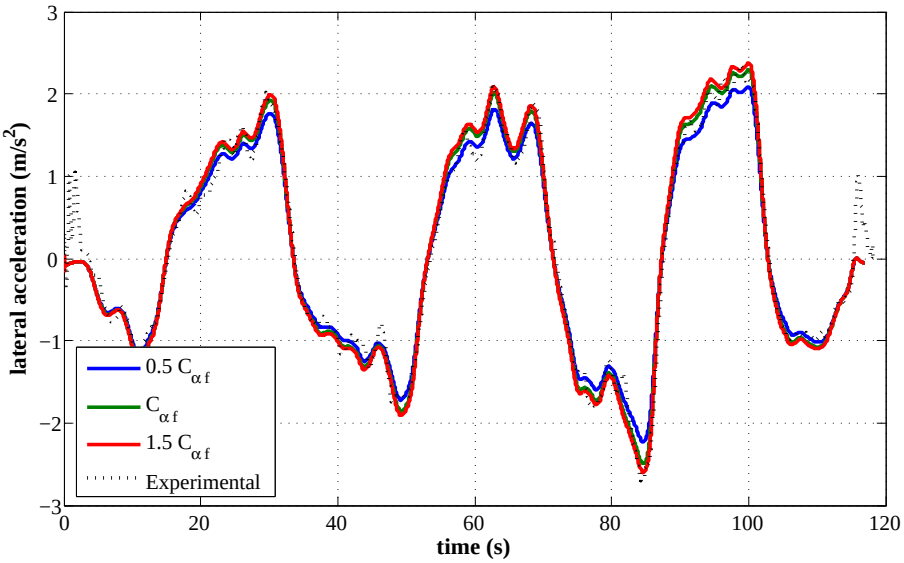

Figure 5.13: Effect of front tyre slip stiffness on lateral acceleration for a figure of 8 manoeuvre

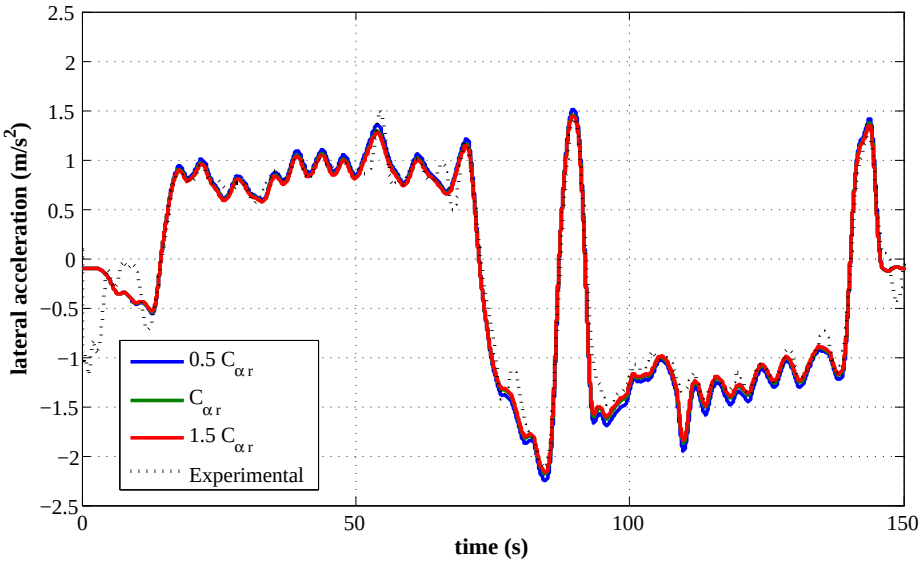

Figure 5.14: Effect of rear tyre slip stiffness on lateral acceleration for a steady state manoeuvre (t = 20-70 seconds and t = 100-140 seconds)

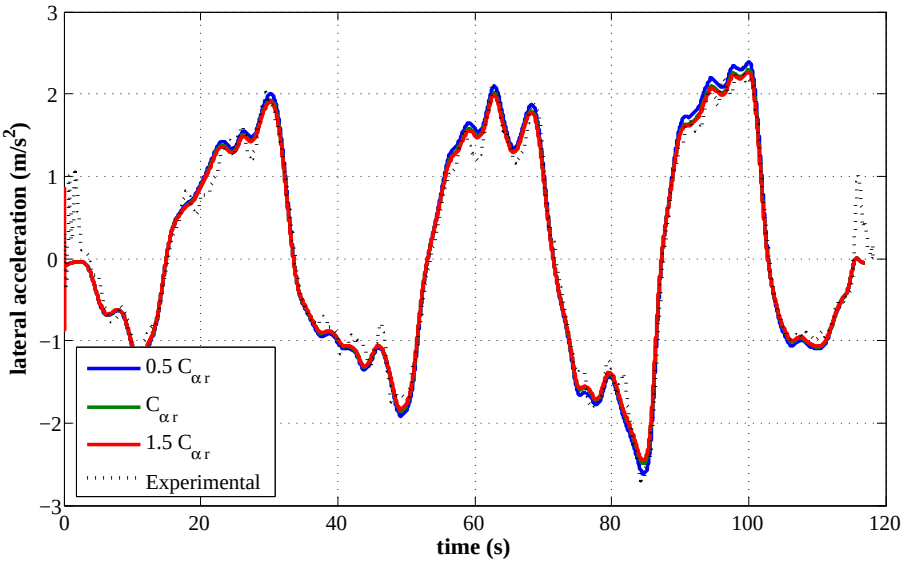

Figure 5.15: Effect of rear tyre slip stiffness on lateral acceleration for a figure of 8 manoeuvre

the vehicle. The values for the front and rear slip stiffnesses estimated from published data were therefore adopted. Furthermore, this means that changes in slip stiffness due to temperature changes and variations in surface are unlikely to have a significant effect on the steady state performance of the vehicle at these levels of lateral acceleration. The effect of slip stiffness is anticipated to be more significant at higher lateral accelerations and in rapid transient manoeuvres. However, this aspect could not be explored experimentally for safety reasons.

With the bicycle model validated using data without tilting action, the next step is to validate the model when the cabin and the rear module move separately resulting in additional cornering forces.

5.3.2 Lateral Motion with Tilting

When the vehicle is tilting, additional tyre forces arise resulting from camber as well as additional rear wheel steer. To get accurate results it is important to establish the absolute tilt angle at the wheel. This is the difference between the measured tilt angle and the rear roll angle. The wheel camber and steer angles can then be established according to equations 5.9 and 5.10. The relative tilt angle between the cabin and the rear module is measured by the linear potentiometer located between the two units. The rear module roll therefore affects the absolute tilt angle reached by the cabin and plays an important role in the stability of the vehicle. An estimation of the steady state roll was discussed in section 5.1.6 and a comparison with the measured roll is discussed in the following section.

Rear module roll

The roll of the vehicle can be measured in a number of ways. Firstly, it can be measured through the difference between the GPS measured lateral acceleration $a_{y,gps}$ and that measured by the accelerometer positioned on the rear module a_{yr}. The difference between the two signals is equivalent to the $g \sin \phi$ component measured by the accelerometer. Secondly, the roll can also be measured using the suspension displacements (and adding an additional 7% for the tyre compliance). However, it was found that the accelerometer signals were significantly affected by road noise and engine noise. After filtering it was found that the suspension potentiometers gave the cleanest results. This method is therefore used to compare the measured roll to the predicted roll

using the effective axle cornering characteristics.

As the moment resulting from the cabin can contribute significantly to the overall moments acting on the rear module, the predicted rear module roll was compared with the measured roll with the vehicle tilting as well as with the cabin locked upright (i.e. without tilting action). Figure 5.16 shows the rear module roll for a figure of 8 manoeuvre with the cabin in the upright position. It can be seen that the predicted roll is significantly smoother than the measured roll. The jagged appearance of the measured roll is thought to be a result of the high friction levels in the trailing arms (3.3.1). Furthermore, the small inclination of the testing grounds as well as irregularities in the road surface could also result in weight shifts that cause the measured roll angle to deviate from the predicted value.

The roll angle with the vehicle driving under normal operating conditions, i.e. with tilting is shown in figure 5.17. Even though a number of irregularities can be seen, the trend is followed well and it can be said that the effective axle cornering characteristics give a good approximation to the roll of the rear module.

Simulated lateral acceleration response

It was previously shown that the model gave a good fit with the cabin in the upright position where cornering forces were dominated by the front and rear slip angles. Figure 5.18 shows the results for a steady state manoeuvre with tilting and figure 5.19 shows the results for the vehicle driving with moderate steering inputs. It can be seen that the model gives a very accurate estimate of the vehicle lateral acceleration under the tested conditions. The input parameters for the model were steer, speed and relative tilt angle. Some sections in figure 5.19 that deviate from the measured lateral acceleration (i.e. at 5, 20 and 70 seconds) were found to be due to noise in the recorded steer signal at those points.

5.4 Concluding Remarks

The mathematical model for the lateral dynamics using non-linear tyre characteristics with transient dynamics was presented. As the range of tests were limited due the known stability issues of the vehicle in its current set-up, especially in transient ma-

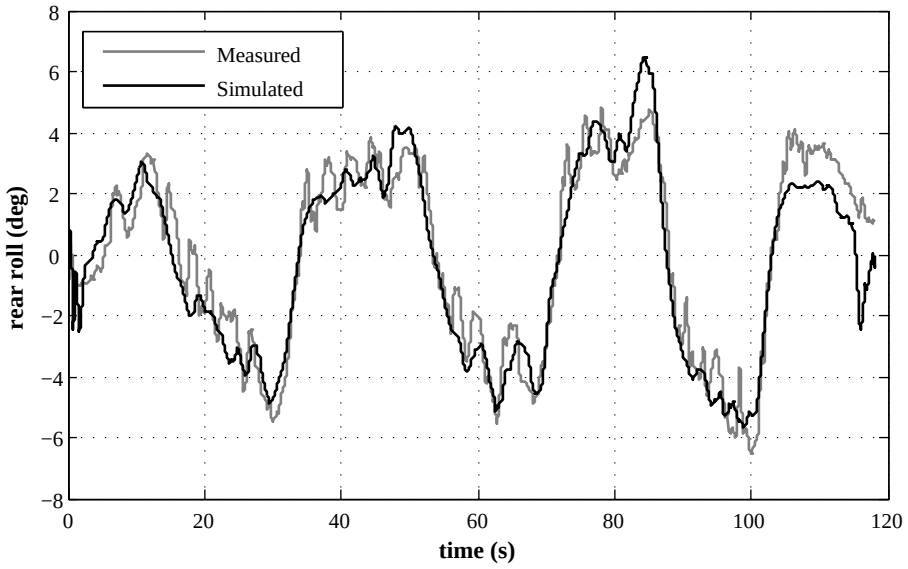

Figure 5.16: Rear module roll in a figure of 8 manoeuvre with locked cabin

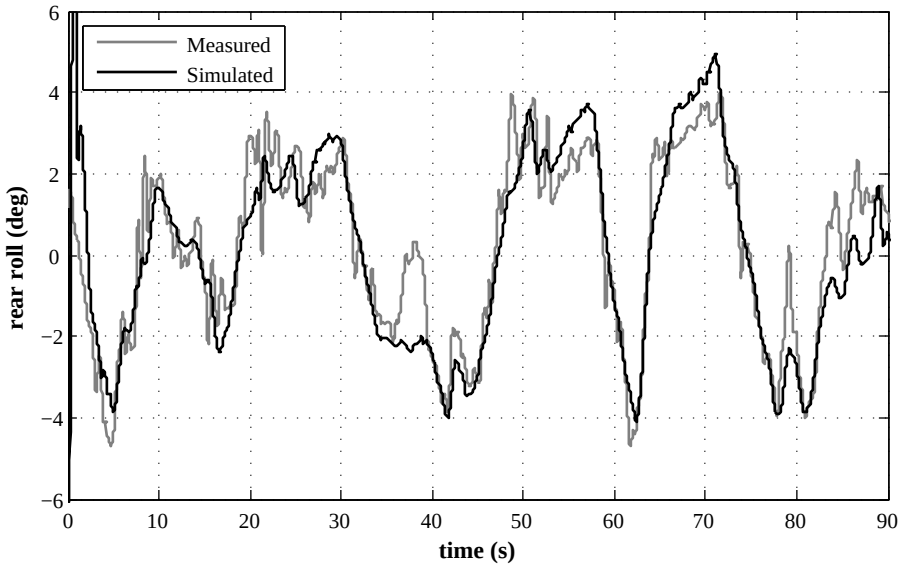

Figure 5.17: Rear roll whilst driving with tilting cabin

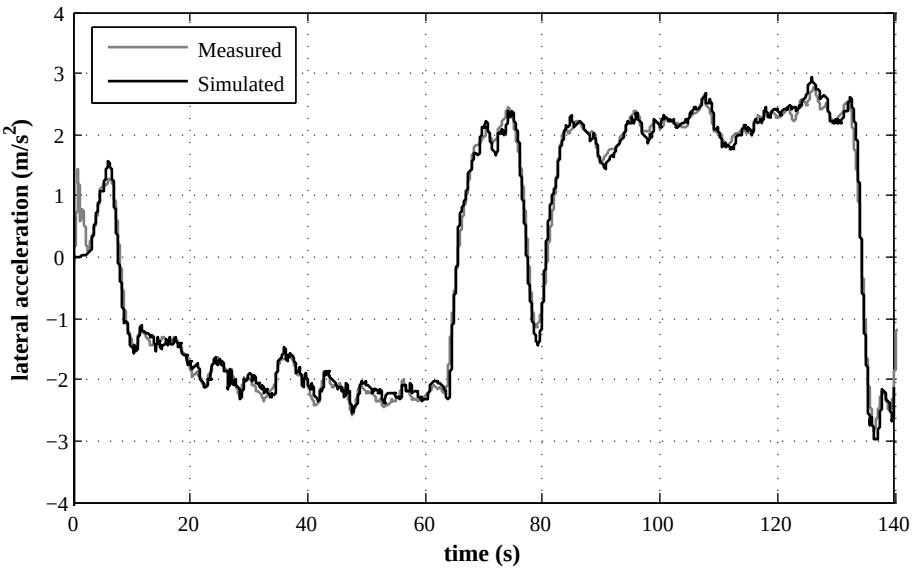

Figure 5.18: Measured and simulated steady state lateral acceleration (t = 10-60 seconds and t = 90-130 seconds)

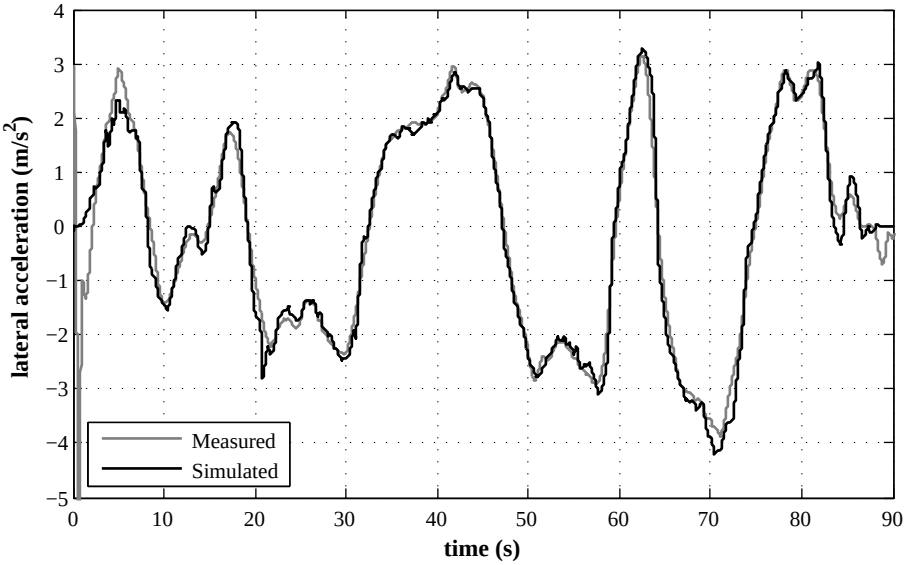

Figure 5.19: Measured and simulated lateral acceleration with moderate steering inputs

noeuvres, the model could only be validated in steady state and in quasi-steady state, where the frequency of the steering inputs remained small relative to the body roll natural frequency. Furthermore, due to limitations in the available hardware and testing facilities, higher order dynamics would have been very difficult to capture. However, within these testing conditions a good fit was established between the measured and the simulated dynamics with moderate steering inputs and with lateral accelerations of up to 4m/s^2.

Effective axle cornering characteristics were used in the model to establish rear module roll and load transfer across the rear axle. These were shown to have a good fit with the measured body roll. However, this method is only applicable at low frequencies, where effects due to damping and inertia can be neglected. In order to accurately measure transient effects and the effects of load transfer in rapid manoeuvres, the tyre load will be taken from the vertical dynamics model where the higher order dynamics have been accurately modelled. Equally, additional weight transfer resulting from the actuator forces will have significant effects in rapid transient manoeuvres and are investigated in detail in chapter 6.

It was attempted to measure the slip stiffnesses of the front and rear tyres using data from the GPS sensor, but the accuracy of the system was shown to be insufficient. If tests were repeated, it would be recommended to use a DGPS system which achieves much higher resolutions and sampling rates. This would also be useful when looking at the dynamics at higher frequencies. Unfortunately these systems are currently only available at high cost. Furthermore, it was found that the linear potentiometers on the CLEVER prototype rapidly deteriorated under current driving conditions. The use of non-contact LVDT sensors would therefore be highly recommended in further testing.

Chapter 6

Limiting Stability Conditions

This chapter looks at the limiting stability conditions that lead to roll-over of the vehicle. For the steady state limits, a two degree of freedom model will be used which includes the kinematic effects resulting from the inclination of the tilt axis. This model is used to introduce the transient state limitations using the 'reserve moment' concept, which indicates the additional roll-moment which can be applied to the rear module before all the load is transferred to the outer wheel in a cornering manoeuvre. This approach gives an insight into the vehicle stability issue but does not take into account dynamic effects. In order to account for dynamic effects and create a deeper understanding of the chain of events that leads to transient state vehicle roll-over, a typical transient state manoeuvre is investigated using the full vehicle model. The limitations of a direct tilt-control approach are discussed. In order to explore the limits of the tilting dynamics, an optimisation study is performed based on an arbitrary function to describe the tilting profile.

6.1 Steady State Analysis

Although instability of the vehicle has been primarily associated with the transient state condition, it is important that the steady state performance is satisfactory before the transient state issues can be addressed. Subjective tests have already shown this to be satisfactory at lateral accelerations of up to 6 m/s^2 [11], although performance at higher lateral accelerations has been found to be inadequate. A regular car tyre reaches its adhesion limit at approximately 10 m/s^2 lateral acceleration [36]. In order

for the vehicle to slide rather than to roll-over, it is necessary for the vehicle's steady state roll-over limit to lie beyond this point. A full steady state analysis including kinematic effects of the vehicle has not yet been performed. A two degree of freedom model will be used based on the centre of mass locations estimated in section 3.1.1. As mass transfer associated with suspension displacements is not taken into account, this somewhat optimistic analysis represents the upper performance limit that can be achieved with the vehicle in its current configuration. A sensitivity study of the key geometrical parameters will be performed in order to assess their impact on the maximum achievable lateral acceleration. In the following section the parameters relating to the cabin denoted by the subscript c, refer to the combined cabin and driver system.

6.1.1 Vehicle Maximum Lateral Acceleration

Limiting Condition Equations

It is possible to determine the maximum lateral acceleration of the vehicle in steady state by looking at a free-body diagram of the vehicle as shown in figure 6.1. Previously, the cabin has been modelled as an inverted pendulum mounted onto the rear module. In the following approach the forces acting at the front wheel and the resulting moments are taken into account.

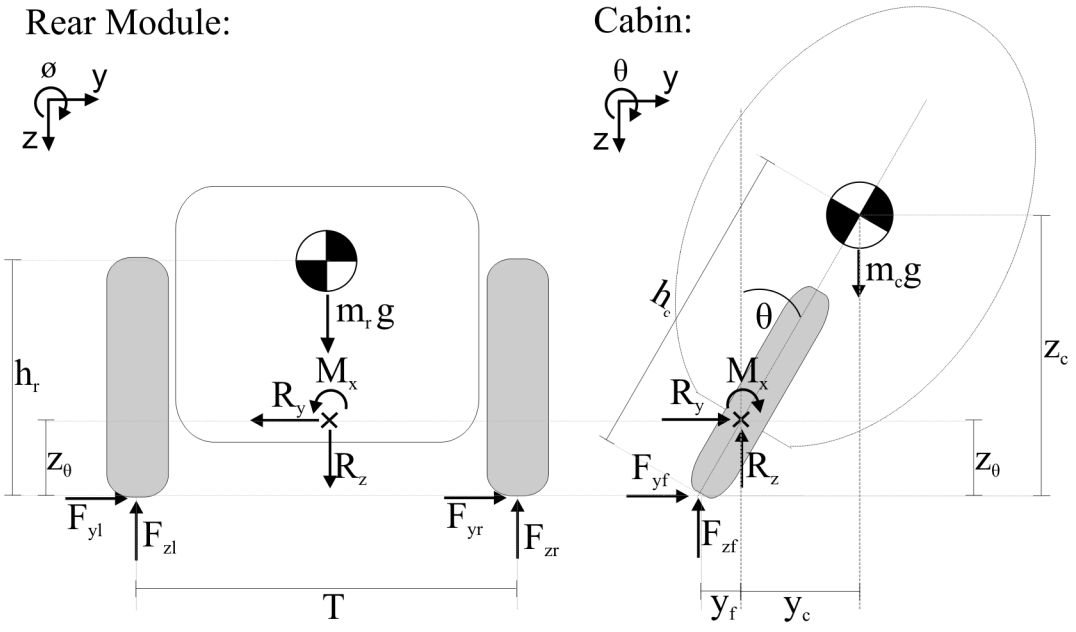

Figure 6.1: Free body diagram of cabin and rear module viewed from the rear

Taking moments about the rear module and the cabin centre of gravity results in the following equations of motion:

$$I_r\ddot{\phi} = R_y(h_r - z_\theta) + (F_{zl} - F_{zr})\frac{T}{2} - h_r(F_{yl} + F_{yr}) - M_x \tag{6.1}$$

$$I_c\ddot{\theta} = M_x + F_{zf}(y_f + y_c) + R_z y_c - F_{yf} z_c - R_y(z_c - z_\theta) \tag{6.2}$$

The forces on the cabin can be resolved to find the reactions at the tilt bearing R_y and R_z. If $\ddot{z} = 0$ and $\ddot{y} = a_y$ then:

$$R_z = m_c g - F_{zf} \tag{6.3}$$

$$R_y = m_c a_y - F_{yf} \tag{6.4}$$

If m represents the total vehicle mass $(m_c + m_r)$, the side force at the front (F_{yf}) and at the rear $(F_{yl} + F_{yr})$ are given by:

$$F_{yf} = \frac{b}{L} m a_y = F_{zf}\frac{a_y}{g} \tag{6.5}$$

$$F_{yl} + F_{yr} = \frac{a}{L} m a_y = (F_{zl} + F_{zr})\frac{a_y}{g} \tag{6.6}$$

At the limiting condition, i.e. just before the vehicle rolls over, the entire rear axle load is supported by the tyre on the outside of the turn and the tyre on the inside of the turn has zero vertical load. Assuming the vehicle is turning right, at the limiting condition the entire weight of the vehicle would be supported by the left tyre ($F_{yr} = F_{zr} = 0$). As there is no roll due to the suspension and it is assumed that the right wheel does not leave the ground, $\ddot{\phi} = 0$. Equation 6.1 can therefore be reduced to:

$$0 = R_y(h_r - z_\theta) + F_{zl}\frac{T}{2} - h_r F_{yl} - M_x \tag{6.7}$$

substituting for F_{yl}, R_y and F_{zl} and assuming the cabin is balanced ($M_x = 0$):

$$h_r \frac{a}{L}(m_c + m_r)a_y - \left(m_r \frac{b}{L} - m_c\left(1 - \frac{b}{L}\right)\right)(h_r - z_\theta)a_y - \frac{a}{L}(m_c + m_r)g\frac{T}{2} = 0 \quad (6.8)$$

Rearranging for a_y and substituting $h_{r\theta}$ for $(h_r - z_\theta)$ and m for $(m_c + m_r)$, the following expression for the maximum lateral acceleration is obtained:

$$a_y = \frac{amgT}{2a(mh_r - m_c h_{r\theta}) + 2m_r b h_{r\theta}} \quad (6.9)$$

Using values for CLEVER, a maximum lateral acceleration of 9.59 m/s^2 is obtained.

The following analysis is to consider the additional moment M_x acting about the tilt joint when the cabin is not balanced. It is then possible to take into account design limitations in the tilting range affecting the steady state stability. The additional moment resulting from the cabin being unbalanced in transient states can also be investigated.

To accurately estimate M_x it is necessary to take into account the kinematic effects resulting from the tilt axis inclination. This kinematic effect results in a lateral motion of the front wheel (discussed in section 2.2.1) as well as a pitch motion of the rear module as the cabin tilts, which in turn leads to a height reduction in the tilt bearing location. Figure 6.2 (top) shows an annotated side profile of the vehicle showing the position of the cabin centre of gravity. Figure 6.2 (middle and bottom) show a side view and top view after a positive (right as viewed from rear) rotation θ about the tilt axis.

As a result of the tilt-bearing height reduction, there will also be a shift in the position of the cabin and driver CoG. However this will be so small that it can be neglected.

After some manipulation and using small angle approximations for the tilt axis inclination ξ, the distances y_f, y_c, z_c and z_θ can be written as:

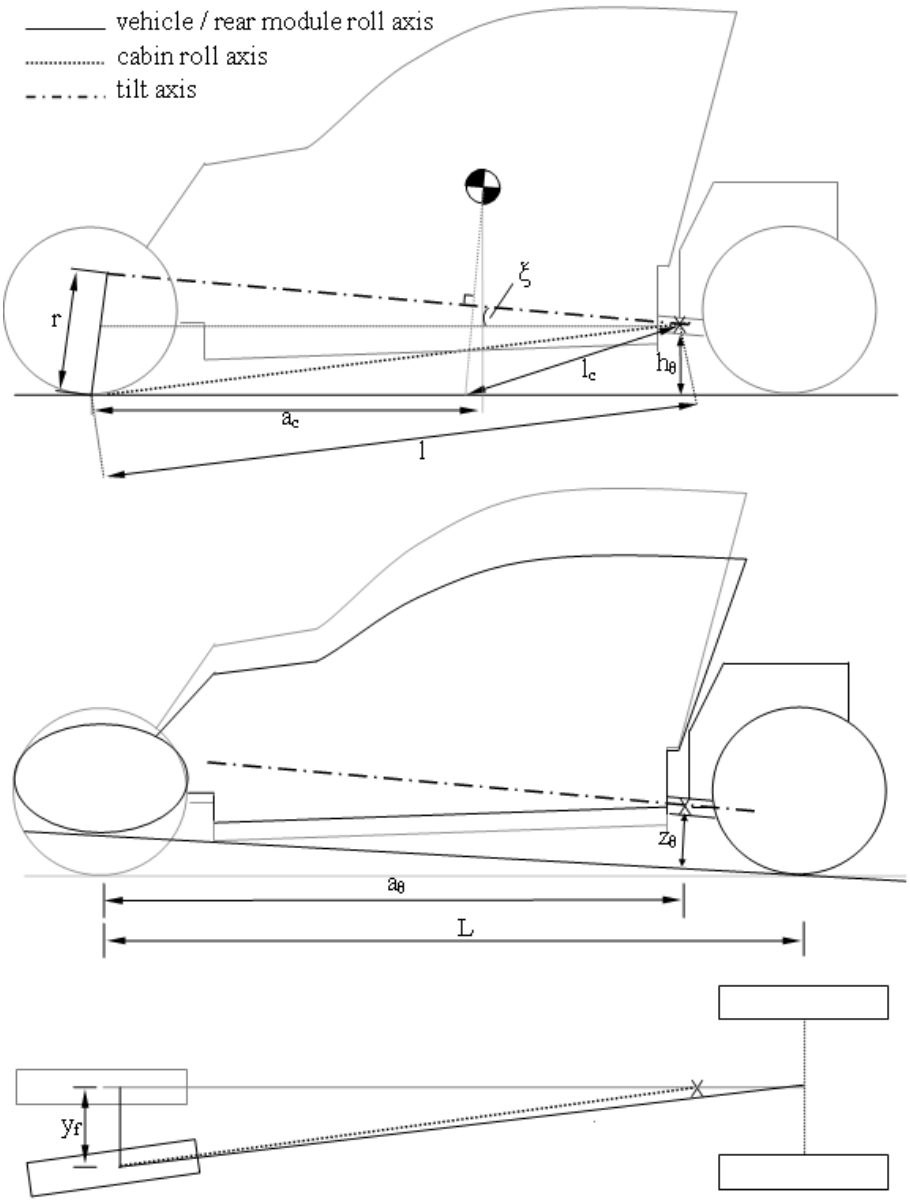

Figure 6.2: Vehicle roll axis before and after a rotation of the cabin about the tilt axis when keeping the rear module fixed

$$
\begin{aligned}
y_f &= (h_\theta + \xi l)\sin\theta && (6.10)\\
y_c &= (h_c - h_\theta - l_c\xi)\sin\theta && (6.11)\\
z_c &= \left(h_c - h_\theta\frac{a_c}{a_\theta}\right)\cos\theta + h_\theta\frac{a_c}{a_\theta} && (6.12)\\
z_\theta &= h_\theta - \frac{1}{L}(L - a_\theta)(h_\theta + \xi l)(1 - \cos\theta) && (6.13)
\end{aligned}
$$

Assigning the variables $z_{c\theta} = (z_c - z_\theta)$ and $y_{fc} = (y_f + y_c)$ we can group the a_y and g terms in equation 6.2 to give the expression:

$$M_x L = [(m_c L + bm)z_{c\theta} + bmz_c]a_y - [bmy_{fc} + (m_c L - bm)y_c]g + LI_c\ddot{\theta} \qquad (6.14)$$

Combining equations 6.14 and 6.7 by substituting for M_x and rearranging terms to obtain an expression for the vehicle's maximum lateral acceleration gives:

$$a_y = \frac{(amT + 2bmy_{fc} + 2(m_c L - bm)y_c)g - 2LI_c\ddot{\theta}}{2a(mh_r - m_c h_{r\theta}) + 2m_r bh_{r\theta} + 2(m_c L + bm)z_{c\theta} + 2bmz_c} \qquad (6.15)$$

Limiting the tilting range to 45°, setting $\ddot{\theta}$ to zero and entering the values corresponding to the CLEVER set-up into equation 6.15 we obtain a maximum steady state lateral acceleration 7.4 m/s^2. It should be noted that this is the theoretical maximum without any suspension roll. The value is considerably less than the 9.59 m/s^2 obtained when assuming the cabin remains balanced.

Parameter Sensitivity Study

The above equations can be used to investigate effects of changes in the cabin set-up on the steady state performance. The most important parameters affecting the maximum steady state lateral acceleration are the tilting range of the cabin and the rear module track width. The variation in the maximum lateral acceleration for a range of values in these key parameters are shown in figure 6.3.

It can be seen that to achieve a maximum lateral acceleration of 10 m/s^2 in the current

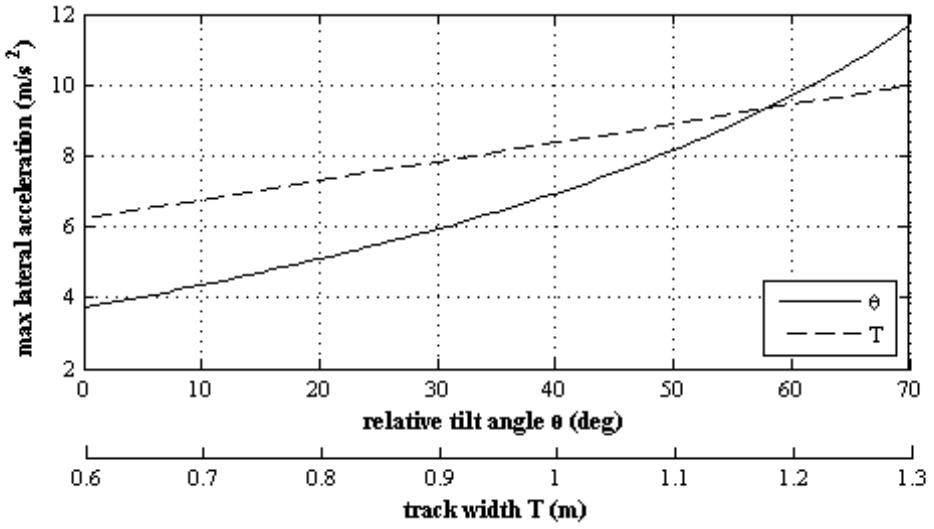

Figure 6.3: Effect of relative tilt angle and track width on maximum steady state lateral acceleration

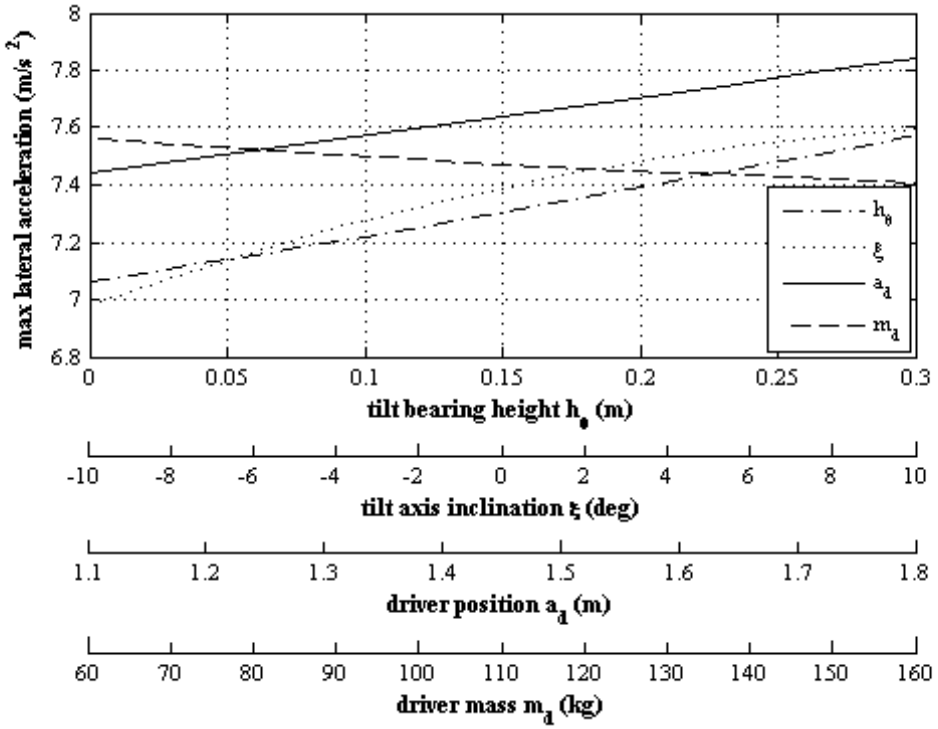

Figure 6.4: Effect of tilt bearing height, tilt axis inclination, driver position and driver mass on maximum steady state lateral acceleration

set-up, a tilting range greater than ± 60 °would be required or a track width of 1.3m (current track width = 0.84m). It is interesting to note that the track width of the Vandenbrink CARVER of 1.14m is equally below this value (assuming a similar tilting range and mass distribution).

The effects of the driver location a_d and mass m_d as well as the tilt bearing height h_θ and tilt axis inclination ξ are shown in figure 6.4. One of the effects that stands out is the small significance of the driver mass. This is due to the fact that the added cabin moment at maximum lateral acceleration is offset by the additional load on the rear wheels. The maximum lateral acceleration is increased as the driver position a_d is shifted to the rear as this results in additional load onto the rear tyres. Another surprising result is that $a_{y,max}$ increases with the tilt bearing height h_θ, whereas it would be expected to decrease. This result is misleading as the tilt-axis inclination ξ is kept constant in the calculation. To obtain the same handling characteristics (and lateral motion of the front wheel), ξ should however be increased as h_θ is lowered. As can be seen, a positive tilt axis inclination shifts the front wheel away from the turning radius which helps to prevent rollover. However, the reduction in $a_{y,max}$ due to the raised tilt axis and tilt axis inclination is not as great as initially anticipated.

6.1.2 Moment Reserve

Under steady state lateral acceleration there is a load transfer onto the outer wheel. If we take the cabin as being balanced in steady state, the moment about the rear module CoG resulting from the lateral force is given by:

$$M_r = (F_{yl} + F_{yr})h_r - R_y h_{r\theta} \tag{6.16}$$

Using the previously derived expressions for F_{yl}, F_{yr} and R_y, this can be rewritten as:

$$M_r = (amh_r - (m_c L - bm)h_{r\theta})\frac{1}{L}a_y \tag{6.17}$$

Once the cabin reaches its tilting limit and can no longer be balanced (at 5.7m/s^2), there will be an additional moment M_x from the cabin given in equation 6.14. The load transfer ΔF_z across the rear axle is then given by:

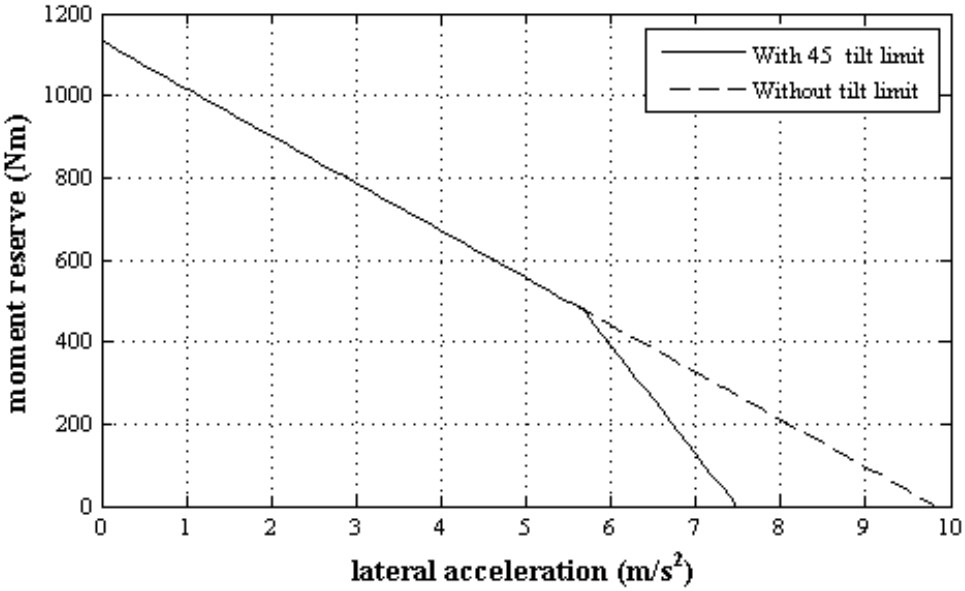

Figure 6.5: Moment reserve against lateral acceleration

$$\Delta F_z = \frac{M_r + M_x}{T} \tag{6.18}$$

The maximum allowable load transfer $\Delta F_{z,max}$ is equivalent to half the weight on the rear axle. Therefore, the additional moment that can be applied about the tilt bearing before reaching the maximum weight transfer is given by:

$$M_{res} = (\Delta F_{z,max} - \Delta F_z)T \tag{6.19}$$

A graph of the moment reserve against lateral acceleration is shown in figure 6.5.

Looking at figure 6.5 it can be observed that the moment reserve rapidly drops off once the cabin has reached its maximum tilting range at a lateral acceleration of 5.7m/s^2. If the maximum steady state lateral acceleration of 7.4 m/s^2 is reached, there is no allowance for any additional moment. Operating the vehicle close to the steady state limit can therefore easily result in roll-over.

It is possible to plot the moment reserve against lateral acceleration for the entire tilting range of the vehicle, as shown in figure 6.6. This gives an initial indication of

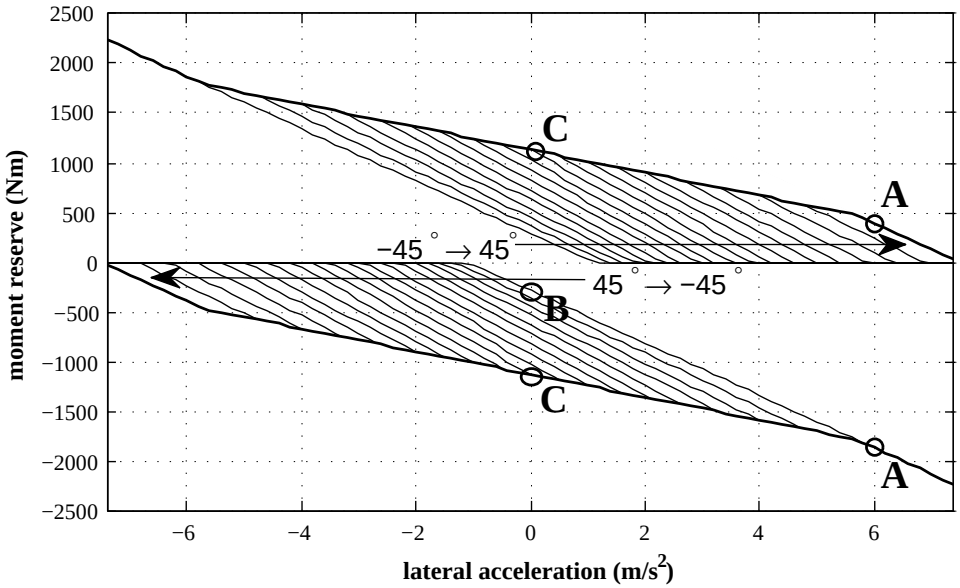

Figure 6.6: Moment reserve against lateral acceleration

the torque that can be applied by the actuators before risking vehicle roll-over, and illustrates the problem leading to roll-over in transient state manoeuvres.

To explain the significance of figure 6.6 relating to the transient state instability, an imaginary scenario will be used where the vehicle exits a steady state corner with a lateral acceleration of 6 m/s^2 to return to straight line driving at 0 m/s^2. The bold line in figure 6.6 represents the condition where the cabin is balanced such that no moment is applied to the rear module up to ± 45°. If the vehicle is travelling in steady state with a lateral acceleration of 6 m/s^2, the cabin will be tilted at 45° and there will be approximately 400 Nm moment reserve in one direction (to increase the tilt beyond 45°) and -1900 Nm in the other (to reduce the tilt towards zero), denoted by A. If a step steer demand was then made to return to straight line driving (denoted by C), i.e. 0 m/s^2 lateral acceleration, only a small moment reserve would be available before the vehicle would roll over (between B and C). Assuming that the step change in lateral acceleration could occur instantly, the cabin would still be tilted at 45° while the vehicle has 0 m/s^2 lateral acceleration, as denoted by B. The available moment to tilt the cabin back in the upright position at this point is only around -250 Nm. Clearly, the greater the step change in lateral acceleration, the smaller the moment reserve available to achieve the desired tilt angle. Of course, in real life, it is impossible to make an instantaneous step and the lateral acceleration would require a certain time to build up. However, it does illustrate how a transient manoeuvre where a rapid change in

lateral acceleration is demanded could easily lead to a roll-over situation. Furthermore, a demand such as the one illustrated would lead to a large tilt angle error, resulting in a high actuator torque, which would result in the overall rear module moment surpassing the moment reserve, ultimately leading to the roll-over of the vehicle.

6.2 Transient State Limitations

So far the vehicle's limiting conditions have been described purely from equations of static equilibrium. Transient state rollover was previously shown to occur when the actuator torque exceeds the 'moment reserve'. This is a simple method of illustrating the limitations of a direct tilt-control approach. The highest potential for roll-over occurs in dynamic situations. To illustrate the conditions which lead to roll-over in transient state, the full vehicle model will therefore be used. It should also be noted that for roll-over to occur, the centre of gravity of the vehicle would first have to be shifted across the roll-over axis, which lies between the rear wheel on the outside of the turn and the front wheel. However, for the purpose of this study, the roll-over point will be taken as the point where the inner wheel load becomes zero.

Manoeuvres in which a rapid steer input is made can result in a high torque demand as the error between actual and the demand tilt angle becomes large. The torque demand becomes even greater when the cabin is already tilted past the balancing point (i.e. 'over-lean' is applied) or following an input in the opposite direction where the angular momentum of the cabin has to be overcome.

6.2.1 Steering Rate

Although a step input demand in the steering would result in a large tilt angle error, an instantaneous change in the steering angle would be impossible in practice. To gauge the maximum steering rate that could be encountered, a step input at low vehicle speed with the hydraulics switched off was performed. This could be taken as a benchmark for the type of steering input that might result from a severe avoidance manoeuvre. The shape of this input could be represented closely by a ramp input followed by a first order lag. This is shown in figure 6.7. The maximum steering rate of this steering input is approximately 400°/s, and will be taken as the maximum possible steering rate that could be encountered in an avoidance manoeuvre.

6.2.2 High Risk Manoeuvres

A number of dynamic manoeuvres that can lead to large and rapid steer input demands are listed below:

- A figure of 8 manoeuvre
- A lane change manoeuvre
- An avoidance manoeuvre

In fact, these three manoeuvres are very similar and differ only in the steering rate applied and the time between steering inputs. In a figure of eight manoeuvre, the driver enters a steady state circular path and after almost completing a full circle, enters a steady state circular path in the other direction. The transient state connecting the two steady state circles presents the problem with the current control strategy. A lane change manoeuvre requires a similar steering input to that of a figure of 8, with the exception that the steer inputs are closer together and the steer angle is returned to zero. An avoidance manoeuvre can be regarded as a rapid lane change manoeuvre, and probably represents one of the most demanding scenarios for any vehicle. It is easiest to follow the chain of events in a figure of 8 manoeuvre and observe the corresponding

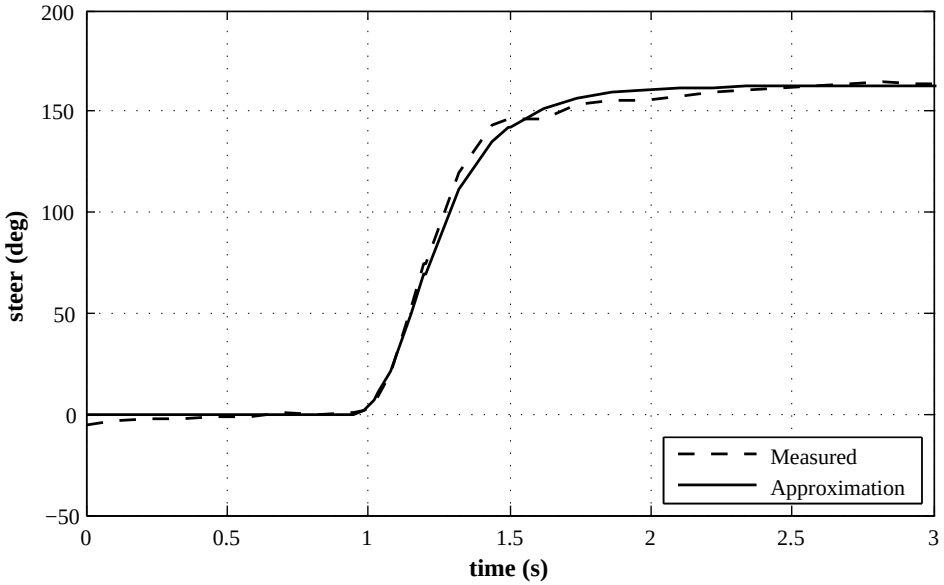

Figure 6.7: Measured steer input and first order lag fit

system response. This scenario will therefore be used to illustrate the chain of events that can lead to the transient state roll-over of the vehicle. Figure 6.8 shows the driving path for a figure of 8 manoeuvre, where the section A represents the entry into the manoeuvre and sections B through E denote the transient and steady state sections for the first half of the manoeuvre. The second half of the manoeuvre requires the same steering inputs, but in the opposite direction and is therefore not labelled.

Figure 6.9 shows the steering input required for this manoeuvre and the simulated lateral acceleration, tilt angle error and inner wheel load of the full vehicle model. It can be seen that the transient section (section D), where the cabin is required to tilt from one side to the other results in a large tilt angle error (up to 30°). Due to the steady state sections (sections C and E) in the figure of 8 manoeuvre, the transient state steer inputs are made with a few seconds in between. In a lane change manoeuvre or avoidance manoeuvre similar rapid steering inputs would be made much closer together.

It can be seen in figure 6.9 that at the end of the steering input (at t = 6s), the lateral acceleration has already reached its steady state value and the tilt error is also nearly at its maximum. There will therefore be a large moment acting on the rear module as the actuators tilt the cabin towards the demand angle. This illustrates a fundamental issue with the direct tilt control method. If the system gain and therefore the torque applied to the rear module is increased, a higher tilting acceleration of the cabin is achieved. As a result, the tilt angle will remain closer to the demand angle which in turn would reduce the tilt error. However, the large torque would initially create a greater load transfer to the outer wheel, increasing the likelihood of roll-over. On the other hand, if the applied torque is reduced, this would reduce the load transfer to the outer wheel, but as the tilt angle error would increase, the likelihood of roll-over due to imbalance of the cabin would also become greater.

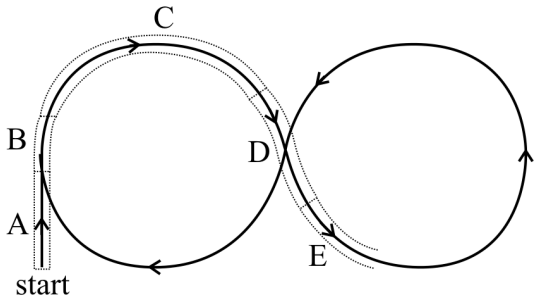

Figure 6.8: Figure of 8 manoeuvre

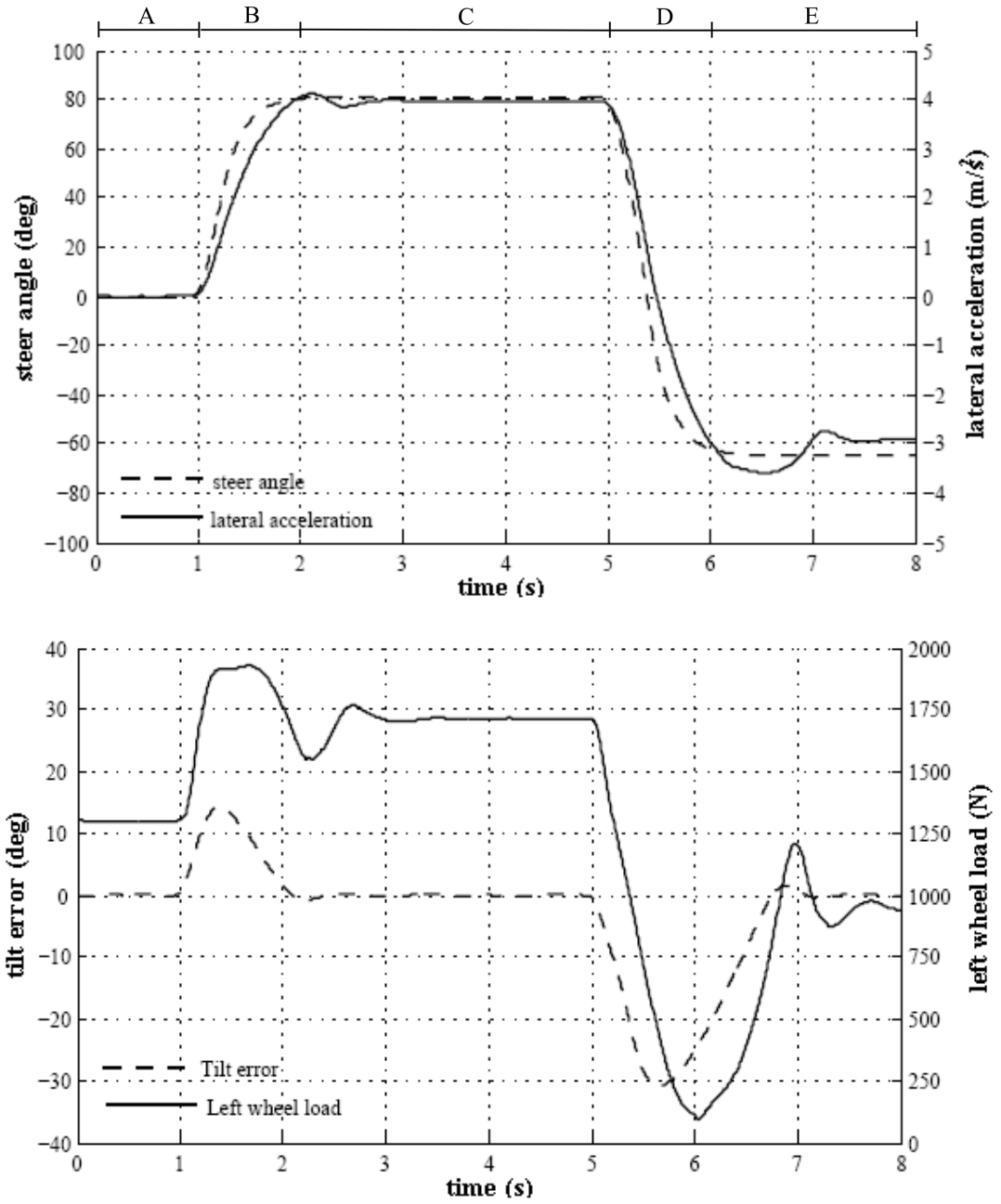

Figure 6.9: Simulated steer input and lateral acceleration response (a) and resultant tilt displacement error and left wheel load (b) for entering and exciting a steady state corner

This leads to the question of whether an optimum tilting profile exists where the motion of the cabin and the build up of lateral acceleration are synchronised in such a way that the steady state demand can be reached as rapidly as possible without the vehicle rolling over. A study was therefore conducted by assuming a profile for the lateral acceleration and tilt acceleration and optimising it to maximise the lateral velocity of the vehicle without roll-over.

6.3 Lateral Dynamics Optimisation

6.3.1 Optimisation Objectives

Looking at the free body diagram of the cabin and rear module shown in figure 6.1, it can be clearly seen that the roll moment resulting from the vehicle's lateral acceleration and that of the actuators tilting the cabin into the turn both act in the same direction. As there is a maximum roll moment that can be applied before the vehicle rolls out of the corner, this leads to the question of how to allocate the available moment. When the vehicle is tilted, it is possible to apply a greater lateral acceleration without roll-over than would be possible with the vehicle in the upright position. However, whilst the cabin is being tilted, the lateral acceleration allowance is reduced. The objective of this study is to find the optimum tilting profile that will maximise the lateral velocity of the vehicle without roll-over. At one end of the spectrum, the vehicle would only start tilting once a desired lateral acceleration has been reached. At the other end of the spectrum the vehicle would only generate lateral force once the cabin had reached the necessary tilt angle. Naturally, the optimum solution is likely to lie between these two extremes.

6.3.2 Lateral Acceleration Profile

A candidate tilting profile has been chosen, the parameters of which will be optimised. Figure 6.10 shows the experimental lateral acceleration build up of the vehicle as a result of a sudden steer input. In order to avoid roll-over, the sum of the lateral acceleration and the tilting acceleration cannot exceed a certain maximum value at any instant. As the lateral acceleration increases the tilting acceleration will usually need to reduce, and so an exponential decay is chosen as a candidate function for the tilting acceleration, as shown in equation 6.20.

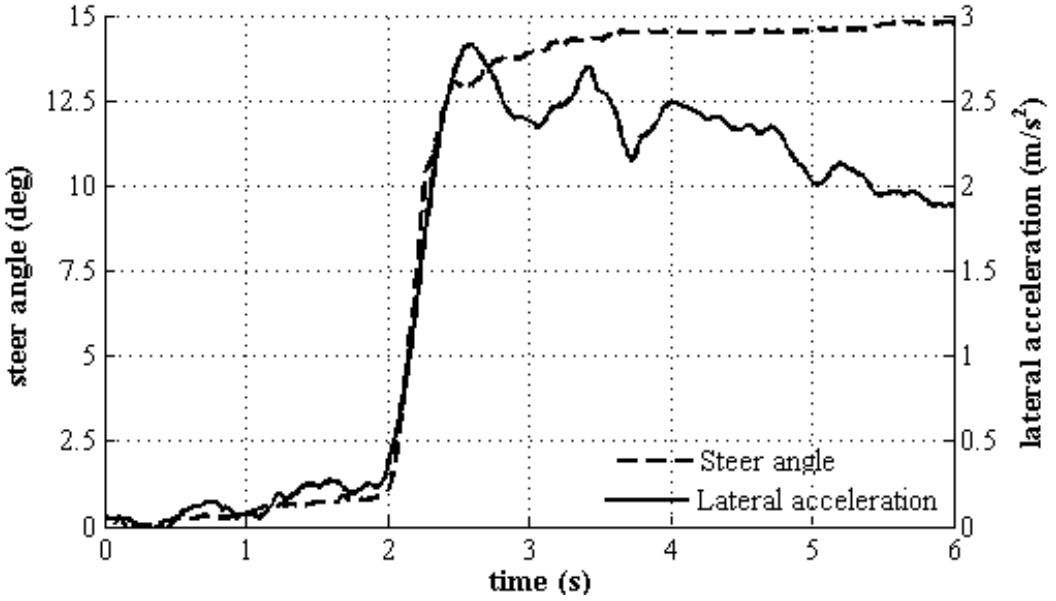

Figure 6.10: Measured lateral acceleration step input response

$$\ddot{\theta} = Ke^{\frac{-t}{\tau}} \tag{6.20}$$

The maximum roll moment that can be applied is equivalent to K. If we integrate equation 6.20 twice and assume the initial condition $\dot{y_c} = y_c = 0$, we obtain the following expression for the tilt angle θ:

$$\theta = \tau^2 K e^{\frac{-t}{\tau}} + \tau K t - \tau^2 K \tag{6.21}$$

6.3.3 System Equation

Substituting the expressions for $\ddot{\theta}$ and θ into equation 6.15 and integrating with respect to t, the lateral velocity is represented by the integral shown in equation 6.22:

$$\dot{y} = \int_0^{t_v} \frac{(amT + 2bmy_{fcd} + 2(m_f L - b_m)y_{cd})g - 2LI_{cd,z}\ddot{\theta}}{2a(mh_r - m_f h_{r\theta}) + 2m_r b h_{r\theta} + 2(m_f l + bm)z_{cd\theta} + 2bmz_{cd}} dt \tag{6.22}$$

The parameter values used are shown in table 6.1.

Symbol	Description	Value
a	Dist. CoG to Front	1.60m
a_c	See Figure 6.2	1.14m
a_θ	See Figure 6.2	1.95m
b	Dist. CoG to Rear	0.80m
h_c	Cabin Height	0.59m
h_r	Rear Module Height	0.54m
h_θ	Tilt Joint Height	0.271m
l	See Figure 6.2	1.97m
l_c	See Figure 6.2	0.904m
m_c	Cabin Mass	250kg
m_r	Rear Module Mass	162kg
I_c	Cabin Inertia	100 kgm^2
K	Profile Parameter	5.66
L	Wheelbase	2.40m
T	Wheeltrack	0.84m
ξ	Tilt Axis Angle	5°

Table 6.1: Vehicle system parameters

6.3.4 Results

Straight Line Driving

By plotting the lateral velocity against the time constant τ, it is possible to determine the value which maximises the lateral velocity after any given period of time.

Figure 6.11 displays the change in lateral velocity against τ for the time period t_v = 0.1 to 1.0 seconds. The circles on each line of constant time denote the value of τ for which the vehicle's lateral velocity is a maximum. These results show that up to a time of $t_v = 0.4$s the best strategy is to keep the cabin in the upright position, i.e. not to tilt at all. Furthermore, it can be seen in figure 6.11 that the value of τ reaches an optimum value of 0.53 at t = 0.67seconds. It can be seen that there is an optimal tilting profile to achieve the greatest lateral velocity past 0.67 seconds. Therefore if the vehicle were tilted any faster, i.e. using a larger time constant (to maintain tilting acceleration for longer), this would in fact be counterproductive. Figure 6.12 shows the lateral acceleration profile for various values of τ. The discontinuities for $\tau = 0.53$ and $\tau = 0.8$ are associated with the physical limitation of 45°max tilt.

The objective of this study was to find what profile maximises the lateral velocity of the vehicle without rollover after a certain period of time, i.e. the greatest area

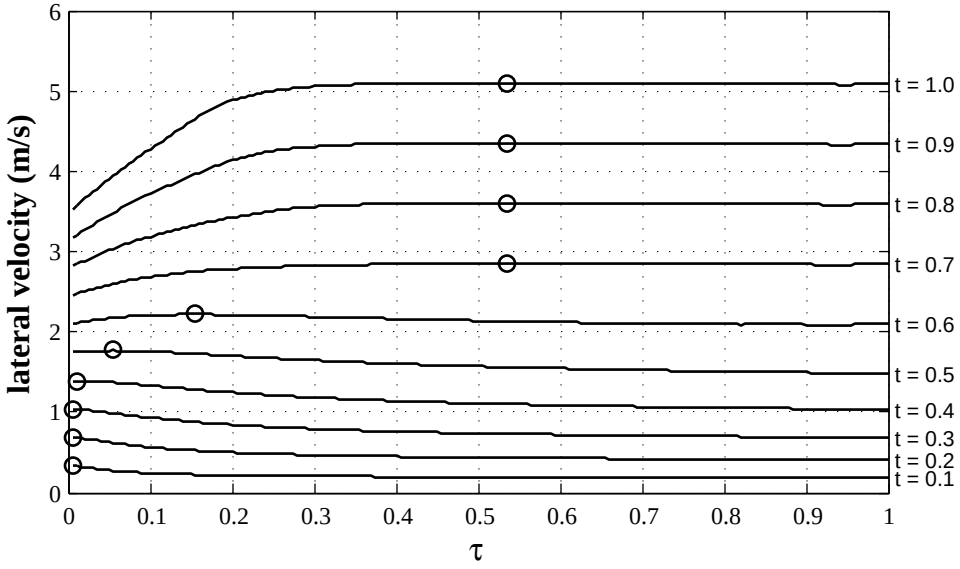

Figure 6.11: Lateral velocity against τ for $t_v = 0.1$ to 1s

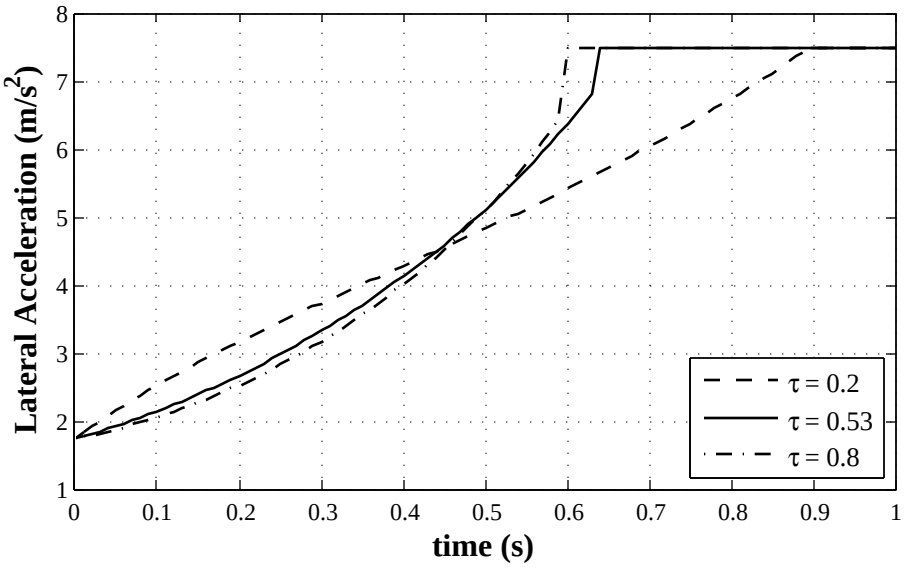

Figure 6.12: Lateral acceleration against time for different values of τ

enclosed by the lines in Figure 6.12. For the ideal value of τ= 0.53, the build up of lateral acceleration can be seen to be fairly gradual. This bodes well from a drivability perspective, although it will be necessary to investigate this aspect further.

Variation of Initial Conditions

The tilting profiles shown previously apply to an initial straight line driving condition with zero lateral acceleration and tilt angle. The same procedure can be repeated for all combinations of initial tilting angle and lateral acceleration of the vehicle. This would represent exiting a steady state manoeuvre and demanding the maximum vehicle lateral acceleration. A value of τ for any initial driving condition to maximise the lateral velocity without roll-over after a specific time interval can then be obtained.

The value of K is dependent on the allowable moment that can be applied without the vehicle rolling over. This is dependent on the current lateral acceleration and tilt angle of the vehicle. As was shown previously (figure 6.6), the moment reserve against lateral acceleration can be calculated over the entire tilting range of the cabin (-45° to +45°). The maximum tilt acceleration and K value is then given by:

$$K = \ddot{\theta}_{max} = \frac{M_{x,max}}{I_c} \tag{6.23}$$

It is now possible to calculate an optimal value for τ with each initial condition for a range of time intervals. As shown in figure 6.11, this converges to a maximum as time increases. Figure 6.13 displays the variation in the optimal value of τ after a period of t_v = 1 second. At zero lateral acceleration and tilt angle we have the condition that was previously discussed, resulting in an optimal τ value of 0.53. The area where $\tau = 0$ represents the conditions that cannot be achieved. For visual purposes the maximum τ value was restricted to 0.6. In actual fact it was found that τ grows larger as the initial conditions get further from the demand conditions, i.e. instead of a plateau at $\tau = 0.6$, these values would keep rising. This indicates that at these conditions a high tilt acceleration is required rather than building up lateral acceleration quickly.

The outer edge of the plateau (A), past which τ drops to zero, represents the worst case scenario where the τ value would reach a maximum. The grey edge on the opposite side (B) going from 0 to 45° represents the initial conditions that would be encountered in a balanced steady state corner. It can be seen that the optimal value of τ remains

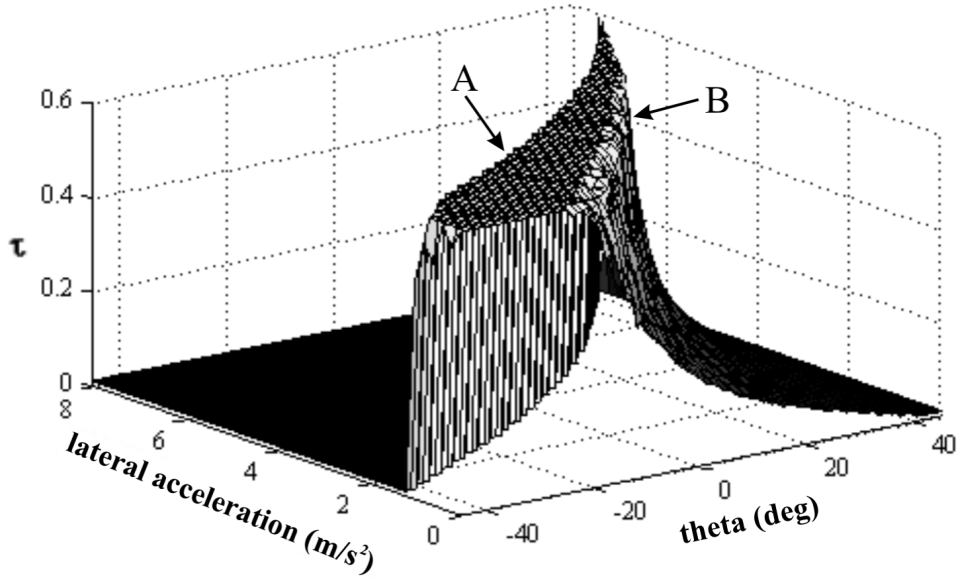

Figure 6.13: Optimised τ value for a 1 second interval

approximately constant in this instance. The further a point is located from this line, the smaller the likelihood that the situation will be encountered. For example the point $[a_y, \theta] = [0.5, -45]$ represents the unlikely steady state situation where the vehicle has a lateral acceleration towards the right, but is tilted in the opposite direction. However, this would be a possible scenario in a transient situation. For example, when a driver exits a steady state turn in one direction and demands the maximum lateral acceleration in the other, with the current control strategy, a steer input is made generating a lateral acceleration. As can be seen in Figure 6.13, the ideal approach would be to tilt the cabin before the lateral acceleration builds up. Using a new control approach consistent with the profile discussed, the vehicle would be prevented from rolling over. However, as the vehicle tilts towards the balanced angle, the available tilt acceleration could be increased, which is impossible due to the nature of the chosen exponential profile. This can be illustrated using the resultant time response for the vehicle tilt and lateral acceleration for an initial condition of $\theta = -45^\circ$ and $a_y = 0.5\text{m/s}^2$ and $\tau = 1$, as shown in figure 6.14. Because the K value (equation 6.23) under these conditions is small, the tilt acceleration and hence lateral acceleration remain small even after 1 second. An ideal profile is likely to be one in which the tilt acceleration initially increases with time.

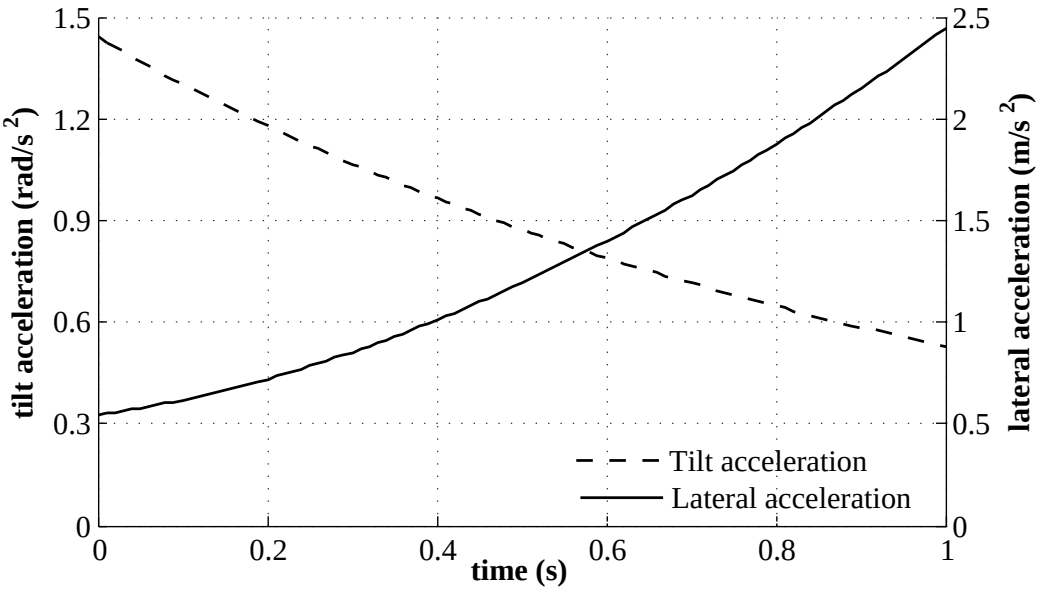

Figure 6.14: Tilt and lateral acceleration for an initial condition of θ = -45° and a_y = 0.5m/s^2 and $\tau = 1$

6.4 Concluding Remarks

Using a simple 2DoF model with cabin kinematics to model the roll dynamics of the cabin and rear module it was possible to investigate the steady state stability of the vehicle and the effects of key parameters on the maximum steady state lateral acceleration. It was shown that in its current configuration, the vehicle would be unable to reach a 10 m/s^2 steady state lateral acceleration and would therefore roll over before reaching the adhesion limit of the tyres. The two key parameters that can be increased to reach a higher steady state lateral acceleration are the tilting range of the cabin and the rear module track width.

The transient state limitations were introduced using the 'moment reserve' concept based on the 2DoF model. By tilting the cabin to the desired angle, an additional moment acts on the rear module which results in a load transfer from the wheel on the inside of the turn to the outside wheel. The moment reserve in steady state depends on the tilt angle of the cabin and the vehicle lateral acceleration. To illustrate the circumstances which can lead to transient state roll-over of the vehicle, the full vehicle model was used to show the inner rear wheel load approaching zero in a figure of 8 manoeuvre. The compromise of system response and stability was discussed and led to an optimisation study to find an ideal tilting profile.

The optimisation study has shown that an ideal tilting profile which maximises the lateral velocity of a direct-tilt-controlled vehicle without roll-over can be found for steady state initial conditions, but would sometimes perform inadequately in more complex manoeuvres. The study was based on an arbitrary function in order to illustrate the effect of different tilting dynamics. It has become clear that in order to optimise the lateral dynamics, independent control of the tilting and lateral acceleration is required. To achieve this, the direct link between the driver input at the steering wheel and the front wheel steering angle must be broken. In other words, the new control strategy needs to be a combination of direct tilt control (DTC) and steer tilt control (STC). This should allow the vehicle manoeuvrability to be maximised without exceeding the limits of stability.

Chapter 7

Controller Design Study

In the previous chapter, it was shown that in order to optimise the lateral dynamics, it is necessary to have control over the build up of lateral acceleration. Furthermore, in order to prevent roll-over it is necessary that the moment acting on the rear module remains within the calculated 'reserve moment' which describes the maximum additional moment that can be applied to the rear module before the inner wheel load reaches zero. These conditions can be met if the front steering wheel can be controlled independently of the driver input.

For the design and optimisation of the new control system, a linear model of the vehicle system is created and validated against the non-linear multi-body model. This allows a frequency domain analysis of the current system which can be used as a benchmark for the performance of the new control system. The current controller implemented in CLEVER creates an estimate of the steady state lateral acceleration based on the driver steer input and the vehicle speed. Transient dynamics, which have been shown to lead to roll-over of the vehicle, are therefore not taken into account in the original control method. A 2Hz low-pass filter was introduce in order to reduce the actuator moment. This was determined through subjective testing as the best compromise between tilting response and transient state stability, as described by Drew [35]:

" Both the proportional gain and the cut-off frequency of the software filter are significant factors contributing to the transient tilt response. Higher gains and higher cut-off frequencies allow for a fast tilt response, but they also increase the effective moment that can be applied between the base and the tilting cabin, such that roll-over is possible when the vehicle is steered aggressively. Lower frequencies prevent this from

happening, but provide poorer response in non-aggressive manoeuvres. It was shown that when designing a direct tilt controlled three-wheeled tilting vehicle with the arrangement and physical characteristics used in CLEVER, safe handling can only be achieved at the expense of a fast tilt response. ”

The linear model confirms a peak in the lateral acceleration and load transfer response close to 2Hz, giving quantitative justification for the low-pass filter. However, as shown in the previous chapter, these measures are insufficient to prevent transient-state roll-over. A new controller is therefore proposed which combines steer and tilt control to improve the lateral dynamics response and reduce the moments acting on the rear module, significantly decreasing the risk of roll-over across the frequency range.

7.1 Proposed Controller

It was shown in the previous chapter that for an optimised response in the lateral dynamics of the vehicle, independent control of the lateral acceleration through active steer is necessary. This can be achieved by cutting the direct link between the driver steering input and the steering angle at the front wheel. Instead, the driver steering input can be regarded as a lateral acceleration demand, with a controller regulating the tilt angle demand and the steer angle of the front wheel. The current controller uses the steer angle and speed to estimate the steady state lateral acceleration and calculates the required tilt angle accordingly. Transient state dynamics are therefore not taken into account. Taking the driver steer input as a lateral acceleration demand can therefore be regarded as more appropriate, as steady state conditions will not be achieved at the time the steering input is made.

In the previous chapter, it was shown that in the event of a large tilt angle error, the emphasis is on reaching the desired tilt angle rather than increasing the lateral acceleration. Using a negative gain feedback between the tilt-error and the steer input, as shown in figure 7.1, would reduce the amount of steering at the front wheel proportional to the tilt error. This therefore seems to be a reasonable first approach for an improved control method. The gain will be optimised and the new system response will be compared to the current load transfer and lateral acceleration response. It is anticipated that the optimised gain will lead to some counter-steer under certain circumstances in order to reach the required tilt angle more rapidly.

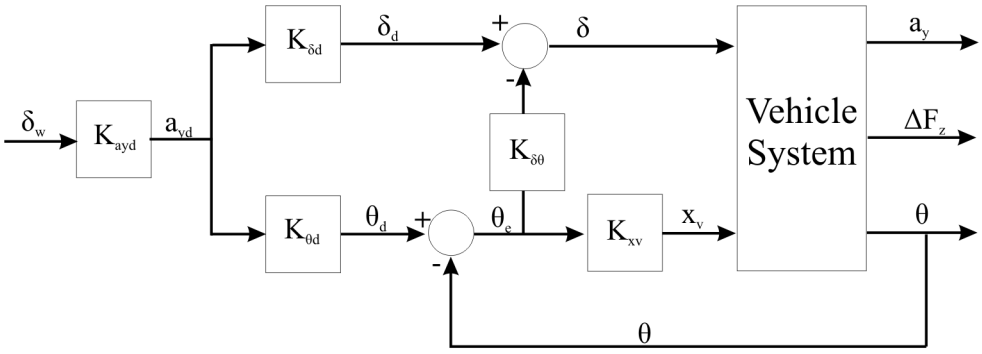

Figure 7.1: Block diagram for proposed control system

With the steering gain $K_{\delta\theta}$ set to zero, the controller is analogous to the original set-up. The lateral acceleration demand a_{yd} is equivalent to the lateral acceleration estimate of the original controller:

$$a_{yd} = \frac{\delta_w R_w V^2}{L} \tag{7.1}$$

where δ_w is the driver input at the steering wheel, R_w is the steering ratio, L is the wheel-base and V is the vehicle forward velocity. Based on the same principle, the steering demand angle δ_d and tilt demand angle θ_d are given by:

$$\delta_d = \frac{a_{yd} L}{V^2} \qquad \theta_d = K_\theta \frac{a_{yd}}{g} \tag{7.2}$$

where K_θ (=1.2) is the gain that is applied to compensate for the raised tilt axis.

7.2 System Linearisation

In order to design a new control approach and assess it against the original controller, a linearised model of the vehicle systems is developed. This allows a quantitative comparison of the old and new system performance in the frequency domain. The two variables that can be controlled are the front wheel steer and cabin tilt angle. The parameters that affect the handling and stability of the vehicle and that need to

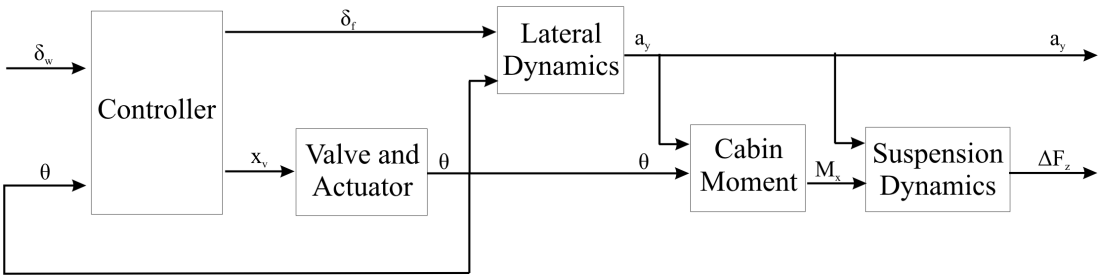

Figure 7.2: Schematic diagram showing individual blocks required for the linearisation of the vehicle system

be controlled are the vehicle lateral acceleration and the load transfer across the rear axle. Therefore a system of transfer functions will be derived to relate the steer and tilt angle demand to the vehicle lateral acceleration and rear axle load transfer. The linearisation process will be split up in order to obtain individual linear models for the vehicle's lateral dynamics (section 7.2.1), kinematics and resultant cabin moment (section 7.2.2), suspension dynamics (section 7.2.3) and dynamics of the valve and actuator system (section 7.2.4), as represented in the schematic diagram shown in figure 7.2. These will then be combined as single transfer functions relating the input to the output parameters. The system performance will be analysed over the range 0.01 - 10 Hz, although the principal frequencies of interest are regarded as 0.1 - 2Hz as this encompasses frequencies encountered at the driver/system interface.

7.2.1 Lateral Motion Dynamics

Referring to the equations described in chapter 5, the lateral motion of the vehicle can be described using the following linearised equations:

$$m(\dot{v} + Vr) = C_{\alpha f}\left(\delta_f - \frac{v + ar}{V}\right) + C_{\theta f}\theta + 2C_{\alpha r}\left(K_{\delta r}\theta - \frac{v - br}{V}\right) \tag{7.3}$$

$$I_z\dot{r} = aC_{\alpha f}\left(\delta_f - \frac{v + ar}{V}\right) + aC_{\theta f}\theta - 2bC_{\alpha r}\left(K_{\delta r}\theta - \frac{v - br}{V}\right) \tag{7.4}$$

These can be written in state-space notation with the state vector x and input vector u:

$$x = \begin{bmatrix} v \\ r \end{bmatrix} \qquad u = \begin{bmatrix} \delta_f \\ \theta \end{bmatrix} \tag{7.5}$$

V is the forward velocity about which the system is linearised. The output variable y is the lateral acceleration $a_y = (\dot{v} + Vr)$. The A, B, C and D matrices in the standard state space notation are then given by:

$$A = -\begin{bmatrix} \frac{C_{\alpha f}+2C_{\alpha r}}{mV} & V + \frac{C_{\alpha f}a-2C_{\alpha r}b}{mV} \\ \frac{C_{\alpha f}a-2C_{\alpha r}b}{mVk^2} & \frac{C_{\alpha f}a^2+2C_{\alpha r}b^2}{mVk^2} \end{bmatrix} \qquad B = \begin{bmatrix} \frac{C_{\alpha f}}{m} & \frac{C_{\theta f}a+2C_{\alpha r}K_{\delta_r}}{m} \\ \frac{aC_{\alpha f}}{mk^2} & \frac{aC_{\theta f}-2bC_{\alpha r}K_{\delta r}}{mk^2} \end{bmatrix}$$

$$C = -\begin{bmatrix} \frac{C_{\alpha f}+2C_{\alpha r}}{mV} & \frac{C_{\alpha f}a-2C_{\alpha r}b}{mV} \end{bmatrix} \qquad D = \begin{bmatrix} \frac{C_{\alpha f}}{m} & \frac{C_{\theta f}+2C_{\alpha r}K_{\delta r}}{m} \end{bmatrix}$$

The Matlab function *ss2tf* is used to obtain a transfer function relating the lateral acceleration to each input variable. Finally a transfer function is applied to the lateral acceleration output to represent the tyre lag (see section 5.1.5):

$$\frac{\alpha'}{\alpha} = \frac{\frac{V}{\sigma}}{s + \frac{V}{\sigma}} \tag{7.6}$$

This results in the third order transfer functions G_1 and G_2 describing the relationship between the lateral acceleration and the steer and the lateral acceleration and tilt angle respectively:

$$a_y = G_1\delta_f + G_2\theta \tag{7.7}$$

7.2.2 Kinematics and Cabin Moment

In order to get an accurate value for the moment applied about the tilt bearing, it is necessary to include the kinematic effects resulting from the tilt bearing inclination. From chapter 6 equation 6.14 was obtained to describe the moment about the tilt bearing.

$$M_x L = [(m_f L - bm)z_{c\theta} + bmz_c]a_y - [bmy_{fc} + (m_f L - bm)y_c]g + LI_c\ddot{\theta} \tag{7.8}$$

Where the linearised values of y_{fc}, y_c, z_c and $z_{c\theta}$ are given by:

$$\begin{aligned} y_f &= (h_\theta + \xi l)\theta && (7.9)\\ y_c &= (h_c - h_\theta - l_c\xi)\theta && (7.10)\\ z_c &= \left(h_c - h_\theta\frac{a_c}{a_\theta}\right) + h_\theta\frac{a_c}{a_\theta} && (7.11)\\ z_\theta &= h_\theta && (7.12)\\ z_{c\theta} &= (z_c - z_\theta) && (7.13)\\ y_{fc} &= (y_f + y_c) && (7.14) \end{aligned}$$

The transfer functions for the moment about the tilt bearing M_x over the tilt angle θ and over the lateral acceleration a_y are then given by:

$$G_3 = \frac{(LI_c)s^2 - (bmy_{fc} + (m_f L - bm)y_c)g}{L} \tag{7.15}$$

$$G_4 = \frac{((m_f L - bm)z_{c\theta} + bmz_c)}{L} \tag{7.16}$$

where

$$M_x = G_3\theta + G_4 a_y \tag{7.17}$$

7.2.3 Suspension Dynamics

At the principal frequencies (0-2Hz), the roll dynamics are dominated by the suspension and the tyre stiffnesses can be neglected. It is possible to model the rear module as a single degree of freedom system. The roll of the rear module is then given by the following equation:

$$(I_r + Ic)\ddot{\phi} = -\frac{T^2}{2}\phi K_s - \frac{T^2}{2}\dot{\phi}C_s - m_c g h_{r\theta}\phi + \frac{b}{L}mgh_{r\theta}\phi + m_c a_y h_{r\theta} - \frac{b}{L}mh_{r\theta}a_y - \frac{a}{L}mh_r a_y - K_{r\phi}\phi - M_x + \frac{1}{L}(bmy_{fc} + (m_c L - bm)y_c)g\phi \quad (7.18)$$

The final term represents the additional moment about the tilt bearing as a result of the extra cabin tilt angle due to the suspension roll.

The above equation can be represented in state-space with the state vector x and input vector u:

$$x = \begin{bmatrix} \phi \\ \dot{\phi} \end{bmatrix} \qquad u = \begin{bmatrix} a_y \\ M_x \end{bmatrix} \quad (7.19)$$

The output variable y is the load transfer $\Delta F_z = -(\phi K_s + \dot{\phi}C_s)\frac{T}{2}$. The A, B, C and D matrices are then given by:

$$A = \begin{bmatrix} 0 & 1 \\ (-\frac{T}{2}K_s - m_c g h_{r\theta} + \frac{b}{L}mgh_{r\theta} - K_{r\phi} \\ +\frac{1}{L}(bmy_f c + (m_f L - bm)y_c)g)\frac{1}{(I_r+Ic)} & -\frac{T^2 C_s}{2I_r} \end{bmatrix} \quad B = \begin{bmatrix} 0 & 0 \\ (m_c h_{r\theta} - \frac{b}{L}mh_{r\theta} & -\frac{1}{I_r} \\ -\frac{a}{L}mh_r a_y)\frac{1}{I_r+I_c} & \end{bmatrix}$$

$$C = -\begin{bmatrix} \frac{TK_s}{2} & \frac{TC_s}{2} \end{bmatrix} \qquad D = \begin{bmatrix} 0 & 0 \end{bmatrix}$$

The transfer functions relating the load transfer to the input variables are again obtained through the *ss2tf* function, giving:

$$\Delta F_z = G_5 a_y + G_6 M_x \tag{7.20}$$

7.2.4 Valve and Actuator Dynamics

Using small perturbation analysis, the linearised equation for the flow through the valve around the centre position is:

$$Q_L = K_q x_v + K_c \Delta P_L \tag{7.21}$$

where K_q and K_c are the flow gain and the pressure gain at the operating conditions, which are equivalent to the partial derivatives of the valve orifice equation:

$$Q = C_e x_v \sqrt{P_s - \Delta P_L} \tag{7.22}$$

where ΔP_L is the load pressure on the system $(P_1 - P_2)$ at the operating conditions. The values of K_q and K_c are therefore given by:

$$K_q = \frac{\partial Q}{\partial x_v} = C_e \sqrt{P_s - \Delta P_L} \tag{7.23}$$

$$K_c = \frac{\partial Q}{\partial \Delta P_L} = \frac{-C_e x_v}{\sqrt{P_s - \Delta P_L}} \tag{7.24}$$

The valve coefficient C_e is given by:

$$C_e = \frac{q_{nom}}{\sqrt{\frac{\Delta P_{nom}}{2}}} \tag{7.25}$$

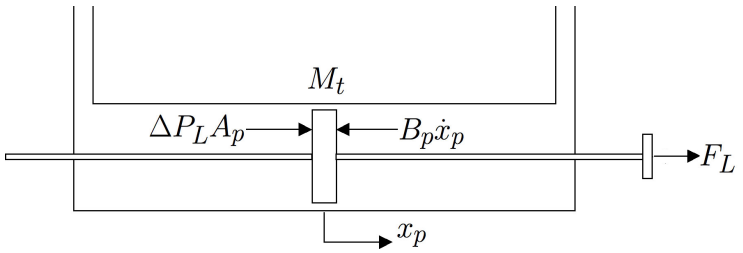

Figure 7.3: Forces acting upon double ended actuator [35]

A nominal flow q_{nom} of 16 l/min at a pressure drop ΔP_{nom} of 10 bar with 100% valve opening [50] results in a valve coefficient value $C_e = 3.771 \cdot 10^{-7} m^4/s\sqrt{N}$. This value is calculated assuming that the valve opening is measured as a percentage of the maximum valve opening, i.e. when fully open $x_v = 1$.

The values of ΔP_L and x_v at the operating conditions were determined using the non-linear model as 138.7bar and 0.0123. This results in the values $5.504 \cdot 10^{-4}$ and $-3.187 \cdot 10^{-12}$ for K_q and K_c respectively.

From section 3.4, the actuator flow is given by:

$$Q_1 = A_p \dot{y} + q_{c1} = A_p x_p s + \frac{V_1}{2\beta_e} \Delta P_L s \tag{7.26}$$

$$Q_2 = A_p \dot{y} + q_{c2} = A_p x_p s + \frac{V_2}{2\beta_e} \Delta P_L s \tag{7.27}$$

where s is the Laplace operator and V_1 and V_2 are the volumes in each hydraulic cylinder and are equivalent to $\frac{V_t}{2}$ in the central position. Therefore $Q_1 = Q_2 = Q_L$. The equation can be rearranged for ΔP_L:

$$\Delta P_L = (Q_L - A_p x_p s) \frac{4\beta_e}{V_t s} \tag{7.28}$$

As the system is linearised about the central position, it is possible to simplify the actuator system by modelling the two actuators as a single double-ended actuator as shown in figure 7.3.

Resolving the forces acting on the piston:

$$M_t\ddot{x}_p = A_p\Delta P_L - B_p\dot{x}_p + F_L \tag{7.29}$$

This gives the transfer function:

$$x_p = \frac{A_p\Delta P_L + F_L}{M_t s^2 + B_p s} \tag{7.30}$$

The hydraulic system can be represented by the block diagram shown in figure 7.4.

Substituting for ΔP_L using equation 7.28:

$$x_p = G_9 x_v + G_{10} F_L \tag{7.31}$$

The transfer functions G_9 and G_{10} can be obtained by manipulating the block diagram:

$$G_9 = \frac{\frac{K_q}{A_p}}{\frac{V_t M_t}{4\beta_e A_p^2}s^3 + (\frac{V_t B_p}{4\beta_e A_p^2} - \frac{K_c M_t}{A_p^2})s^2 + (1 - \frac{B_p K_c}{A_p^2})s} \tag{7.32}$$

$$G_{10} = \frac{V_t s - 4\beta_e K_c}{(M_t V_t)s^3 + (B_p V_t - 4\beta_e K_c M_t)s^2 + (4\beta_e(A_p^2 - B_p K_c))s} \tag{7.33}$$

The relationship between the tilt demand θ_d and the actual angle θ as a result of the actuator dynamics can be approximated by a first order lag. By ignoring the external load and including the tilt angle feedback loop, the closed loop hydraulic circuit can

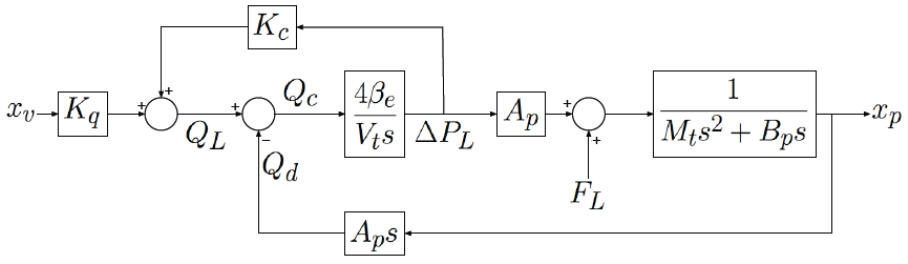

Figure 7.4: Linearised block diagram of hydraulic system [35]

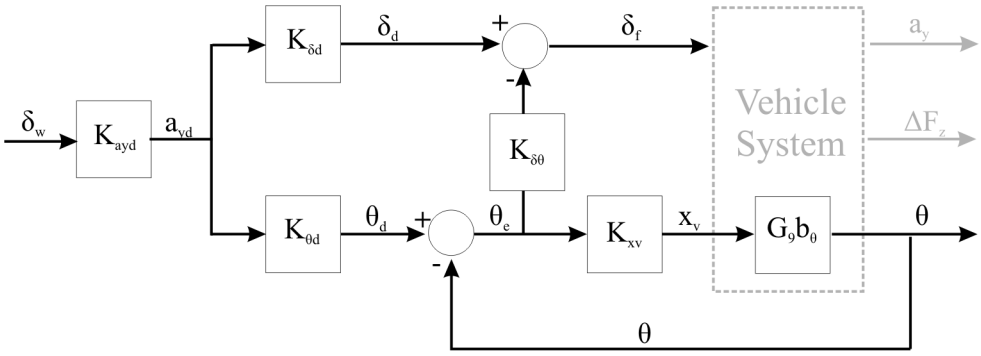

Figure 7.5: Controller including position feedback control of the hydraulic system

be represented by the block diagram shown in figure 7.5.

The transfer function relating θ to θ_d is then given by:

$$\begin{aligned}
\frac{\theta}{\theta_d} &= \frac{G_9 K_{xv} b_\theta}{1 - G_9 K_{xv} b_\theta} \\
&= \frac{\frac{K_q}{A_p} K_{xv} b_\theta}{\frac{V_t M_t}{4\beta_e A_p^2} s^3 + (\frac{V_t B_p}{4\beta_e A_p^2} - \frac{K_c M_t}{A_p^2}) s^2 + (1 - \frac{B_p K_c}{A_p^2}) s + \frac{K_q}{A_p} K_{xv} b_\theta} \\
&= \frac{\frac{K_q K_{xv} A_p b_\theta}{A_p^2 - B_p K_c}}{\left(\frac{s^2}{\omega_n^2} + \frac{2\zeta}{\omega_n} s + 1\right) s + \frac{K_q K_{xv} A_p b_\theta}{A_p^2 - B_p K_c}}
\end{aligned} \tag{7.34}$$

By neglecting the higher order dynamics that are significant at frequencies above the vehicle dynamics, the system can be simplified to a first order lag with a time constant τ, giving the transfer function G_{9a}:

$$G_{9a} = \frac{\theta}{\theta_d} = \frac{1}{1 + \tau s}$$

where

$$\tau = \frac{A_p^2 - B_p K_c}{K_q K_{xv} A_p b_\theta} \tag{7.35}$$

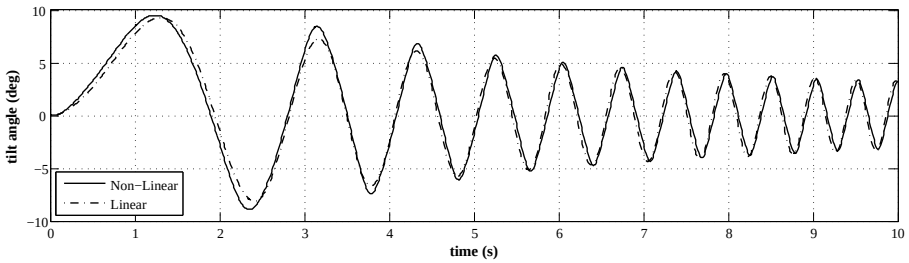

Figure 7.6: Non-linear tilt angle response and first order linear fit

This approximation assumes that the relationship between the tilt demand and achieved tilt angle is only dependent on the actuator dynamics. Although the assumption significantly simplifies the resulting transfer functions, it still offers a good match to the non-linear hydraulic performance resulting from a tilt angle demand input. Figure 7.6 shows the tilt angle response resulting from a 0.1 to 2Hz sweep in tilt angle demand as calculated by the non-linear model and the response obtained using the first order lag G_{9a}. As a good fit is obtained, the simplified hydraulic model will be used for the subsequent analysis.

7.2.5 Control System Transfer Function

Using the same approximating techniques as in the previous section, the transfer function relating δ_f to δ_d is given by:

$$G_{10} = \frac{\delta_f}{\delta_d} = 1 - \frac{\tau s}{1+\tau s}\frac{K_{\theta d}K_{\delta\theta}}{K_{\delta d}} \tag{7.36}$$

Setting $K_{\delta\theta} = 0$ results in the original control method.

7.2.6 Vehicle System Transfer Functions

With the simplifications previously described, the vehicle system can be described by the transfer function matrix:

$$\begin{bmatrix} a_y \\ \Delta F_z \end{bmatrix} = \begin{bmatrix} P_{11} & P_{12} \\ P_{21} & P_{22} \end{bmatrix} \begin{bmatrix} \delta_f \\ \theta_d \end{bmatrix} \tag{7.37}$$

where

$$P_{11} = \frac{a_y}{\delta_f} = G_1 \tag{7.38}$$

$$P_{12} = \frac{a_y}{\theta_d} = \frac{\theta}{\theta_d} \cdot \frac{a_y}{\theta} = G_{9a} G_2 \tag{7.39}$$

$$P_{21} = \frac{\Delta F_z}{\delta_f} = \frac{a_y}{\delta_f} \cdot \frac{\Delta F_z}{a_y} + \frac{a_y}{\delta_f} \cdot \frac{M_x}{a_y} \cdot \frac{\Delta F_z}{M_x} = G_1 G_5 + G_1 G_4 G_6 \tag{7.40}$$

$$\begin{aligned} P_{22} = \frac{\Delta F_z}{\theta_d} &= \frac{\theta}{\theta_d} \cdot \frac{a_y}{\theta} \cdot \frac{M_x}{a_y} \cdot \frac{\Delta F_z}{M_x} + \frac{\theta}{\theta_d} \cdot \frac{M_x}{\theta} \cdot \frac{\Delta F_z}{M_x} + \frac{\theta}{\theta_d} \cdot \frac{a_y}{\theta} \cdot \frac{\Delta F_z}{a_y} \\ &= G_{9a} G_2 G_4 G_6 + G_{9a} G_3 G_6 + G_{9a} G_2 G_5 \end{aligned} \tag{7.41}$$

Finally, to obtain δ_f and θ_d as a function of the lateral acceleration demand a_{yd}:

$$\begin{bmatrix} \delta_d \\ \theta_d \end{bmatrix} = a_{yd} \begin{bmatrix} K_{\delta d} G_{10} \\ K_{\theta d} \end{bmatrix} \tag{7.42}$$

7.2.7 Linearisation Results

Using the above transfer functions individually, a good correlation was obtained between the linear and non-linear model. Although a good fit was found up to frequencies of 10Hz, the results are displayed for 0.1 - 2Hz as this largely encompasses the frequencies that can be encountered when the vehicle is driven.

Figures 7.7 and 7.8 show the linear and non-linear lateral acceleration and load transfer response for a steer input at the steering wheel of $\pm$ 45°with driving speed of 30km/h. This is equivalent to a steering angle at the wheel δ_f of $\pm$ 3.8°. It can be seen that the linear and non-linear results remain very close across the entire frequency range. Figures 7.9 and 7.10 show the lateral acceleration and load transfer response for a tilt

demand input θ_d of $\pm$ 10° at 30km/h. Figure 7.9 shows a good match for the lateral acceleration response across the entire frequency range. The load transfer shown in figure 7.10 on the other hand, does not result in an equally good match. At the lower frequencies, the non-linear model appears to have a phase lag when compared to the linear model. It can be seen that the load transfer response is more non-linear at the lower frequencies than at higher frequencies. This is likely to be because the gravitational forces acting on the cabin are more significant at lower frequencies.

The combined lateral acceleration and load transfer response is shown in figures 7.11 and 7.12. This represents the vehicle response under normal operating conditions, i.e. the steering angle input from the driver is used in conjunction with the vehicle speed to calculate the tilt angle demand (equation 2.23). As anticipated, the match between the linear and non-linear results are not as good as when looking at the steer and tilt inputs individually, due to the non-linearity of the system.

7.3 Frequency Domain Analysis

Using the above transfer functions, it is possible to plot the frequency response of the vehicle lateral acceleration and load transfer against the demand lateral acceleration, as shown in figures 7.13 and 7.14. It is worth noting that the lateral acceleration load transfer response both reach a maximum amplitude at approximately 1.5Hz. This gives a quantitative reason for the 2Hz low-pass filter, which would have attenuated the additional load applied by the actuator at these frequencies. It was reported by Drew [35] that the cut-off frequency would have been further reduced, if this did not result in a "sluggish" driving sensation.

With the confidence that the linear model gives a good representation of the system dynamics, it is possible to compare the original system response with that of the proposed controller over the entire frequency range of interest. Figures 7.15 and 7.16 show the lateral acceleration and load transfer response of the original controller ($K_{\delta\theta} = 0$) compared to that of the proposed controller. The system response is shown for a range of steering gains $K_{\delta\theta}$ from 0.2 to 0.4. This was chosen so that the lateral acceleration amplitude would never exceed the demand lateral acceleration amplitude, which is satisfied with a value of $K_{\delta\theta} = 0.2$. For the previous control method the actual lateral acceleration can be seen to exceed the demand lateral acceleration over a significant part of the frequency range, leading to an increase in the load transfer. This would

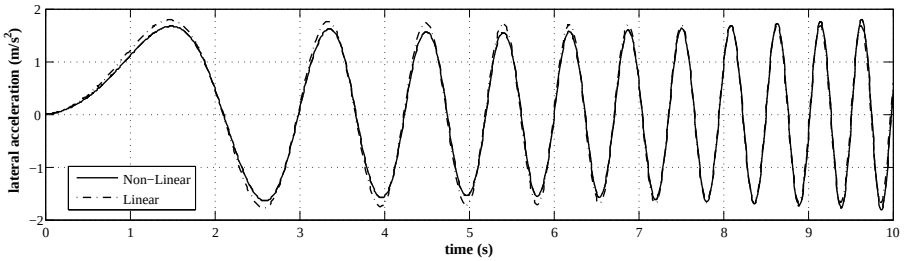

Figure 7.7: Linear and non-linear lateral acceleration response to a steer input

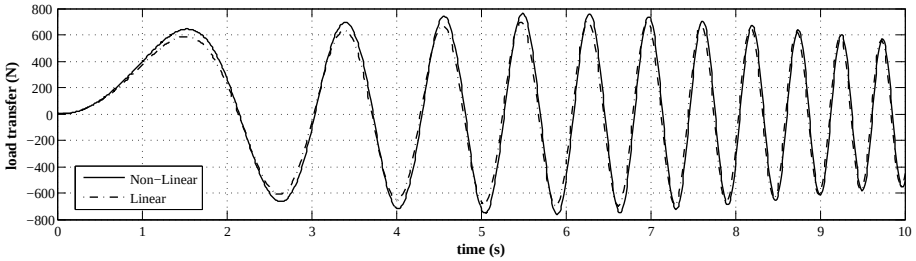

Figure 7.8: Linear and non-linear load transfer response to a steer input

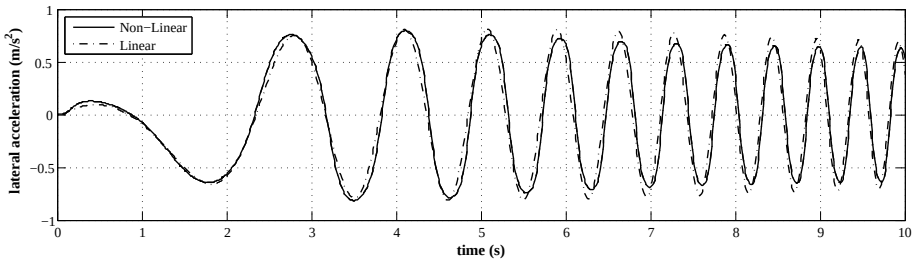

Figure 7.9: Linear and non-linear lateral acceleration response to a tilt demand input

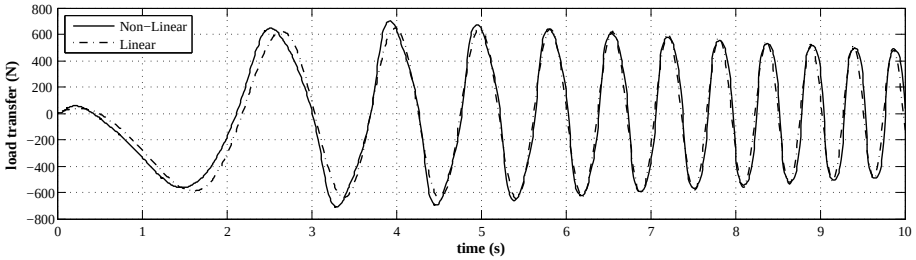

Figure 7.10: Linear and non-linear load transfer response to a tilt demand input

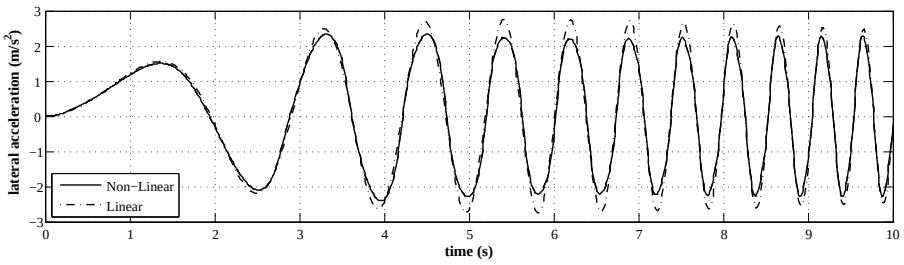

Figure 7.11: Linear and non-linear lateral acceleration response to a combined steer and tilt demand input

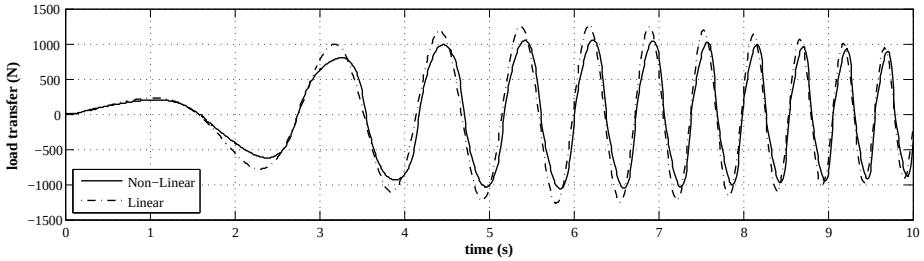

Figure 7.12: Linear and non-linear load transfer response to a combined steer and tilt demand input

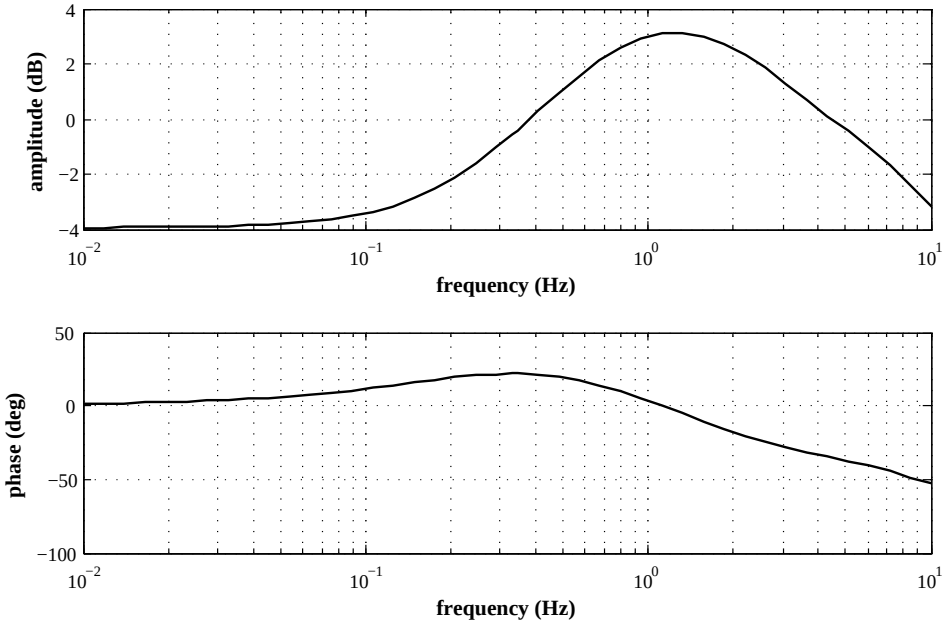

Figure 7.13: Bode plot of lateral acceleration response for original controller

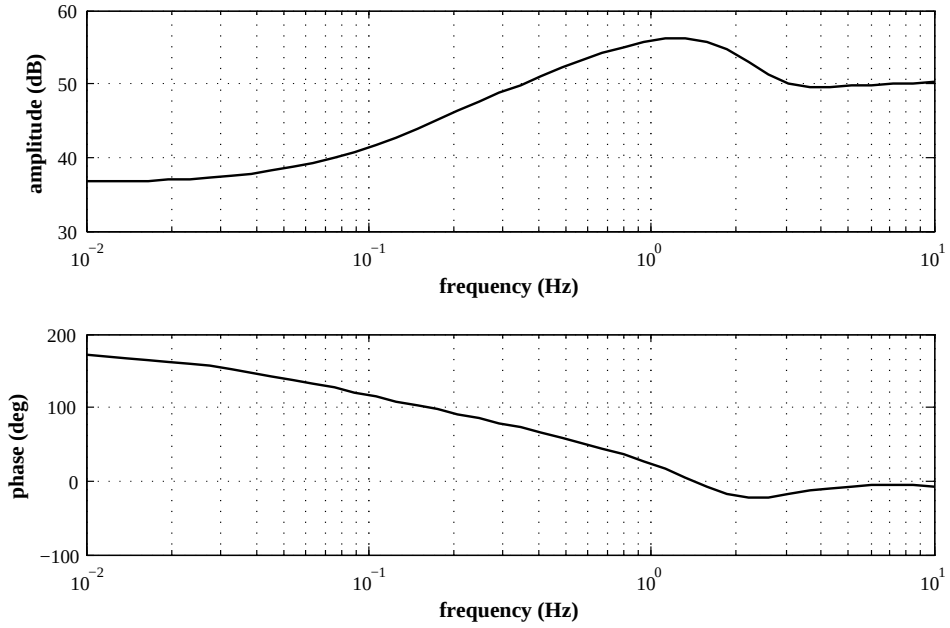

Figure 7.14: Bode plot of load transfer response for original controller

have been an important factor contributing to the transient state instability of the vehicle. With the new control approach however, the lateral acceleration does not exceed the demand lateral acceleration. As a result, the load transfer is also reduced over the principal frequency range of 0.1 - 2Hz. It should be noted that at lower frequencies, the achieved lateral acceleration does not match the demand lateral acceleration due to the under-steer effect introduced by the kinematic rear-wheel steer (see chapter 2). With the correct amount of rear wheel steer, this would be much closer to 1 (0dB). In this case a higher steering gain $K_{\delta\theta}$ would be required to keep the ratio $\frac{a_y}{a_{yd}}$ as close as possible to 0dB over the principal frequency range. It can be argued that for a neutral and predictable handling response, the lateral acceleration response should remain constant across the frequency range. This can be achieved with a steering gain value of 0.4. By increasing the gain any further, the lateral acceleration response deviates further from the demand acceleration. Increasing the gain up to 0.4 also leads to a positive effect on the load transfer as can be seen in figure 7.16. The optimal gain value is therefore thought to lie in the range of 0.2 to 0.4, where a steering gain $K_{\delta\theta}$ of 0.4 appears to give the most promising results in the frequency domain. The system response will be investigated in the time domain to confirm these findings.

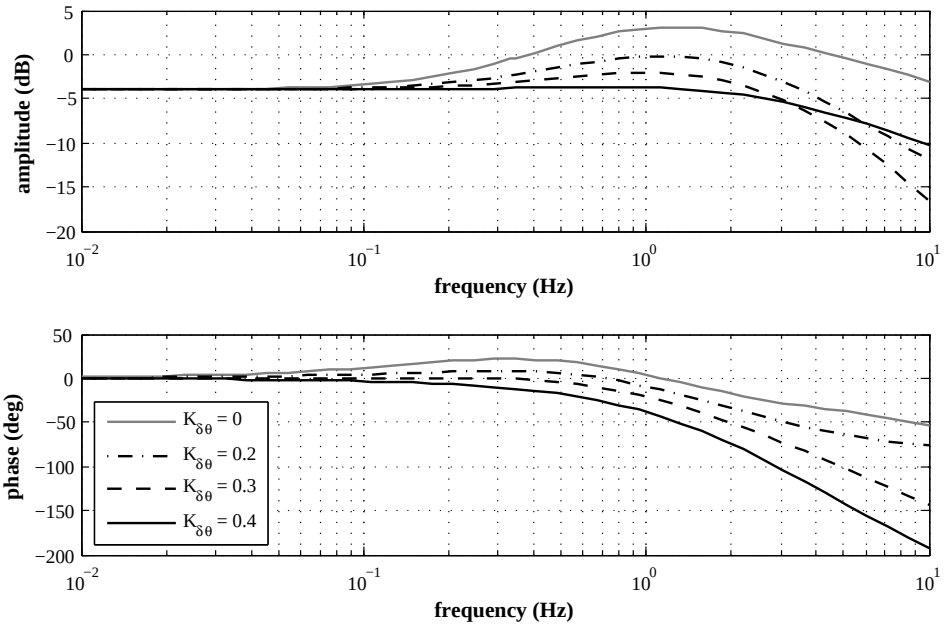

Figure 7.15: Bode diagram of $\frac{a_y}{a_{yd}}$ for original and new controller

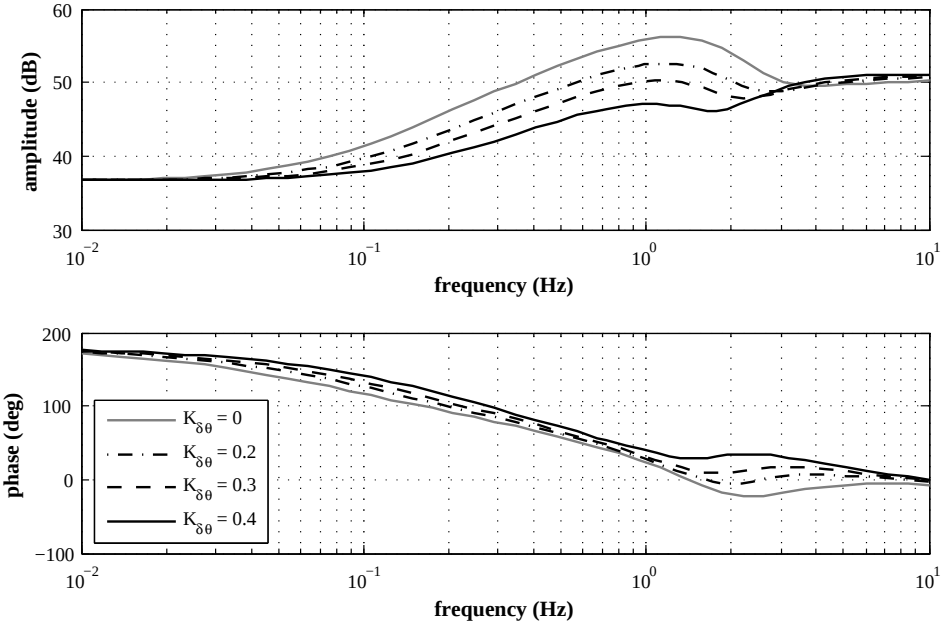

Figure 7.16: Bode diagram of $\frac{\Delta F_z}{a_{yd}}$ for original and new controller

7.4 Time Domain Response

The controller was designed in the frequency domain with the system linearised about the centre position and a vehicle forward speed of 30 km/h. Performance will be investigated in the time domain with the non-linear model. As the principal aim of the controller is to improve transient state performance, a number of manoeuvres will be investigated where the original control method would have brought the vehicle to the brink of roll-over (i.e. zero inner wheel load) and the vehicle dynamics of the original and new control approach are compared. As a starting point it is possible to refer back to the manoeuvre shown in figure 6.9, where it was shown that a large tilt angle error resulted in a large load transfer causing the vehicle to nearly roll-over. The same manoeuvre has been repeated with the new control approach using the full non-linear simulation and the lateral acceleration and load transfer response is compared with the original response.

Looking at figure 7.17, it can be seen that the lateral acceleration builds up more gradually with the new control approach. As a result, there is significantly less overshoot and the lateral acceleration settles to the steady state value more rapidly. The more gradual build-up of lateral acceleration and reduced actuator loads lead to a significant reduction in the load transfer, as shown in figure 7.18. Whereas with the previous controller, this manoeuvre would almost lead to the vehicle rolling over, with the new strategy, the inner wheel load is still in a safe range.

The robustness of the new control method and the effect of the gain $K_{\delta\theta}$ can be investigated further by looking at the response to a step input, which would inevitably have lead to the vehicle rolling over with the original control method. Looking at figure 7.19, it can be seen that increasing the gain results in some counter-steering. This results in an even smaller load transfer as can be seen in figure 7.21 and a faster response in the tilt angle as seen in figure 7.22. Furthermore, it has a positive effect of reducing overshoot in the lateral acceleration and the lateral acceleration settles into steady state more rapidly. It could be argued that introducing some counter-steer would cause the vehicle to briefly travel in the opposite direction to that desired. However, with this control strategy, counter-steer would only occur in extreme situations, where it would be necessary to prevent roll-over. Furthermore, this would only occur for a fraction of a second, and would be unlikely to be noticed by the driver, similar to the counter-steering effects on a motorcycle. Looking at the lateral acceleration profile in figure 7.20, it can be seen that the proportion of time spent at a negative lateral acceleration for the initial input is extremely small, but that the benefits in terms of load transfer

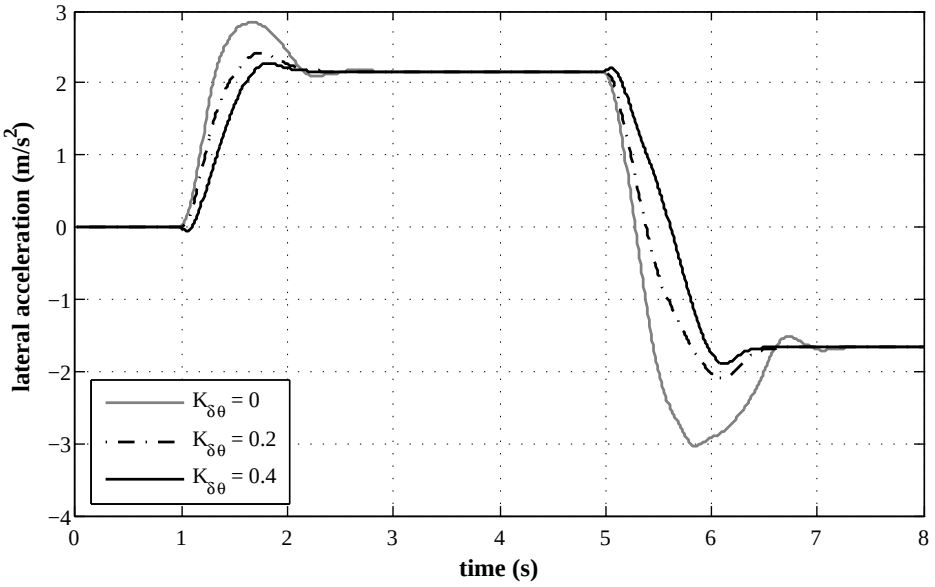

Figure 7.17: Lateral acceleration response for entering and exiting a steady state corner using the original and new controller

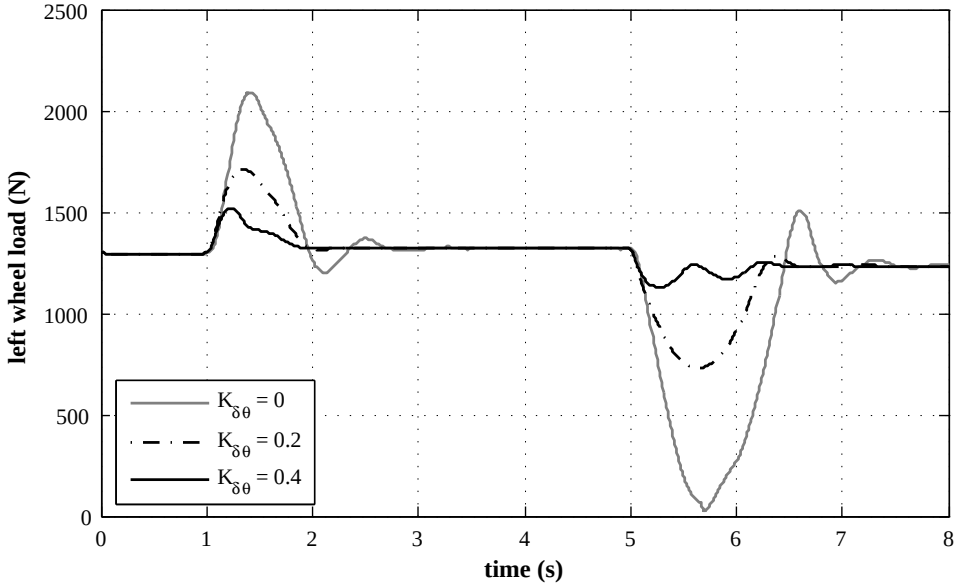

Figure 7.18: Left wheel load for entering and exiting a steady state corner using the original and new controller

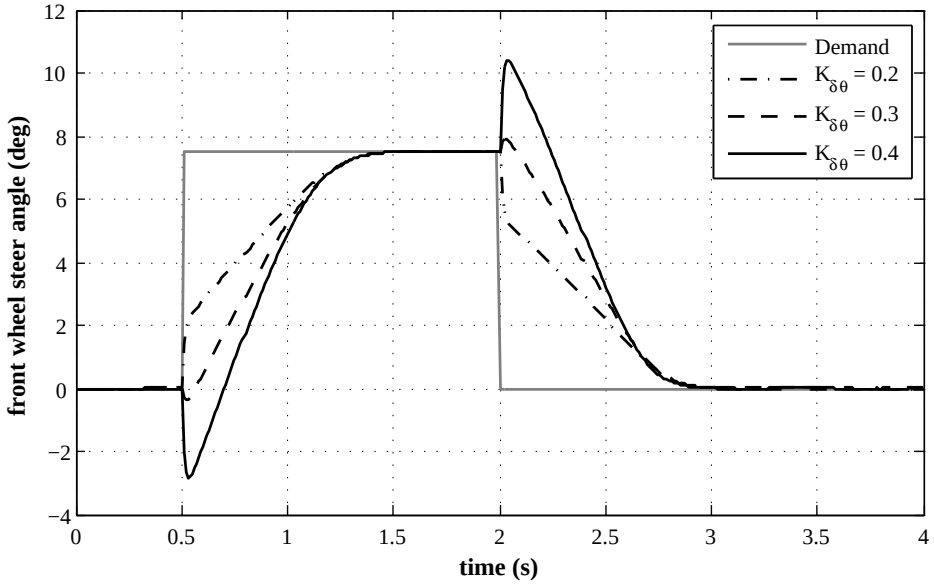

Figure 7.19: Steer response to a step input in the lateral acceleration demand

are significant. The ideal value for the steering gain $K_{\delta\theta}$ at a driving speed of 30 km/h is therefore thought to be 0.4.

The optimal steering gain is likely to be velocity dependent. The process was therefore repeated at 10km/h intervals up to 120km/h, which represents the operating range of the vehicle. The results are shown in figure 7.23. The optimal value was chosen as the value of $K_{\delta\theta}$ that resulted in the flattest $\frac{a_y}{a_{yd}}$ amplitude profile, similar to that obtained for $K_{\delta\theta} = 0.4$ at 30km/h. With the correct kinematic set-up, this should result in the lateral acceleration matching the lateral acceleration demand across the principal frequency range and give a safe and predictable handling performance.

It can be seen that the steering gain reaches horizontal asymptotes at each end of the speed range. At low speed there is very little lateral force resulting from a steer input and therefore steering gain has little effect. At high speed, the resultant forces are much larger and hence a smaller gain is required to achieve the desired response. The results shown in figure 7.23 could be applied as a look-up table in the vehicle controller.

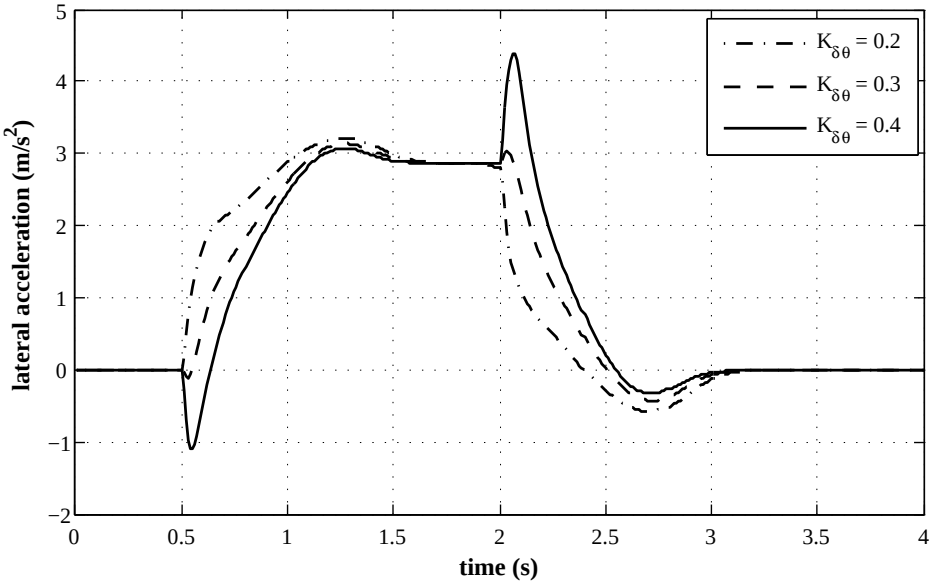

Figure 7.20: Lateral acceleration response to a step input in the lateral acceleration demand

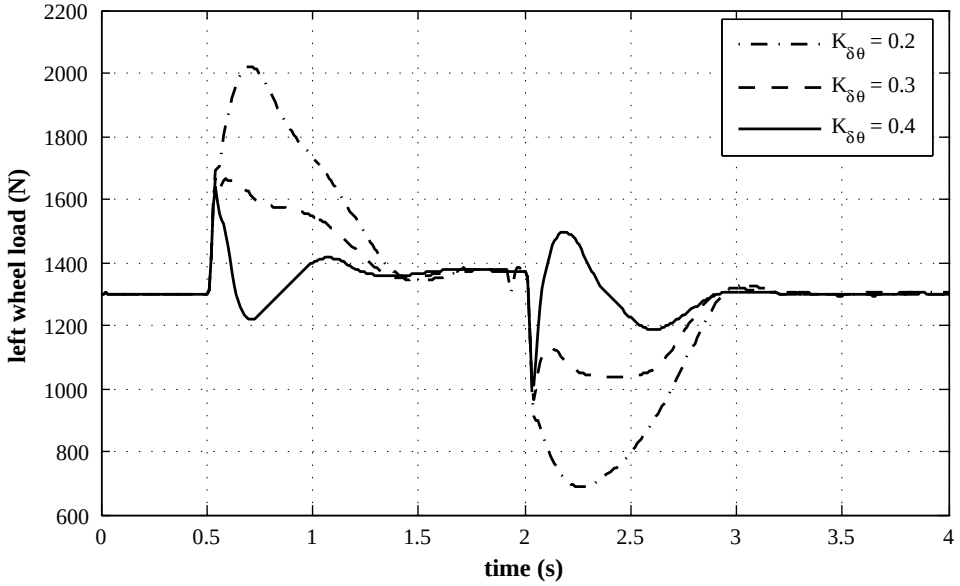

Figure 7.21: Left wheel load response to a step input in the lateral acceleration demand

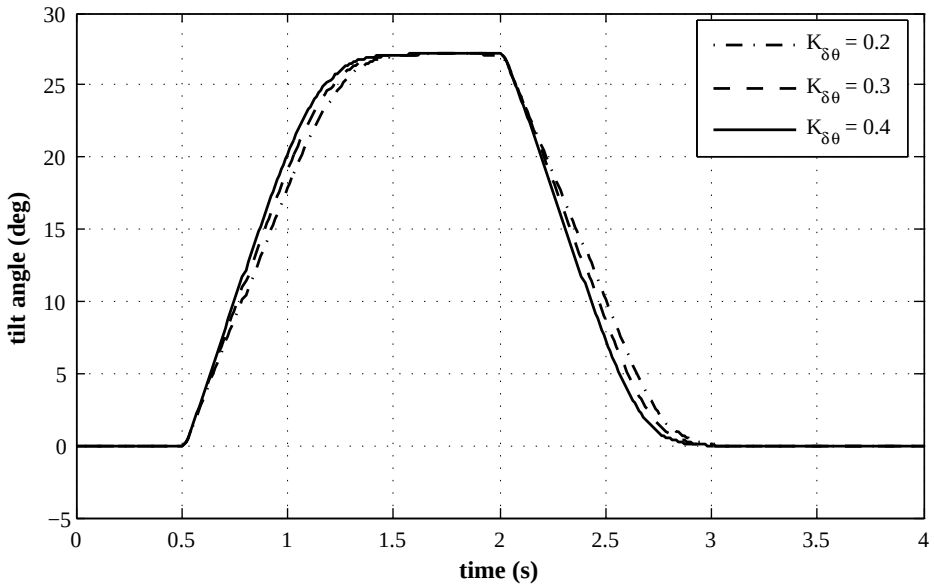

Figure 7.22: Tilt angle response to a step input in the lateral acceleration demand

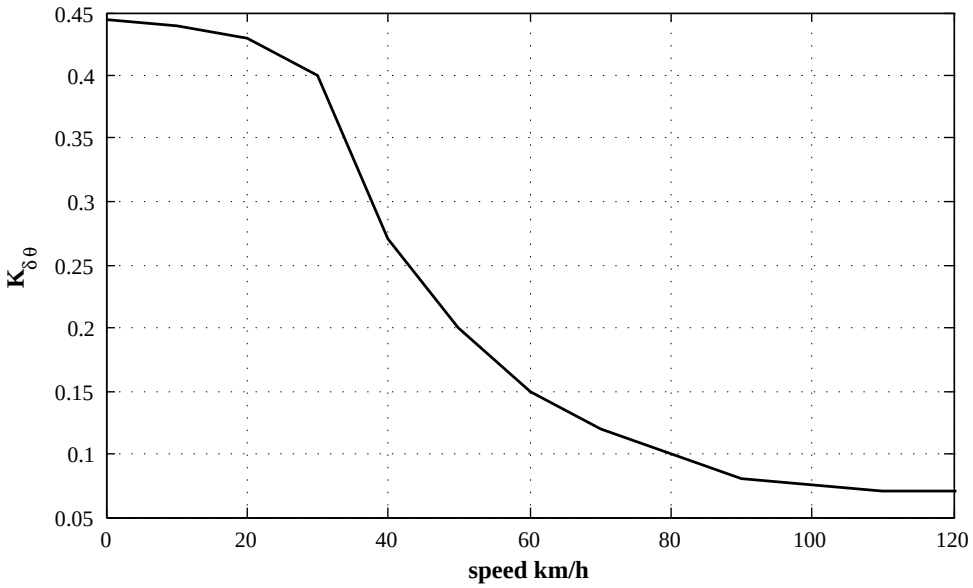

Figure 7.23: Steering gain against forward speed

7.5 Concluding Remarks

In this chapter the vehicle model was linearised in order to analyse the system performance in the frequency domain. The linear model was shown to give a good fit to the non-linear model. The frequency domain response of the current system displayed a peak in the lateral acceleration and load transfer response at around 1.5Hz, this matched the observations made previously in subjective tests. Around this frequency, the lateral acceleration was considerably higher than the demand lateral acceleration, as the initial steering input would lead to large slip angles at the front and rear. This leads to a large load transfer across the rear axle and is a significant factor contributing to the transient state instability of the vehicle.

The proposed control system treats the driver steering input as a lateral acceleration demand that is to be reached as rapidly as possible and with minimum load transfer across the rear axle. It utilises a negative gain feedback between the tilt-error and the steer input, reducing the steering angle as the tilt error increases. As a result the forces which act on the actuator are significantly reduced and the desired tilt angle can be reached more rapidly and with less load transfer. The system was linearised about the central position at a driving speed of 30km/h, and an ideal steering gain was determined at this speed. The process was repeated in 10km/h intervals from 0 - 120km/h to obtain the optimal steering gain over the speed range of the vehicle.

The frequency response analysis of the proposed control system displayed a much more predictable handling response coupled with reduced load transfer across the rear axle. The controller was tested for robustness using the non-linear model. Using the non-linear model, the lateral acceleration response was shown to be more gradual when compared to the original control method. As a result, there is less overshoot and the lateral acceleration settles to the steady state value more rapidly. The resultant load transfer for a demanding manoeuvre using the new control method was shown to be approximately 15% of the original value. The new control method was also shown to result in some counter-steering in rapid steering manoeuvres. This helps to rapidly tilt the cabin to the desired tilt angle and simultaneously reduce load transfer. As a result the controller is shown to be very robust, even in extreme manoeuvres.

Chapter 8

Conclusions

The CLEVER concept vehicle was developed as part of a EU consortium in an attempt to provide an alternative mode of transport with a small road-footprint and reduced carbon dioxide emissions. The resultant vehicle was only 1 metre wide and fully enclosed the driver and passenger. An active direct tilt control system was develpoped in order to tilt the vehicle into corners to prevent the vehicle from rolling over at higher lateral accelerations. Although the vehicle performed well in steady state, initial testing revealed that transient dynamics could lead to the vehicle rolling over.

In the current work a full vehicle model was developed in order to investigate the transient state dynamics and test an improved control method. The model was validated against test data obtained in numerous experiments performed with the prototype vehicle. The principal causes of the instability of the vehicle were identified as transient peaks in actuator forces applied to the cabin combined with roll moments associated with lateral acceleration. As the actuator forces are reacted against the non-tilting rear module, the sum of the moments could become large enough to bring the vehicle to the point of roll-over.

A lateral dynamics optimisation study revealed that independent steer control of the front wheel is necessary in order to achieve the necessary lateral handling performance. Previous attempts at combining STC and DTC have led to complex switching strategies or weighting functions to switch from one mode to the other. These, however led to poor response around the switching points, required a large number of sensory inputs and often led to an unnatural driving experience. A new strategy was therefore proposed which combined STC and DTC as a concurrent control strategy. Both systems are

active throughout the speed range of the vehicle and use the driver steer input as the single control input. Simulations showed that the weight transfer across the rear axle in transient states was significantly reduced and that the lateral acceleration settled to the steady state value more rapidly than with the previous control method. In summary, the research presented shows that it is possible to obtain a safe and predictable handling characteristic for a three-wheeled tilting vehicle. The vehicle can be fully enclosed and steered in a similar fashion to a car, offering a viable alternative to other modes of transport.

8.1 Research Achievements

In a review of the current system, the basic operating principles of the CLEVER vehicle were presented. It was shown that adjustments to the tilt axis inclination would have to be made to achieve the desired neutral handling. Furthermore, the constraints on a new control system resulting from the kinematic set-up of the vehicle were discussed.

A full vehicle model was developed. The model initially consisted of five degrees-of-freefom. To validate the model in bounce and roll, the test-vehicle was placed on a three post rig. The experiments revealed that the vehicle dynamics were significantly more complex than initially anticipated and that the tilt joint stiffness played a major role in the dynamics response. The model was then extended to a multi-body model. With the added degrees of freedom, a good match was shown between the measured and simulated roll and bounce dynamics, giving a better understanding of the dynamics observed in testing.

The lateral dynamics of the vehicle were modelled using a non-linear tyre model based on Pacejca's 'Magic Formula'. Test data was obtained for validation purposes at a local test track and a good fit was obtained between the measured and simulated response. However, the range of tests performed were limited due to the transient stability issues and limitations in the hardware and proving grounds.

Using a simple 2DOF model which included the tilting kinematics, it was possible to investigate the steady state stability and the effects of key parameters on the maximum steady state lateral acceleration. It was shown that the vehicle would be unable to reach 10m/s^2 steady state lateral acceleration in its current configuration and would therefore roll-over before reaching the adhesion limit of the tyres. Modifications would have to

be made to achieve safe steady state handling.

The transient state limitations were introduced using the 'moment reserve' concept based on the 2DoF model, where the additional moment that can be applied to the rear module is dependent on the lateral acceleration and tilt angle of cabin. The manoeuvres and sequence of events that leads to the transient state roll-over of the vehicle were presented in detail using the full vehicle model. It was shown that roll-over occured due to a combination of the rapid build up of lateral force resulting from a steer input before the cabin could be tilted to the desired angle, and the large moment applied by the actuators as a result of the tilt angle error. This led to an optimisation study, where it was assumed that the lateral and tilting motion of the vehicle could be controlled independently (as in a dual-control mode system). The tilting profile was assumed to follow an exponential decay for which parameters were optimised. It was shown that an ideal tilting profile could be found to maximise the lateral velocity of the vehicle without roll-over for steady state initial conditions. However, the profile assumed was inadequate for more complex manoeuvres. The study clearly showed that in order to optimise the lateral dynamics, a dual-control (SDTC) system would be required.

A linear model of the vehicle system was developed in order to analyse the lateral acceleration and load transfer response of the previous and proposed control system in the frequency domain. A good fit was obtained between the linear and the non linear model around the operating point. A peak in the lateral acceleration and load transfer response was observed around 1.5Hz, which matched previous observations made in subjective tests.

The proposed control system treated the driver steering input as a lateral acceleration demand. A negative gain feedback term was applied between the tilt-error and the steer input. This had the effect of reducing the front wheel steer as the tilt angle error increases, leading to a significant reduction in the forces acting on the actuator and the desired tilt angle being reached more rapidly with less weight transfer. The frequency analysis of the proposed control system displayed a much more predictable handling response coupled with reduced load transfer across the rear axle. Tests using the non-linear model revealed that the lateral acceleration response had less overshoot and settled to the steady state value more rapidly. This was coupled with a load transfer equivalent to approximately 15% of the original value. In extreme manoeuvres, the new control method would lead to counter-steering which would help to rapidly tilt the cabin to the desired tilt angle and reduce load transfer.

In conclusion, the research performed has led to a deeper understanding of the stability issues associated with a direct tilt controlled vehicle. A combined steer and tilt control strategy has been proposed and shown to improve handling and significantly reduce the risk of roll-over.

8.2 Further Work

It was shown that the current chassis design has a number of limitations preventing the vehicle from handling in a safe and predictable manner. Firstly, it was shown that the current tilt-axis inclination did not match the angle required for neutral handling. Furthermore, it was shown that even with improved transient state handling, the vehicle is unable to reach high enough lateral accelerations to reach the adhesion limit of the tyres. As a result, the vehicle would roll-over before reaching the onset of the tyres sliding. A full chassis redesign is therefore recommended to include these fundamental necessities.

The scenarios investigated in this thesis have been confined to constant forward velocity situations. However, it is well known that one of the fundamental problems of three wheeled vehicles is their stability under braking or acceleration ([51] [52]). More work therefore needs to be done to investigate the stability of three-wheeled vehicles under such circumstances. Furthermore, stability of the vehicle on cambered roads and low friction surfaces should be looked at in detail.

As the proposed control system is based only on the driver steering input, the vehicle might not be perfectly balanced, especially at higher lateral accelerations. The impact of this on the stability and handling of the vehicle could be investigated initially using simulations. However, an important aspect of any new control method is the impact on the driver and much of this is likely to be learned through subjective tests. Subjective tests also need to be performed on the steering feel of the proposed control system. It is important to convey to the driver how far he is from the handling limits of the vehicle. This could possibly be achieved through steering torque feedback.

Due to the safety implications in both transient and steady states, only limited experimental tests were performed. With the chassis design changes previously mentioned and a safe and robust controller, a significant amount of research remains to be done on the compatibility of this new class of vehicles with the expectations of todays commuters.

A benchmark vehicle could be used to compare the ride and handling characteristics of the three wheeled narrow vehicle against its four wheeled counterpart.

The implementation of the proposed control system in an updated chassis would represent a big step towards a new efficient form of personal transportation.

Appendix

A.1 Vehicle and Systems Modelling

A top level view of the multi-body model is shown in figure A.1

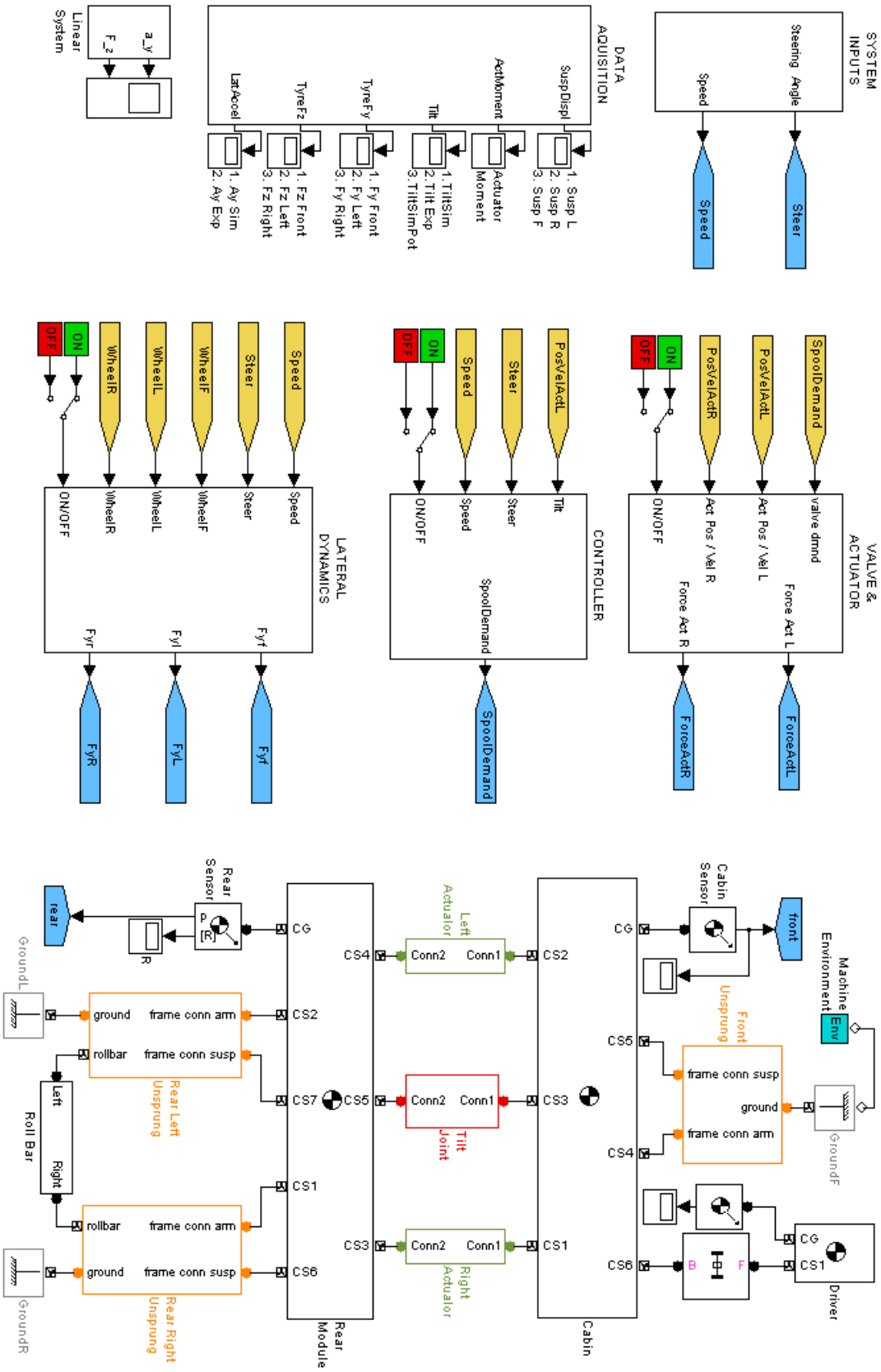

Figure A.1: Top level view of full multi-body model

A.2 Three Post Rig Experiments

Figure A.2: Pull string potentiometer mounting point

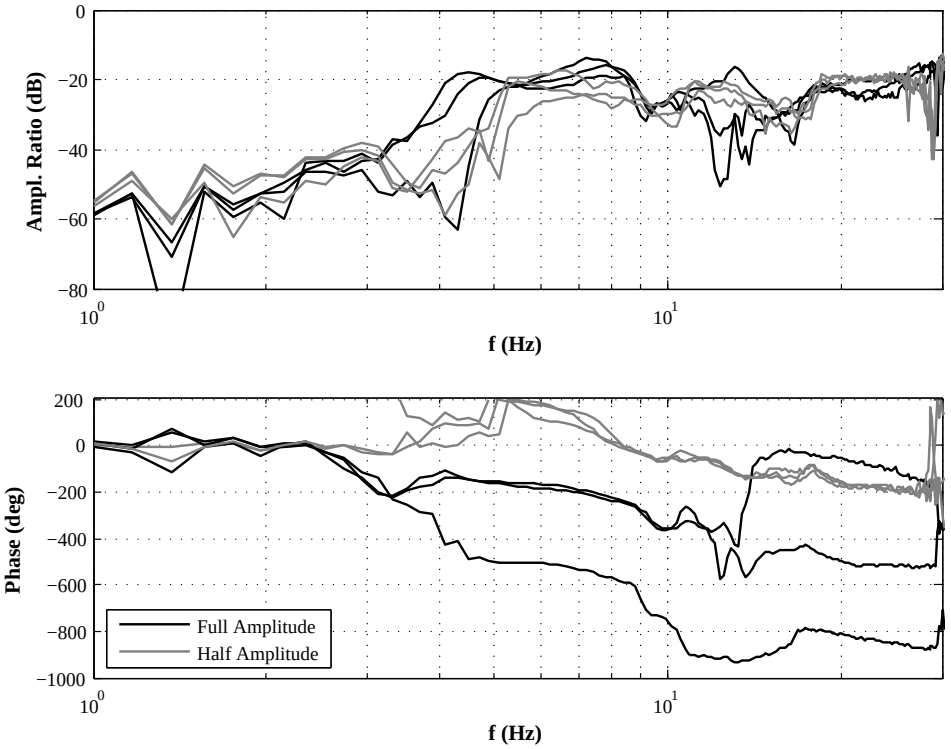

Figure A.3: Difference in suspension displacement in bounce

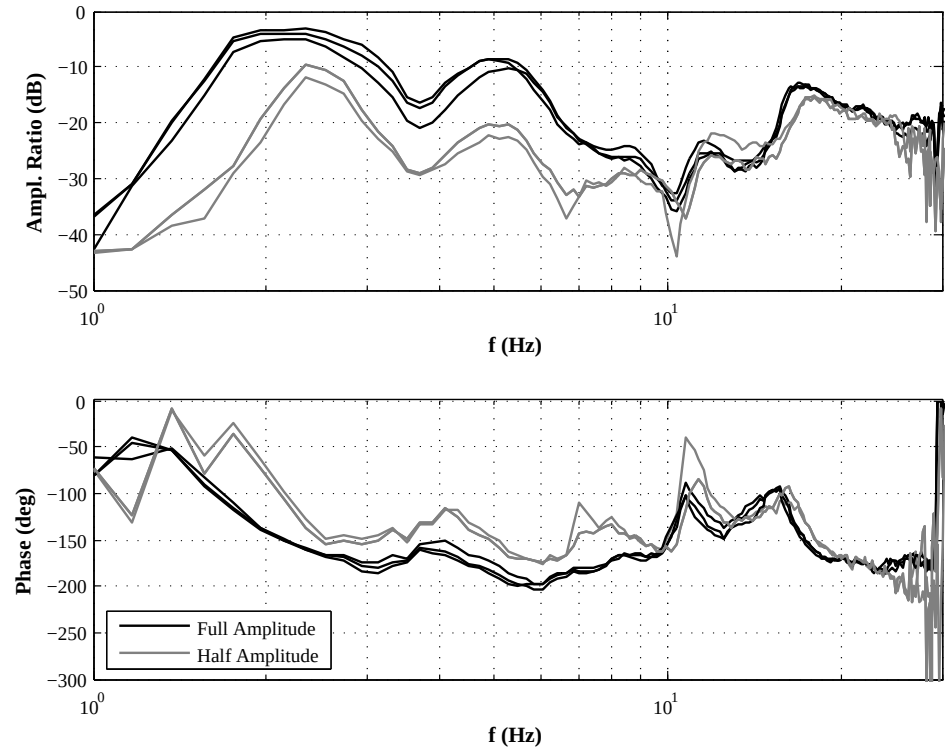

Figure A.4: Left suspension displacement in roll

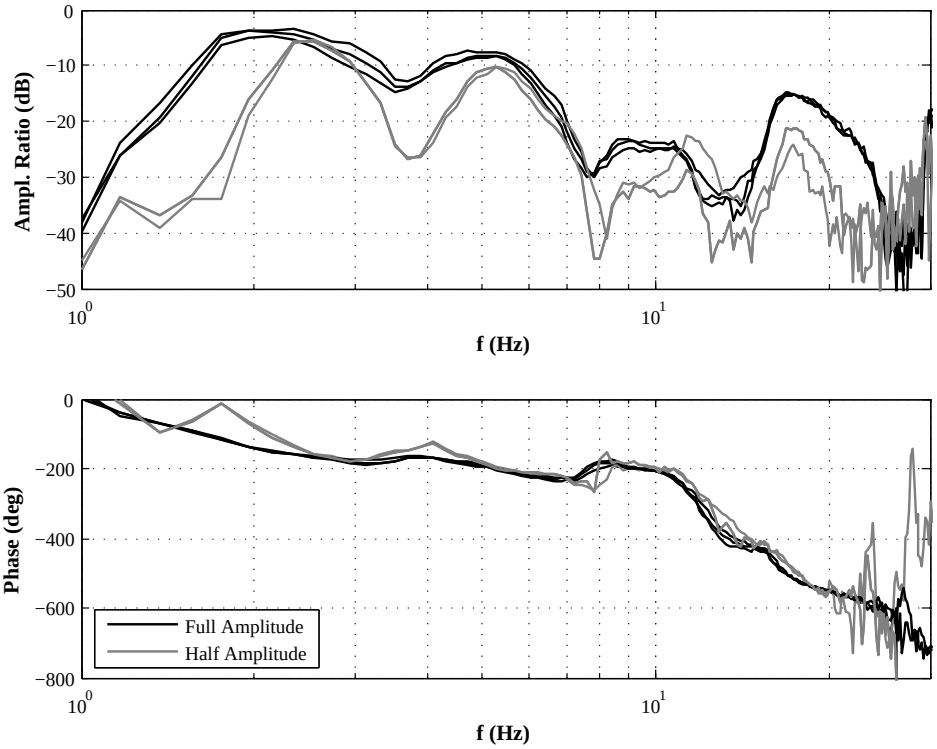

Figure A.5: Right suspension displacement in roll

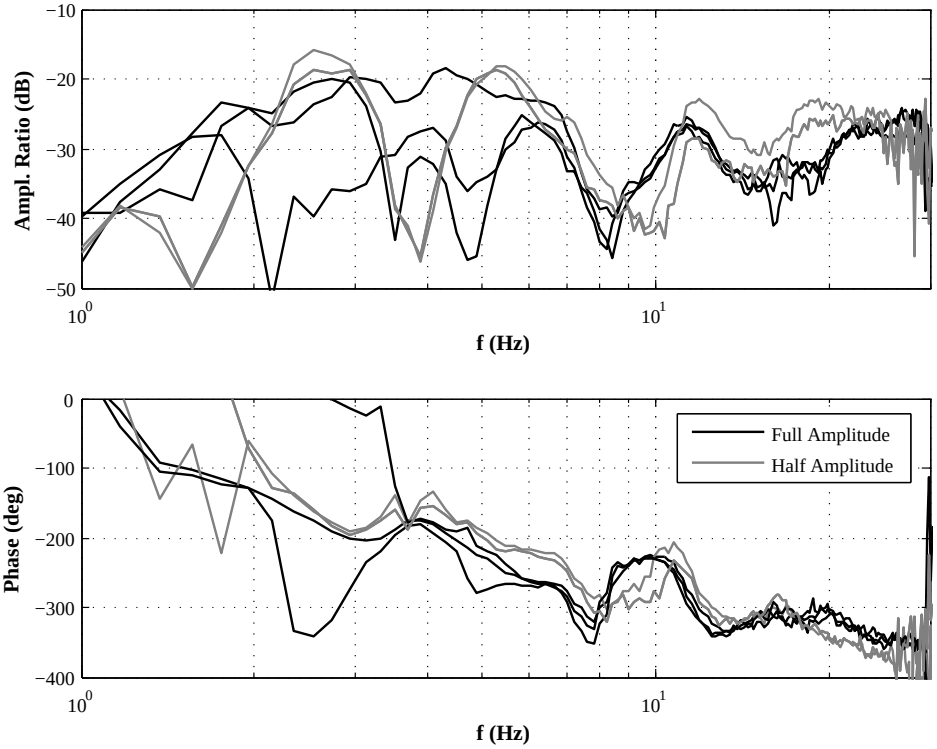

Figure A.6: Average suspension displacement in roll

Symbol	Description	Value
C_{act}	Actuator damping	$3000Nsm^{-1}$
C_r	Roll bar damping	$0Nsm^{-1}$
C_{s1}	Rear spring compression damping	$2600Nsm^{-1}$
C_{s2}	Rear spring rebound damping	$4500Nsm^{-1}$
C_{sf}	Front spring damping	$36000Nsm^{-1}$
C_t	Rear vertical tyre damping	$400Nsm^{-1}$
C_{tf}	Front vertical tyre damping	$400Nsm^{-1}$
C_{ty}	Rear lateral tyre damping	$50Nsm^{-1}$
C_{tyf}	Front lateral tyre damping	$1500Nsm^{-1}$
$C_{t\psi}$	Rear rotational tyre damping (z axis)	$0.5Nms\ /^{\circ}$
$C_{t\psi f}$	Front rotational tyre damping (z axis)	$8Nms/^{\circ}$
K_{act}	Actuator stiffness	$1.05 \cdot 10^6 Nm^{-1}$
K_r	Roll bar stiffness	$1.2 \cdot 10^6 Nm^{-1}$
K_s	Rear spring stiffness	$39900Nm^{-1}$
K_{sf}	Front spring stiffness	$31000Nm^{-1}$
K_t	Rear vertical tyre stiffness	$420000Nm^{-1}$
K_{tf}	Front vertical tyre stiffness	$420000Nm^{-1}$
K_{ty}	Rear lateral tyre stiffness	$160000Nm^{-1}$
K_{tyf}	Front lateral tyre stiffness	$85000Nm^{-1}$
$K_{t\psi}$	Rear rotational tyre stiffness (z axis)	$100Nm\ /\ ^{\circ}$
$K_{t\psi f}$	Front rotational tyre stiffness (z axis)	$100Nm\ /\ ^{\circ}$

Table A.1: Parameter values for the SimMechanics model

References

[1] Anon. "Regulation (EC) No 443/2009 of the European Parliament and of the Council of 23 April 2009 setting emission performance standards for new passenger cars as part of the Community's integrated approach to reduce CO 2 emissions from light-duty vehicles (Text with EEA relevance)". Technical report, European Parliament, Council, 2009. Procedure number: COD(2007)0297.

[2] S. Hanzl, A. Neumann, J. Stark, and G. Sammer. "CLEVER Deliverable D9: Benefits for Urban Traffic". Technical report, Universitt fr Bodenkultur Vienna, Institute of Transport, 2005. Internal Report for European Commission.

[3] Y. Li, J. L. Meiry, and W. G. Roesler. "An Active Roll Mode Suspension System for Ground Vehicles". *Journal for Basic Engineering*, pages 167–174, 1968.

[4] R. Hibbard and D. Karnopp. "Twenty First Centry Transportation System Solutions - a New Type of Small, Relatively Tall and Narrow Active Tilting Commuter Vehicle". *Vehicle System Dynamics*, 25(5):321–347, 1996.

[5] W. L. Garrison and M. E. Pitstick. "Lean Machines: Preliminary Investigations". *Paper UCB-ITS-90-4*, 1990.

[6] S. Kidane, L. Alexander, R. Rajamani, P. Starr, and M. Donath. "A fundamental investigation of tilt control systems for commuter vehicles". *Vehicle System Dynamics*, 46(4):295–322, 2008.

[7] J. Berote, A. van Poelgeest, J. Darling, K. Edge, and A. Plummer. "The dynamics of a three-wheeled narrow-track tilting vehicle". In *FISITA World Automotive Congress 2008, The Future of Automobiles and Mobility*, Munich, Germany, 14–19 September 2008. Paper number F2008-SC-032.

[8] J. Berote, A. Plummer, and J Darling. "Lateral Dynamics Optimisation of a Direct Tilt Controlled Narrow Vehicle". In *Proceedings of the 10th International Symposium on Advanced Vehicle Control (AVEC 2010)*, 22–26 Aug 2010.

[9] S. So and D. Karnopp. "Active Dual Mode Tilt Control for Narrow Ground Vehicles". *Vehicle System Dynamics*, 27:19–36, 1997.

[10] S-G. So and D. Karnopp. "Switching strategies for narrow ground vehicles with dual mode automatic tilt control". *Int. J. of Vehicle Design*, 18(5):518–532, 1997.

[11] M. Barker. *Chassis Design and Dynamics of a Tilting Three Wheeled Vehicle*. PhD thesis, University of Bath, Bath, UK, 2006.

[12] C. van den Brink and H. Kroonen. "Dynamic Vehicle Control for Enclosed Narrow Vehicles". In *Proceedings of EAEC 6th European Congress: Lightweight and Small Cars—The Answer to Future Needs*, 2–4 July 1997. Paper number 97A2I22.

[13] C Van den Brink and H. Kroonen. "DVC — The banking technology driving the CARVER vehicle class". In *Proceedings of the 7th International Symposium on Advanced Vehicle Control (AVEC04)*, 13–20 Aug 2004.

[14] C. van den Brink and H. Kroonen. "Slender Comfort Vehicles: Offering the Best of Both Worlds". *AutoTechnology*, pages 56–59, 1/2004.

[15] R. Moore. "U researchers advance narrow commuter vehicle concept". Obtained from: `http://www1.umn.edu/umnnews/Feature_Stories/U_researchers_advance_narrow_commuter_vehicle_concept.html` on 19/9/2007.

[16] J. C. Chiou and C. L. Chen. "Modeling and Verification of a Diamond-Shape Narrow-Tilting Vehicle". *IEEE/ASME Transactions on Mechatronics*, 13(6):678–691, 2008.

[17] J. C. Chiou, C. Y. Lin, C. L. Chen, and Chien C. P. "Tilting Motion Control in Narrow Tilting Vehicle Using Double-Loop PID Controller". In *Proceedings of the 7th Asian Control Conference*, pages 913–918, Hong Kong, China, 27–29 August 2009.

[18] D. Karnopp and C. Fang. "A Simple Model of Steering-Controlled Banking Vehicles". *ASME, Dynamic Systems and Control Division (Publication) DSC, Transportation Systems*, 44:15–28, 1992.

[19] D. Karnopp and R. Hibbard. "Optimum Roll Angle Behavior for Tilting Ground Vehicles". *ASME, Dynamic Systems and Control Division (Publication) DSC, Transportation Systems*, 44:29–37, 1992.

[20] R. Hibbard and D. Karnopp. "Methods of Controlling the Lean Angle of Tilting Vehicles". *ASME, Dynamic Systems and Control Division (Publication) DSC, Transportation Systems*, 52:311–320, 1993.

[21] R. Hibbard and D. Karnopp. "The Dynamics of Small, Relatively Tall and Narrow Tilting Ground Vehicles". *ASME, Dynamic Systems and Control Division (Publication) DSC, Transportation Systems*, 52:397–417, 1993.

[22] D. Karnopp. "The Dynamics of Narrow, Automatically Tilted Commuter Vehicles". In *Proceedings of the 1997 EAEC Congress: Lightweight and small cars: the answer to future needs*, pages 13–19, 1997. Paper number 97A2KN08.

[23] D. Karnopp. "Tilt Control for Gyro-Stabilized Two-Wheeled Vehicles". *Vehicle System Dynamics*, 37(2):145–156, 2002.

[24] A. Snell. "An Active Roll Moment Control Strategy for Narrow Tilting Commuter Vehicles". *Vehicle System Dynamics*, 29:277–307, 1998.

[25] R. Gohl, R. Rajamani, L. Alexander, and P. Starr. "The Development of Tilt-Controlled Narrow Ground Vehicles". In *Proceedings of the American Control Conference*, 2002.

[26] J. Gohl, R. Rajamani, L. Alexander, and P. Starr. "Active Roll Mode Control Implementation on a Narrow Tilting Vehicle". *Vehicle System Dynamics*, 42(5):347–372, 2004.

[27] J. Gohl, R. Rajamani, P. Starr, and L. Alexander. "Development of a Novel Tilt-Controlled Narrow Commuter Vehicle", 2006. Obtained from: http://www.cts.umn.edu/pdf/CTS-06-05.pdf on 21/09/2007.

[28] R. Rajamani, J. Gohl, L. Alexander, and P. Starr. "Dynamics of narrow tilting vehicles". *Mathematical and Computer Modelling of Dynamical Systems*, 9(2):209–231, 2003.

[29] D. Piyabongkarn, T. Keviczky, and R. Rajamani. "Active Direct Tilt Control for Stability Enhancement of a Narrow Commuter Vehicle". *International Journal of Automotive Technology*, 5(2):77–88, 2004.

[30] J. P. Pauwelussen. "The Dynamic Behaviour of Man-Wide Vehicles With An Automatic Active Tilting Mechanism". In *Proceedings of the 1999 EAEC Congress: Vehicle Systems Technology for the Next Century: Conference II — Vehicle Dynamics and Active Safety*, pages 50–58, 30 June–2 July 1999. Paper number STA99C206.

[31] J.P. Pauwelussen. "The Dynamic Performance of Narrow Actively Tilting Vehicles". In *Proceedings of the 5th International Symposium on Advanced Vehicle Control (AVEC 2000)*, 22–24 Aug 2000.

[32] V. Cossalter, N. Ruffo, F. Biral, and R. Berritta. "Development of a novel three-wheeled vehicle". In *3r̂d International Motorcycle Conference*, 2000.

[33] P. Agostinetti, V. Cossalter, and N. Ruffo. "Experimental analysis of handling of a three wheeled vehicle". In *9t̂h International Conference on High-Tech Cars and Engines*, 2003.

[34] S. Kidane, R. Rajamani, L. Alexander, P. Starr, and M. Donath. "Experimental Investigation of a Narrow Leaning Vehicle Tilt Stability Control System". In *Proceedings of the 2007 American Control Conference*, 11–13 Jul 2007.

[35] B. Drew. *Development of Active Tilt Control For A Three-Wheeled Vehicle*. PhD thesis, University of Bath, Bath, UK, 2006.

[36] H. B. Pacejka. *"Tyre and Vehicle Dynamics"*. Butterworth-Heinemann, 2002.

[37] Anon. "FP4: Component Selection for Hydraulic Systems", Oct 1999. CPTMC, University of Bath. Course Notes.

[38] Anon. "FP2: Introduction to Control for Electrohydraulic Systems", Nov 2003. CPTMC, University of Bath. Course Notes.

[39] H. S. Radt and W.F. Milliken. "Non-dimensionalizing Tyre Data for Vehicle Simulation". *Road Vehicle Handling*, 1983.

[40] W. F. Milliken and D. L. Milliken. *"Race Car Vehicle Dynamics"*. SAE, 1995.

[41] V. Cossalter. *"Motorcycle Dynamics 2nd Edition"*. LuLu (Self Publishing), 2006.

[42] E. J. H. de Vries and H. B. Pacejka. "Motorcycle Tyre Measurements and Models". *Vehicle System Dynamics*, 1(29):280–298, 1998.

[43] A. Wiedele and M. Schmieder. "Research on the Power Transfer of Motorcycle Tires on Real Road Surfaces". In *Proceedings of the 18th FISITA Congress*, 1990.

[44] H. Ishii and Y. Tezuka. "Considerations of Turning Performance for Motorcycles". 1979. JSAE SAE Paper number 972127.

[45] H. Sakai, O. Kanaya, and H. Iijima. "Effect of Main Factors on Dynamic Properties of Motorcycle Tires". 1979. SAE Paper number 790259.

[46] V. Cossalter, A. Doria, R. Lot, N. Ruffo, and M. Salvador. "Dynamic Properties of Motorcycle and Scooter Tires: Measurements and Comparison". *Vehicle System Dynamics*, 5(39):329–352, 2003.

[47] M. C. Best. "Identifying tyre models directly from vehicle test data using an extended Kalman filter". *Vehicle System Dynamics*, pages 1–17, 2009.

[48] J. Hahn, R. Rajamani, and L. Alexander. "GPS-Based Real-Time Identification of Tire-Road Friction Coefficients". In *IEEE Transactions on Control Systems Technology*, volume 10, 2002.

[49] C. R. Carlson and J. C. Gerdes. "Consistent Nonlinear Estimation of Longitudinal Tire Stiffness and Effective Radius". In *IEEE Transactions of Control Systems Technology*, volume 13, 2005.

[50] 4/2 and 4/3 proportional directional valves direct operated, with electrical position feedback: Types 4WRE and 4WREE, 2003. Rexroth Bosch Group. Catalogue Number RE 29 061/02.03.

[51] J. C. Huston, B. J. Graves, and D. B. Johnson. "Three Wheeled Vehicle Dynamics". *SAE Paper 820139*, 1982.

[52] P. G. Van Valkenburgh and R. H. Klein. "Three-Wheel Passenger Vehicle Stability and Handling". *SAE Paper 820140*, 1982.